PISTON

Journal of Technical Engineering

Vol. 9
No. 2
January 2026
ISSN 2541-3511

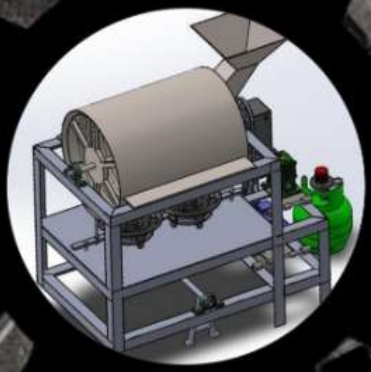

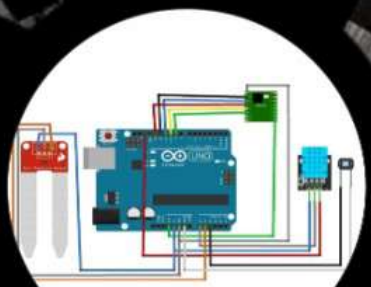

Program Studi Teknik Mesin
Fakultas Teknik
Universitas Pamulang

EDITORIAL BOARD

Piston: Journal of Technical Engineering
Universitas Pamulang
Volume 9, Number 2
January 2026

The editorial board accepts original manuscripts from academics, researchers, and practitioners that have not been previously published. A blind review process is used to determine the suitability of manuscripts for publication. Submission guidelines are provided in this journal. Submitted manuscripts must include a soft copy.

Editorial Office Address
Mechanical Engineering Department, Faculty of Engineering, Universitas Pamulang
Jl. Surya Kencana No.1, Pamulang – South Tangerang, Indonesia
Phone: (+6221) 7412566.
E-mail: piston@unpam.ac.id

PISTON:
Journal of Technical Engineering:

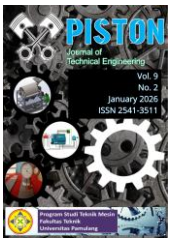

SCOPE OF THE JOURNAL

Piston Journal of the Mechanical Engineering Study Program at Pamulang University accepts manuscripts on a wide range of topics in the field of mechanical engineering, including but not limited to:

1. Energy conversion
2. Materials
3. Manufacturing
4. Mechanical design and construction
5. Other areas related to mechanical engineering.

MANUSCRIPT FORMAT

Manuscripts submitted to this journal—whether conceptual studies or empirical research—should follow the structure outlined below:

(1) **Author(s)**: Full name(s) accompanied by institutional affiliation(s).
(2) **Abstract**: Presented in both Indonesian and English, along with keywords. The abstract should not exceed 300 words.
(3) **Introduction**.
(4) **Main content**.
- For conceptual articles: includes core discussion and analysis.
- For research-based articles: includes:
  - Research methodology, and
  - Result and discussion.
- Figures, tables, and mathematical equations must be sequentially numbered and properly captioned.

(5) Conclusion
(6) Recommendations (if applicable)
(7) Acknowledgments (if applicable).
(8) **References**: A minimum of 10 references is required, with preference given to recent sources.

Manuscript Formatting Guidelines

1. Manuscripts must be submitted in .docx or .doc format.
2. Font: Times New Roman.
3. Single-column layout.
4. Line spacing: single. Paper size: A4.
5. Length: Minimum 5 pages, maximum 10 pages.
6. Margins: 1 cm on all sides (top, bottom, left, right).
7. Image resolution: Minimum 300 dpi, accepted formats include PNG, JPEG, and BMP.
8. References should follow the IOP referencing style

All submitted manuscripts will be reviewed by peer reviewers (Mitra Bestari) to assess their relevance to the journal's scope and the quality of the content. Accepted papers will be published in the *Piston Journal* of Universitas Pamulang.

PISTON:
Journal of Technical Engineering:

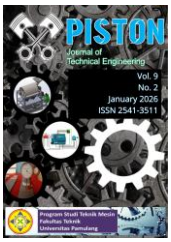

TABLE OF CONTENTS

PISTON:
Journal of Technical Engineering:

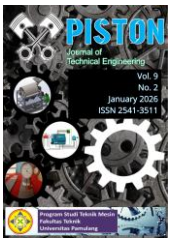

FOREWORD

Alhamdulillahirabbil 'Alamin, all praise and gratitude we extend to Allah SWT for His blessings and guidance, through which the *Journal of Technical Engineering*, Vol. 9, No. 2, January 2026, has been successfully published on schedule.

In this edition of the *Journal of Technical Engineering*, the published articles cover topics including paddy drying systems using integrated heat pump, solar energy, and biomass furnaces; cooling load analysis using the CLTD method; synthesis and application of coconut shell–derived graphene and graphene-like carbon materials; numerical performance analysis of Savonius and Flettner rotors for sustainable energy applications; development of regulatory recommendations for city bus bumper bars; and synthesis of dual-doped ZnO nanofibers for piezoelectric nanogenerator applications.

We encourage continued participation from researchers, lecturers, academics, and practitioners to contribute to this journal, ensuring its consistent publication according to the established schedule. Such contributions are vital for enhancing the quality and diversity of topics in accordance with the scope of mechanical engineering.

It is our hope that this journal provides valuable insights and contributes meaningfully to the advancement of science and technology, while also serving as a reference for national development efforts.

Finally, as no work is ever without flaws, we sincerely apologize for any shortcomings. Constructive feedback and suggestions are highly welcomed for the continuous improvement of this journal.

Pamulang, January 2026

Editorial Board

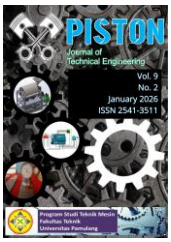

AUTHOR INDEX

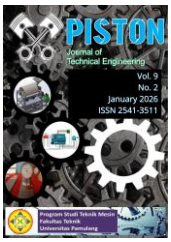

N

Novan Habiburrahman

Nurrahim Hasan Al Banna

Nur Rohmat

P

Putri Pratiwi

R

Ramadhan Haryo Dewanto

Ruzita Sumiati

Y

Yuli Yetri

Z

Zido Yuwazama

PISTON
Journal of Technical Engineering:

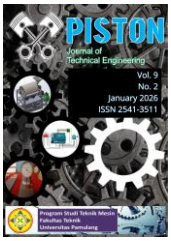

Performance Evaluation of an Integrated Heat Pump Fluidized-Bed Dryer with Solar and Biomass Furnace for Paddy Drying

M. Yahya[1], Zido Yuwazama[1,a)], Dedi Wardianto[1,b)], Putri Pratiwi[1], Delvis Agusman[2]

[1]*Department of Mechanical Engineering, Faculty of Engineering, Institut Teknologi Padang, Padang, 25173, Indonesia*
[2]*Department of Mechanical Engineering, Faculty of Industrial Technology and Informatics, Universitas Muhammadiyah Prof. DR. HAMKA, Jakarta, 12130, Indonesia*

E-mail: [a)] zidoyuwazama23@gmail.com
[b)] wardiantodedi71@gmail.com

Received: Desember 08, 2025 *Revision: Desember 15, 2025* *Accepted: Desember 31, 2025*

Abstract: This study aims to evaluate the performance of a heat pump fluidized-bed dryer incorporating a biomass furnace and a solar collector for paddy drying. The paddy moisture content (MC) was decreased from 28.52% to 16.28% on a dry basis (db) through the drying process over 23.68 minutes, under operating conditions of a mass flow rate of 0.1033 kg/s and an average temperature of 70 °C. An average drying rate of 0.042 kg/min was achieved, corresponding to a specific moisture extraction rate of 0.24 kg/kWh. Correspondingly, the system required average specific electrical and thermal energy consumptions of 7.43, 3.21, and 4.22 kWh/kg, respectively. The biomass furnace demonstrated a high thermal efficiency of 87.9%, while the solar collector achieved an average efficiency of 31.7%. The heat pump exhibited stable performance, with an average coefficient of performance measured at 3.2. The heat pump condenser, solar collector, and biomass furnace generated average heat energies of 2.37 kW, 0.79 kW, and 2.91 kW, respectively. The dryer exhibited average thermal and pickup efficiencies of 21.8% and 40.4%. The average exergy efficiency was 57.7%. Furthermore, the incorporation of the heat recovery exchanger resulted in an approximate 47% reduction in heat energy consumption.

Keywords: Paddy, Fluidized-bed Dryer, Heat Recovery, Drying, Performance.

Abstrak: *Kinerja pengering heat pump fluidized-bed yang menggabungkan kolektor surya dan tungku biomassa untuk pengeringan padi dievaluasi. Sistem pengeringan tersebut berhasil mengurangi kadar air padi dari 28,52% db menjadi 16,28% db selama 23,68 menit, pada kondisi operasi dengan laju aliran massa 0,1033 kg/s dan suhu rata-rata 70 °C. Laju pengeringan rata-rata sebesar 0,042 kg/menit tercapai, yang sesuai dengan laju ekstraksi air spesifik sebesar 0,24 kg/kWh. Dengan demikian, sistem tersebut membutuhkan konsumsi energi spesifik, listrik, dan termal rata-rata masing-masing sebesar 7,43, 3,21, dan 4,22 kWh/kg. Tungku biomassa menunjukkan efisiensi termal yang tinggi sebesar 87,9%, sedangkan kolektor surya mencapai efisiensi rata-rata sebesar 31,7%. Heat pump menunjukkan kinerja yang stabil, dengan koefisien kinerja rata-rata sebesar 3,2. Tungku biomassa, kondensor heat pump, dan kolektor surya menghasilkan energi panas rata-rata masing-masing sebesar 2,91, 2,37, dan 0,79 kW. Pengering menunjukkan efisiensi termal dan efisiensi penyerapan rata-rata masing-masing sebesar 21,8% dan 40,4%. Efisiensi eksergi rata-rata adalah 57,7%. Lebih lanjut, penggabungan heat recovery exchanger menghasilkan pengurangan konsumsi energi panas sekitar 47%.*

Kata kunci: *Padi, Fluidized-bed Dryer, Heat Recovery, Pengeringan, Kinerja.*

INTRODUCTION

As an agrarian nation, Indonesia is recognized as a major global producer of paddy rice, yielding roughly 84 million tons annually. This commodity supports the livelihoods of about 30 million Indonesian farmers [1].

Freshly harvested paddy generally exhibits elevated moisture content (MC), typically between 20% and 27% on a wet basis (wb) [2]. Under these moisture conditions, the grain is unsuitable for storage due to its increased vulnerability to microbial contamination. Consequently, the MC must be reduced to approximately 14% wb to inhibit microbial activity, minimize the risk of discoloration, and ensure its suitability for long-term storage [3].

Drying paddy is the process of decreasing the grain's moisture content by evaporating moisture through the application of heat energy to achieve a specified MC. Numerous types of drying systems are typically utilized to achieve this objective, including fluidized-bed dryers, fixed-bed dryers, open-sun dryers, rotary dryers, and inclined-bed dryers. Fluidized-bed dryers are widely adopted due to their high effectiveness compared to other drying systems. They offer several advantages, such as having a simple structural design, requiring relatively short drying times, producing high-quality dried products, and requiring low initial investment and maintenance costs. Furthermore, fluidized-bed dryers are well-suited for processing wet particulate and granular materials, including food, medicinal herbs, chemical, and agricultural and pharmaceutical [4].

The performance of a fluidized-bed dryer applied to paddy drying was investigated. The findings indicated that decreasing the paddy MC from 36.98% to 27.58% on a dry basis (db), at roughly 7.75 t/h of drying throughput and inlet air temperature of about 100–120 °C, required 7.57 and 0.79 MJ/kg of thermal and electrical energy inputs, respectively [5]. In paddy drying, a significant amount of energy is required to evaporate MC from the grains. In industrial drying applications, manufacturing operations account for nearly 12% of the total energy consumption, while the drying process represents roughly two-thirds of the overall capital investment cost [6].

Besides energy consumption, other prominent considerations for the paddy drying process include the drying rate, operational costs, type of energy source employed, and the quality of the dried grain output. At present, fossil fuels remain the primary energy source for drying processes. However, fossil-fuel reserves are limited. Additionally, they contribute to air pollution, as well as having high prices and steadily rising costs. At the same time, overall energy demand continues to increase. Solar drying offers a viable solution to fossil-fuel-based systems by utilizing solar energy to carry out the drying process. This approach offers reduced energy demand and lower operational costs relative to conventional drying systems. Moreover, solar energy is widely available in numerous regions and serves as a clean and sustainable source of power.

A variety of solar dryer designs and configurations have been introduced to process a wide range of agricultural and industrial materials. These include cabinet-type solar dryers used to dry spices and herbs [7], olive mill wastewater [8], red chili [9], and palm oil fronds [10]. Researchers have also developed other designs, such as greenhouse solar dryers [11], tunnel solar dryers [12], and dryers of Andrographis paniculata [13]. Nevertheless, their performance is constrained by low solar irradiance and intermittent sunlight, as the solar collectors are capable of capturing only a limited amount of solar energy. Solar dryers are often coupled with a biomass furnace to solve these limitations.

Integrated solar–biomass drying systems are applied to various products such as spices and medicinal herbs [14], pineapple [15], chili [16], and fish [17]. In these arrangements, the system is often described as a hot dryer where the elevated drying-air temperature increases the rate of the drying process. However, excessively high drying-air temperatures may decrease product quality. An alternative approach for enhancing the drying rate involves lowering the drying air MC, which can be achieved through dehumidification using a heat pump system.

Drying technologies integrating heat pump with biomass and solar energy sources are extensively developed for processing a wide range of products. Red chili [18], copra [19], and cassava [20] have been dried using cabinet-type solar dryers integrated with heat pump units. Also, paddy drying has been carried out using hybrid solar–fluidized-bed drying incorporating a biomass furnace and heat pump [21]. Thermal energy losses within the drying system, losses from system components, including drying chamber and the air-heating units (solar collectors, biomass burners, and biomass furnaces), serve a critical role because they raise the overall energy consumption during operation and decrease the system's energy efficiency. The integration of a heat recovery exchanger leads to reduced energy losses and enhanced drying process efficiency.

Recovery heat exchangers are implemented across various drying technologies to utilize waste heat and improve operational efficiency. Several studies have implemented this approach for different drying applications, such as cabinet solar dryers incorporating a heat-pump system for drying radish [22]; mint leaves drying using a heat pump [23]; and drying red chili using a cabinet dryer combined with a biomass furnace [24]. Fluidized-bed dryers incorporating a heat recovery exchanger with a heat pump have been evaluated. A 66.9% reduction in the energy demand for wheat drying was achieved with the implementation of a heat recovery unit [25].

Based on the existing literature, the performance of a heat pump-assisted fluidized-bed dryer incorporating a solar collector and a biomass furnace has not yet been investigated for paddy drying. Consequently, the present research focuses on the design and performance evaluation of an integrated heat pump fluidized-bed dryer incorporating a heat recovery exchanger.

METHODS

A heat pump-assisted fluidized-bed dryer incorporating a biomass furnace, a solar collector, and a heat recovery exchanger was developed and constructed. The integrated drying system comprises several major components, including solar collector, heat pump, drying chamber, blower, cyclone separator, and biomass furnace, as presented in Figure 1. A schematic of the drying system is presented in Figure 2. The biomass furnace is configured with a dedicated heat exchanger, a combustion chamber for biomass fuel oxidation, and an exhaust chimney to ensure proper flue gas discharge. The heat exchanger employed is of the cross-flow type. The biomass furnace is equipped with a two-stage heat exchanger system. The primary stage heat exchanger functions as a primary air heater, whereas the second-stage heat exchanger serves as a preheating unit as well as a heat-recovery component. A flat-plate solar collector with a single-pass flow arrangement is implemented in the system using an area of approximately 3.6 m². The heat pump system incorporates an evaporator, condenser, compressor, and capillary tube as its main components. The power input is 1 HP and the refrigerant used is R22. The evaporator and condenser are of the cross-flow fin-and-tube type. The design incorporates a drying chamber configured as a horizontal fluidized bed. The blower used to circulate the air has a power input of 3.7 kW.

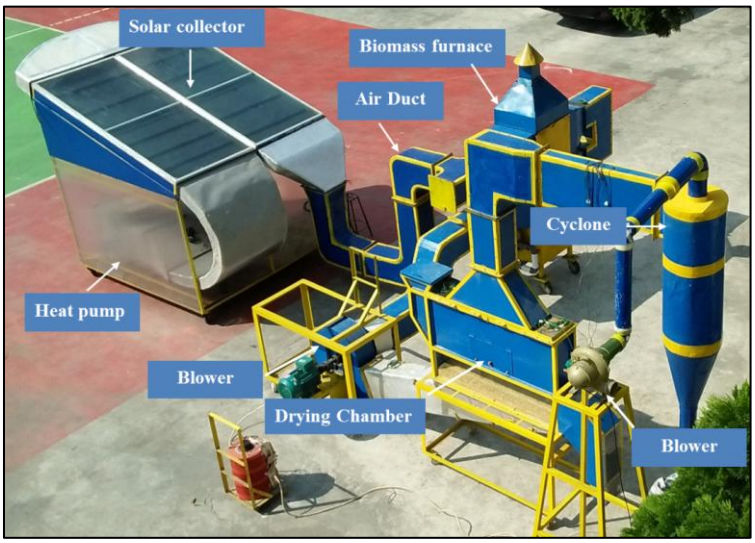

Figure 1. An integrated heat pump fluidized-bed dryer with a solar collector and a biomass furnace

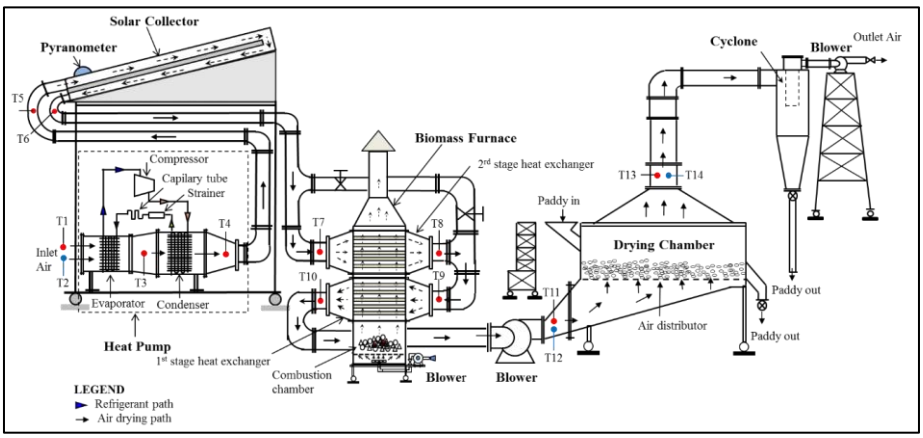

Figure 2. Schematic of an integrated heat pump fluidized-bed dryer incorporating a solar collector and a biomass furnace

An initial MC of 22.19% (wb) was observed in fresh paddy grains (Oryza sativa L.) obtained from Padang, West Sumatra. A total of approximately 12 kg of the grains was then loaded into the drying chamber. The operational conditions of the drying system were comprehensively monitored with several instruments. Air temperatures at various locations within the drying system were measured using thermocouples, whereas solar radiation and airflow rate were measured using a pyranometer and a flowmeter, respectively. The paddy mass change during the drying process was quantified using a electronic balance. Both the paddy mass and air temperatures were recorded periodically at 5 min intervals to accurately monitor the drying dynamics. Coconut-shell charcoal served as the biomass fuel. The relative humidity of the ambient air, as well as the air exiting and entering the drying chamber, was determined from dry- and wet-bulb temperature measurements using a psychrometric chart.

RESULT AND DISCUSSION

The relationship between paddy MC and drying rate as a function of drying time is presented in Figure 3. The paddy MC decreased significantly from 28.52% db (22.19% wb) to 16.28% db (14.0% wb) under operating conditions of 13.78% relative humidity, 70 °C as a mean drying temperature, and 0.1033 kg/s of an air mass flow rate. This MC reduction was achieved within approximately 23.68 minutes of drying. Additionally, Figure 3 shows that the drying rate varied within the range of 0.010 to 0.110 kg/min (averaging 0.042 kg/min). The drying rate was initially high at the early stage of the drying process, corresponding to the high initial MC of the paddy. During paddy drying, the MC gradually decreased, resulting in a continuous reduction in the drying rate over time. This trend indicates that the drying rate is significantly influenced by the paddy MC. Increasing the drying time causes a decrease in the moisture content on a dry basis (%) as well as a decrease in the drying rate (kg/min). These results suggest that the drying process predominantly occurs in the falling-rate period, which is typical for agricultural products such as paddy.

At the initial drying stage (0–5 min), the MC was relatively high, exceeding 28% db, which resulted in the highest drying rate of approximately 0.110 kg/min. This behavior can be attributed to the abundance of free moisture on the paddy surface, allowing rapid evaporation when exposed to hot air. Then, the moisture content decreased steadily from approximately 23% to 17% db as drying time increased to around 10–20 minutes. During this period, the drying rate reduced significantly from about 0.075 kg/min to 0.045 kg/min. Beyond 20 minutes of drying, the moisture content dropped below 16% db, and the drying rate further decreased to values lower than 0.030 kg/min. In this final stage, the drying rate exhibited a gradual and nearly linear reduction. Overall, the data in Figure 3 clearly demonstrate an inverse relationship between moisture content and drying time, accompanied by a decreasing drying rate throughout the process. The absence of a constant-rate drying period suggests that paddy drying under the present operating conditions is dominated by the falling-rate period.

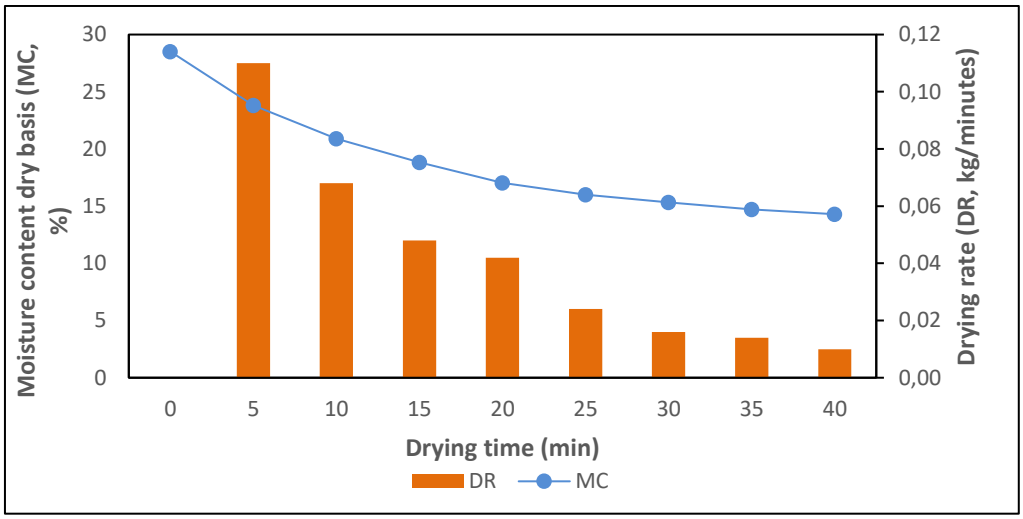

Figure 3. The relationship between drying rate and paddy MC as a function of drying time

The variations in specific energy consumption (SEC), specific thermal energy consumption (STEC), specific moisture extraction rate (SMER), and specific electrical energy consumption (SEEC) as functions of drying time are shown in Figure 4. The results present a decreasing trend in SMER as drying progresses, while SEC, STEC, and SEEC exhibit an opposite increasing tendency. The SMER varied between 0.06 kg/kWh and 0.65 kg/kWh (averaging 0.24 kg/kWh). The SEEC varied between 0.68 kWh/kg and 7.46 kWh/kg (averaging 3.21 kWh/kg), STEC varied between 0.87 and 9.71 kWh/kg (averaging 4.22 kWh/kg), and SEC varied between 1.55 kg/kWh and 17.16 kWh/kg (averaging 7.43 kWh/kg). The results indicate that SMER declined over time, while SEEC, STEC, and SEC increased, due to the gradual decline in the drying rate. Overall, the trends observed in Figure 4 demonstrate that energy efficiency is highest during the initial drying period, then reduces as the drying process approaches lower moisture contents.

At the initial stage of drying (5–10 min), SMER reaches its highest value, exceeding 0.6 kg/kWh, indicating efficient moisture removal with relatively low energy input. During this period, the high moisture content of the paddy facilitates rapid evaporation, resulting in favorable energy utilization. Concurrently, SEC, STEC, and SEEC remain low, reflecting minimal energy demand at the early drying stage. As drying time increases beyond 15 minutes, SMER gradually decreases to values below 0.1 kg/kWh. In contrast, SEC increases steadily from approximately 1 kWh/kg to nearly 18 kWh/kg at 40 minutes, indicating higher energy consumption per unit mass of evaporated moisture. Similarly, STEC and SEEC rise progressively throughout the drying

process. STEC shows a significant increase after 25 minutes, suggesting that thermal energy demand becomes dominant during the last stages of drying. SEEC also shows an increase at a lower rate, reflecting the cumulative electrical energy required for air circulation and system operation.

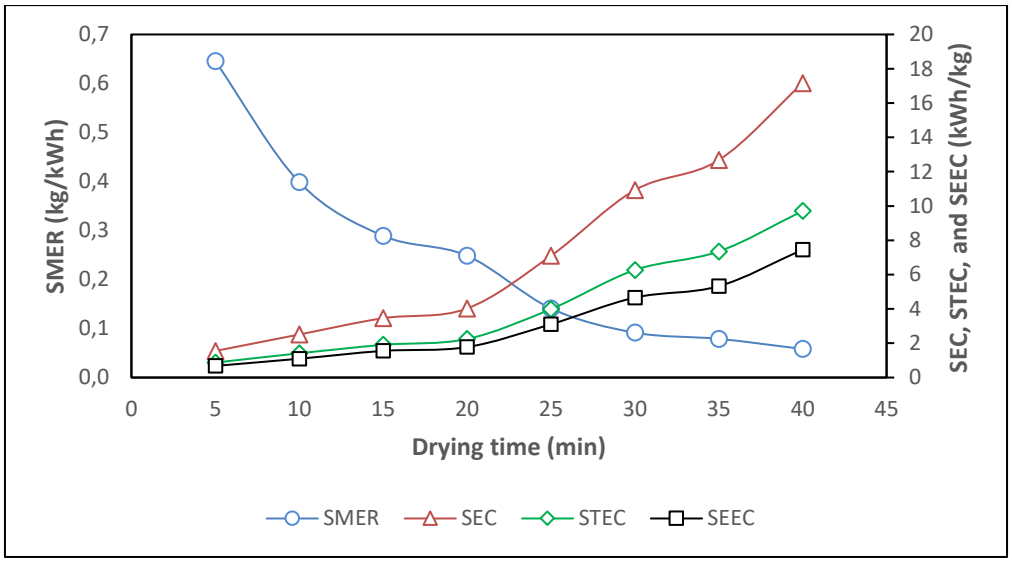

Figure 4. The relationship between SMER, SEEC, STEC, and SEC as a function of drying time

Variations in the thermal efficiencies of the solar collector and biomass furnace at 0.1033 kg/s of the air mass flow rate are illustrated in Figure 5. The solar collector efficiency varied between 24.0% and 39.7% (averaging 31.7%). The biomass furnace exhibited efficiencies from 77.0% to 96.5% (averaging 87.9%). Moreover, Figure 5 illustrates the temporal variations in the coefficient of performance (COP) for the heat pump, as well as the solar collector and biomass furnace thermal efficiencies over the drying process. The results indicate that the heat pump operates with a relatively stable COP throughout the drying period, with values ranging from approximately 2.9 to 3.3 (averaging 3.2), suggesting consistent performance under varying drying conditions. The efficiency of the biomass furnace exhibits significant fluctuations over time, reaching peak values close to 95% around the mid-stage of drying (20-30 min). This behavior can be attributed to more stable combustion conditions and improved heat transfer efficiency as the furnace reaches steady operation. In contrast, the solar collector efficiency shows lower absolute values, varying between approximately 25% and 40%, which reflects the dependence of solar thermal performance on incident solar radiation and thermal losses to the environment. As drying progresses beyond 30 minutes, the biomass furnace and solar collector efficiencies show a slight decline. This decrease is caused by reduced thermal demand as the material decreases in MC, leading to lower useful heat extraction relative to the available energy input. Overall, the trends presented in Figure 5 demonstrate the complementary roles of biomass furnace, solar collector, and heat pump in sustaining stable and efficient drying performance across different stages of the drying process.

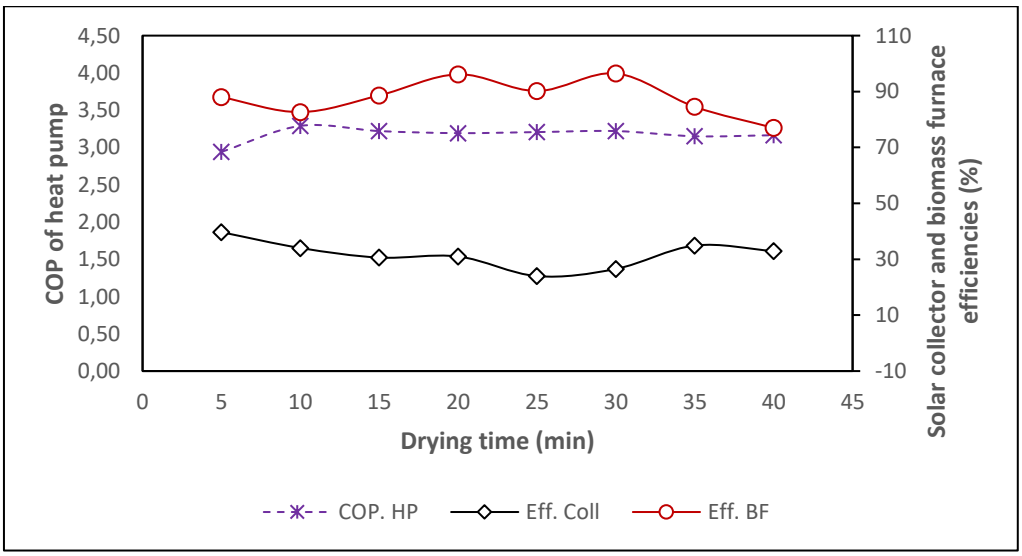

Figure 5. The relationship between the COP of the heat pump, solar collector and biomass furnace efficiencies as a function of drying time

Figure 6 illustrates the heat energy produced by a heat pump, biomass furnace, and solar collector at different drying times. The results show that the biomass furnace consistently provides the highest heat output throughout the drying process, with values ranging from approximately 2.55 kW to 3.19 kW (average 2.91 kW). This indicates that the biomass furnace serves as the primary thermal energy source, supplying stable and sufficient heat in maintaining the drying air temperature. The solar collector produces lower heat energy, ranging from about 0.58 kW to 1.00 kW (averaging 0.79 kW), and exhibits greater fluctuation compared to the other heat sources. These variations can be attributed to changes in solar radiation intensity and ambient conditions during the drying process. Despite its lower contribution, the solar collector plays a complementary role by reducing reliance on biomass fuel and enhancing the total energy efficiency of the hybrid drying system. In contrast, the heat pump condenser contributes a relatively steady heat output, varying between approximately 2.19 kW and 2.45 kW (averaging 2.37 kW). Overall, the combined operation of the heat pump, solar collector, and biomass furnace ensures a balanced and reliable heat supply across different drying stages.

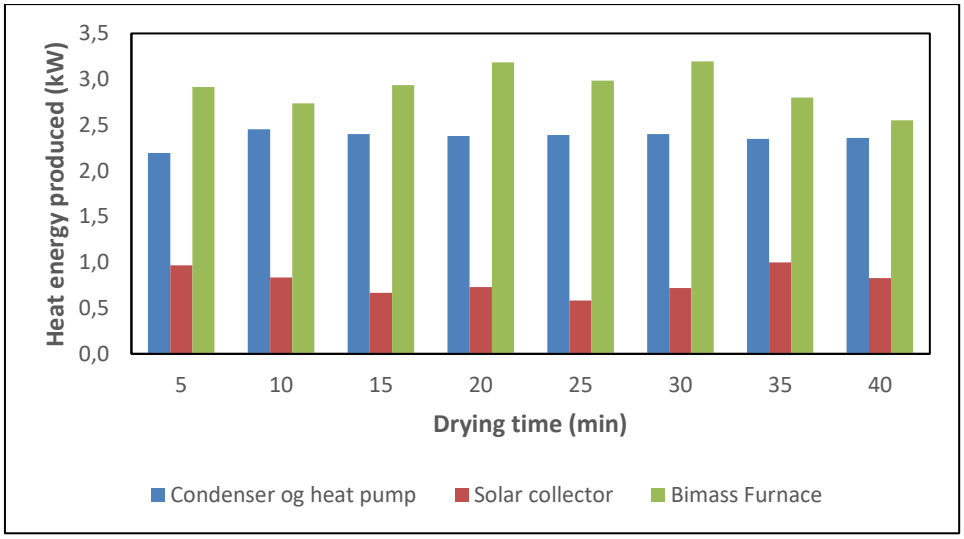

Figure 6. The relationship between heat energy produced and drying time

Figure 7 illustrates the energy fraction of the biomass and solar energy during drying. The fraction of solar energy remains relatively low throughout the drying process, varying between approximately 5.6% and 9.2% (averaging 7.5%). This indicates that solar energy functions primarily as an auxiliary energy source. Minor fluctuations in the solar fraction during drying time are attributed to variations in solar radiation intensity due to solar energy intermittency. Moreover, the biomass energy fraction exhibits consistently higher values, ranging from approximately 24% to 31% (averaging around 27–28%), confirming its dominant contribution to the total energy input. The peak biomass fraction observed at intermediate drying times (15-30 min) suggests increased thermal energy requirements to sustain stable drying temperatures and moisture removal rates. These results indicate that biomass energy plays a critical role in ensuring process continuity and thermal stability, while solar energy contributes to reducing overall biomass consumption and enhancing system energy efficiency.

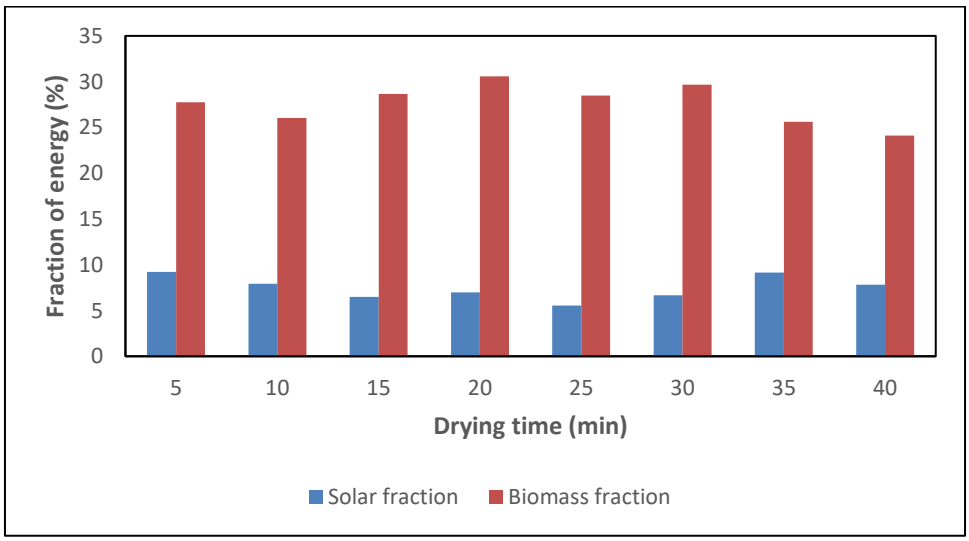

Figure 7. The relationship between energy fraction and drying time

The variation of exergy outflow and inflow, as well as exergy loss over drying is exhibited in Figure 8. The exergy outflow varied between 315.3 J/s and 891.1 J/s, with a mean value of 735.5 J/s, corresponding to the useful exergy carried by the exhaust air and the dried material. In contrast, the exergy inflow varied between 1134.7 J/s and 1456.1 J/s (averaging 1267.8 J/s). The exergy loss, which represents the irreversibility within the system, lay in the range of 373.1 J/s to 902.8 J/s, with an average of 532.4 J/s. The observed fluctuations in exergy parameters with increasing drying time indicate dynamic changes in mass and heat transfer mechanisms within the dryer. Higher exergy losses at certain drying intervals suggest intensified entropy generation due to non-equilibrium heat transfer and pressure losses within the drying chamber.

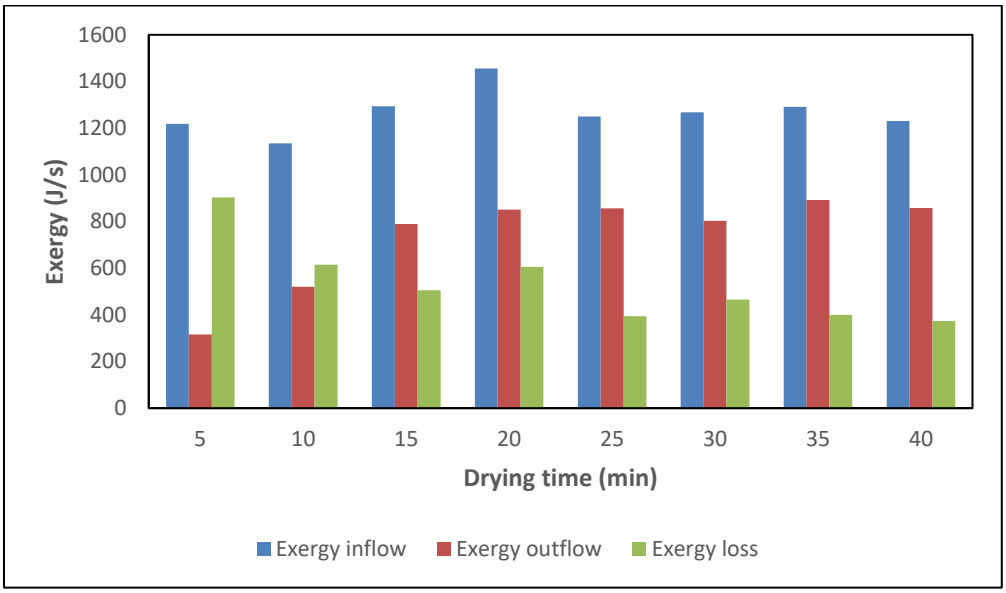

Figure 8. The relationship between exergy variation and drying time

Figure 9 depicts the changes in the thermal and pickup efficiencies of the dryer during the drying process. The thermal efficiencies of the dryer ranged from 3.7% to 40.8% (averaging 21.8%), while the pickup efficiency ranged from 11.4% to 79.5%, with an average value of 40.4%. Figure 9 also shows the variation in exergy efficiency during the drying process, which varied from 25.9% to 69.7%, with an average value of 57.7%. At the initial phase of drying, the thermal and pickup efficiencies were relatively high, but they were reduced toward the end of the process as the drying rate decreased over time.

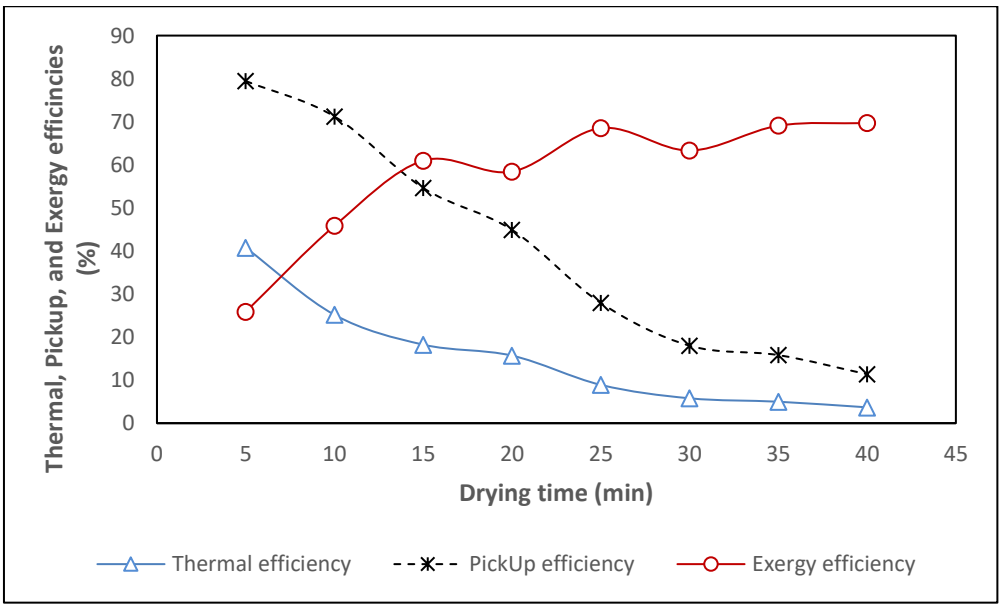

Figure 9. The relationship between thermal, pickup, and exergy efficiencies as a function of drying time

CONCLUSIONS

The paddy drying system combining a heat pump-assisted fluidized-bed dryer incorporating a solar collector and a biomass furnace was tested and assessed. The experiment results indicated that:

1. Paddy moisture content was successfully decreased from 28.52% db to 16.28% db over a period of 23.68 minutes by the drying system, which operated at a mass flow rate of 0.1033 kg/s and 70 °C average temperature.
2. Throughout the process, the drying rate fluctuated between 0.010 kg/min and 0.110 kg/min (averaging 0.042 kg/min).
3. The SMER obtained during the drying process varied between 0.06 kg/kWh and 0.65 kg/kWh (averaging 0.24 kg/kWh).
4. The SEEC, STEC, and SEC exhibited ranges of 0.68 to 7.46 kWh/kg (averaging 3.21 kWh/kg), 0.87 to 9.71 kWh/kg (averaging 4.22 kWh/kg), and 1.55 to 17.16 kWh/kg (averaging 7.43 kWh/kg).
5. The efficiency of the biomass furnace ranged from 77.0% to 96.5% (averaging 87.9%), while solar collector efficiency varied from 24.0% to 39.7% (averaging 31.7%).
6. The COP varied between 2.9 and 3.3, with a mean of 3.2.
7. The heat energy produced varied from 2.19 kW to 2.45 kW (averaging 2.37 kW) for the heat pump condenser, 2.55 kW to 3.19 kW (averaging 2.91 kW) for the biomass furnace, and 0.58 kW to 1.00 kW (averaging 0.79 kW) for the solar collector.
8. The energy fractions obtained in the experiment ranged from 5.6% to 9.2% (averaging 7.5%) for solar fraction and 24.1% to 30.6% (averaging 27.6%) for biomass fraction.
9. The loss of exergy, outflow, and inflow ranged from 373.1 J/s to 902.8 J/s (averaging 532.4 J/s), 315.3 J/s to 891.1 J/s (mean of 735.5 J/s), and 1134.7 J/s to 1456.1 J/s (averaging 1267.8 J/s), respectively.
10. The dryer exhibited thermal efficiencies of 3.7%–40.8% and pickup efficiencies of 11.4%–79.5%, with corresponding mean values of 21.8% and 40.4%.
11. The efficiency of exergy obtained in the experiment ranged from 25.9% to 69.7% (averaging 57.7%).
12. The implementation of a heat recovery exchanger in the drying system results in an approximate 47% decrease in heat energy demand.
13. Heat energy consumption in the drying system was lowered by roughly 47% using a heat recovery exchanger.

REFERENCES

[1] BPS, *Statistik Indonesia*. Jakarta: Badan Pusat Statistik, 2019.

[2] H. K. Purwadaria, "Problems and Priorities of Grain Drying in Indonesia," in *Grain Drying in Asia: Proceeding of an International Conference held at the 74 FAO Regional Office for Asia and the Pacific, ACIAR Proceedings No. 71*, Bangkok, Thailand, 1995, pp. 201–209.

[3] BSN, "Standar Nasional Indonesia Beras Giling," Badan Standardisasi Nasional, Jakarta, 2008.

[4] S. Syahrul, F. Hamdullahpur, and I. Dincer, "Exergy analysis of fluidized bed drying of moist particles," *Exergy, An Int. J.*, vol. 2, no. 2, pp. 87–98, 2002, doi: https://doi.org/10.1016/S1164-0235(01)00044-9.

[5] M. N. Ibrahim, M. S. H. Sarker, N. Ab Aziz, and P. Mohd Salleh, "Drying Performances and Milling Quality of Rice during Industrial Fluidized Bed Drying of Paddy in Malaysia," *Pertanika J. Sci. Technol.*, vol. 23, no. 2, pp. 297–309, 2015.

[6] M. S. H. Sarker, M. N. Ibrahim, N. Abdul Aziz, and M. S. Punan, "Energy and exergy analysis of industrial fluidized bed drying of paddy," *Energy*, vol. 84, pp. 131–138, 2015, doi: https://doi.org/10.1016/j.energy.2015.02.064.

[7] S. Janjai, N. Srisittipokakun, and B. K. Bala, "Experimental and modelling performances of a roof-integrated solar drying system for drying herbs and spices," *Energy*, vol. 33, no. 1, pp. 91–103, 2008, doi: https://doi.org/10.1016/j.energy.2007.08.009.

[8] A. R. Celma and F. Cuadros, "Energy and exergy analyses of OMW solar drying process," *Renew. Energy*, vol. 34, no. 3, pp. 660–666, 2009, doi: https://doi.org/10.1016/j.renene.2008.05.019.

[9] J. Banout, P. Ehl, J. Havlik, B. Lojka, Z. Polesny, and V. Verner, "Design and performance evaluation of a Double-pass solar drier for drying of red chilli (Capsicum annum L.)," *Sol. Energy*, vol. 85, no. 3, pp. 506–515, 2011, doi: https://doi.org/10.1016/j.solener.2010.12.017.

[10] A. Fudholi, K. Sopian, M. A. Alghoul, M. H. Ruslan, and M. Y. Othman, "Performances and improvement potential of solar drying system for palm oil fronds," *Renew. Energy*, vol. 78, pp. 561–565, 2015, doi: https://doi.org/10.1016/j.renene.2015.01.050.

[11] S. Janjai, P. Intawee, J. Kaewkiew, C. Sritus, and V. Khamvongsa, "A large-scale solar greenhouse dryer using polycarbonate cover: Modeling and testing in a tropical environment of Lao People's Democratic Republic," *Renew. Energy*, vol. 36, no. 3, pp. 1053–1062, 2011, doi: https://doi.org/10.1016/j.renene.2010.09.008.

[12] V. Palled, S. R. Desai, Lokesh, and M. Anantachar, "Performance evaluation of solar tunnel dryer for chilly drying," *Karnataka J. Agric. Sci.*, vol. 25, no. 4, pp. 472–474, 2012.

[13] N. Srisittipokakun, K. Kirdsiri, and J. Kaewkhao, "Solar drying of Andrographis paniculata using a parabolicshaped solar tunnel dryer," *Procedia Eng.*, vol. 32, pp. 839–846, 2012, doi: https://doi.org/10.1016/j.proeng.2012.02.021.

[14] J. Prasad and V. K. Vijay, "Experimental studies on drying of Zingiber officinale, Curcuma longa l. and Tinospora cordifolia in solar-biomass hybrid drier," *Renew. Energy*, vol. 30, no. 14, pp. 2097–2109, 2005, doi: https://doi.org/10.1016/j.renene.2005.02.007.

[15] A. Madhlopa and G. Ngwalo, "Solar dryer with thermal storage and biomass-backup heater," *Sol. Energy*, vol. 81, no. 4, pp. 449–462, 2007, doi: https://doi.org/10.1016/j.solener.2006.08.008.

[16] M. A. Leon and S. Kumar, "Design and Performance Evaluation of a Solar-Assisted Biomass Drying System with Thermal Storage," *Dry. Technol.*, vol. 26, no. 7, pp. 936–947, Jul. 2008, doi: https://doi.org/10.1080/07373930802142812.

[17] Hamdani, T. A. Rizal, and Z. Muhammad, "Fabrication and testing of hybrid solar-biomass dryer for drying fish," *Case Stud. Therm. Eng.*, vol. 12, pp. 489–496, 2018, doi: https://doi.org/10.1016/j.csite.2018.06.008.

[18] M. Yahya, "Design and Performance Evaluation of a Solar Assisted Heat Pump Dryer Integrated with Biomass Furnace for Red Chilli," *Int. J. Photoenergy*, vol. 2016, no. 1, p. 8763947, Jan. 2016, doi: https://doi.org/10.1155/2016/8763947.

[19] M. Mohanraj, "Performance of a solar-ambient hybrid source heat pump drier for copra drying under hot-humid weather conditions," *Energy Sustain. Dev.*, vol. 23, pp. 165–169, 2014, doi: https://doi.org/10.1016/j.esd.2014.09.001.

[20] M. Yahya, A. Fudholi, H. Hafizh, and K. Sopian, "Comparison of solar dryer and solar-assisted heat pump dryer for cassava," *Sol. Energy*, vol. 136, pp. 606–613, 2016, doi: https://doi.org/10.1016/j.solener.2016.07.049.

[21] M. Yahya, "Performance Analysis of Solar Assisted Fluidized Bed Dryer Integrated Biomass Furnace with and without Heat Pump for Drying of Paddy," *Int. J. Photoenergy*, vol. 2016, no. 1, p. 3801918, Jan. 2016, doi: https://doi.org/10.1155/2016/3801918.

[22] Y. Qiu, M. Li, R. H. E. Hassanien, Y. Wang, X. Luo, and Q. Yu, "Performance and operation mode analysis of a heat recovery and thermal storage solar-assisted heat pump drying system," *Sol. Energy*, vol. 137, pp. 225–235, 2016, doi: https://doi.org/10.1016/j.solener.2016.08.016.

[23] M. Aktaş, A. Khanlari, B. Aktekeli, and A. Amini, "Analysis of a new drying chamber for heat pump mint leaves dryer," *Int. J. Hydrogen Energy*, vol. 42, no. 28, pp. 18034–18044, 2017, doi: https://doi.org/10.1016/j.ijhydene.2017.03.007.

[24] T. A. Yassen and H. H. Al-Kayiem, "Experimental investigation and evaluation of hybrid solar/thermal dryer combined with supplementary recovery dryer," *Sol. Energy*, vol. 134, pp. 284–293, 2016, doi: https://doi.org/10.1016/j.solener.2016.05.011.

[25] F. Xiang, L. Wang, and X. Yue, "Exergy Analysis and Experimental Study of a Vehicle-Mounted Heat Pump–Assisted Fluidization Drying System Driven by a Diesel Generator," *Dry. Technol.*, vol. 29, no. 11, pp. 1313–1324, Sep. 2011, doi: https://doi.org/10.1080/07373937.2011.592044.

PISTON
Journal of Technical Engineering:

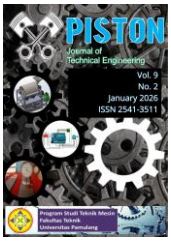

Analysis of Cooling Load Performance with CLTD Method Case Study: Al-Furqon Mosque

Ramadhan Haryo Dewanto[1,a)], Fahrudin[1], Damora Rhakasywi[1]

[1]*Mechanical Engineering, Faculty of Engineering, Universitas Pembangunan Nasional Veteran Jakarta, Depok, 16514, Indonesia*

E-mail: [a)] 2110311005@mahasiswa.upnvj.ac.id

Received: Desember 30, 2025 *Revision: January 02, 2026* *Accepted: January 10, 2026*

Abstract: Thermal comfort in worship spaces is an important aspect that affects the quality of religious activities. However, intermittently occupied worship spaces, such as mosques during Jummah prayers, often experience spikes in heat load due to the accumulation of sensible and latent heat from occupants and solar radiation. This study aims to analyze the actual cooling load and determine the cooling load required to achieve a comfortable room temperature based on the Cooling Load Temperature Difference (CLTD) method. Temperature measurements were taken using data loggers at one outdoor point and nine indoor points during five Fridays between October 10 and November 7, 2025, from 11:00 a.m. to 1:00 p.m. Western Indonesian Time. Cooling load calculations were based on occupancy variations of 100, 300, and 600 people and comfort temperature targets of 23°C, 25°C, and 27°C. The results showed that the temperature in the worship hall was well above the thermal comfort limit. The actual cooling load increased significantly between 12:00 p.m. and 1:00 p.m. WIB and during peak occupancy, reaching a peak load of 570,116.3 Btu/h. To achieve a comfortable room temperature, the cooling capacity needs to be increased by 8–35%. The final capacity recommendation based on the measurements and ASHRAE standards ranges from 44–69 TR. It can be concluded that the cooling system of Al-Furqon Mosque is currently under capacity and requires increased capacity and adaptive operational strategies to achieve thermal comfort in intermittently occupied worship spaces in a tropical climate.

Keywords: CLTD, Cooling Load, Temperature, Prayer Room.

Abstrak: *Kenyamanan termal pada ruang ibadah menjadi aspek penting yang memengaruhi kualitas aktivitas keagamaan. Namun, ruang ibadah berokupansi intermiten, seperti masjid saat salat Jumat, sering mengalami lonjakan beban panas akibat akumulasi panas sensibel dan laten dari penghuni serta radiasi matahari. Penelitian ini bertujuan untuk menganalisis beban pendingin aktual dan menentukan kebutuhan beban pendingin yang diperlukan untuk mencapai temperatur kenyamanan ruang berdasarkan metode Cooling Load Temperature Difference (CLTD). Pengukuran temperatur dilakukan menggunakan data logger pada satu titik luar ruangan dan sembilan titik dalam ruangan selama lima hari Jumat antara 10 Oktober hingga 7 November 2025 pada rentang waktu 11.00–13.00 WIB. Perhitungan beban pendingin dilakukan berdasarkan variasi okupansi 100, 300, dan 600 orang serta target temperatur kenyamanan 23°C, 25°C, dan 27°C. Hasil penelitian menunjukkan bahwa temperatur ruang ibadah berada jauh di atas batas kenyamanan termal. Beban pendingin aktual meningkat signifikan pada pukul 12.00–13.00 WIB dan saat okupansi padat, dengan beban puncak mencapai 570.116,3 Btu/h. Untuk mencapai temperatur kenyamanan ruang, kapasitas pendingin perlu ditingkatkan sebesar 8%–35%. Rekomendasi kapasitas akhir berdasarkan hasil pengukuran dan standar ASHRAE berkisar antara 44–69 TR. Dapat disimpulkan bahwa sistem pendingin Masjid Al-Furqon saat ini berada dalam kondisi under-capacity dan memerlukan peningkatan kapasitas serta strategi operasional yang adaptif untuk mencapai kenyamanan termal pada ruang ibadah berokupansi intermiten di iklim tropis.*

Kata kunci: *CLTD, Beban Pendingin, Temperatur, Ruang Ibadah.*

INTRODUCTION

Places of worship play a crucial role as venues for spiritual and social activities of the community. Thermal comfort in worship spaces affects the quality of worship and influences the concentration of worshippers

[1]. Thermal comfort is greatly influenced by HVAC design [2]. Therefore, comprehensive cooling load calculations are required for HVAC systems to support thermal comfort in worship spaces.

Cooling Load Temperature Difference (CLTD) is a cooling load calculation method developed by ASHRAE that estimates heat transfer into a room through building elements based on equivalent temperature differences corrected for solar radiation, building orientation, and climate conditions. Previous studies have analyzed cooling loads in buildings and rooms using the CLTD method. Saeed et al. (2025) [3] calculated the cooling load of a mosque in Duhok, Iraq, using three methods, including traditional CLTD, Carrier HAP, and Revit. The results showed that the CLTD method produced the lowest cooling load, while the HAP and Revit calculations were approximately 2.33% and 2.93% higher than CLTD, respectively. This difference occurred because the assumptions and calculation processes for each method were different. The use of the CLTD method is supported by research by Jaya et al. (2020) [4], who analyzed the cooling load of the Dhammasala room at Padumuttara Temple in Sumatra, Indonesia. From the initial condition of a hot room with an average temperature of around 28.6°C, a recommendation was obtained to use an HVAC cooling system in the form of a chiller with a capacity of around 30–40 TR, with the aim of lowering the room temperature to a comfortable zone. These findings confirm that the CLTD method can be used to determine AC capacity.

Research related to cooling load analysis in worship spaces has also been conducted by Alqadhi et al. (2019) [5] at AlFahad Mosque, Saudi Arabia, using the E20 method with CLTD and HAP software. The manual CLTD method produced a total cooling capacity that was 8.8% greater than that of the HAP software. Although the CLTD method provided a higher value, both results were still within a range that was feasible for the mosque's needs. This study emphasizes that CLTD can be used for initial load estimation, but differences with the software must be taken into account when designing an AC system. Additionally, Prawibowo et al. (2024) [6] conducted research comparing cooling load calculations for hotel buildings using the traditional CLTD method with Carrier HAP 5.01. It was found that CLTD consistently provided higher cooling load estimates, with a difference of 3%–14% compared to HAP calculations. The HAP analytical method calculates hourly loads and usage schedules. The largest differences occurred in large rooms with extensive glass areas and high internal loads. These results indicate that HAP is more accurate for detailed design, while CLTD is useful for quick initial estimates. This research provides important findings for selecting calculation methods that meet HVAC design accuracy requirements.

Based on the literature reviewed previously, there are important points related to the CLTD method and its application. The Cooling Load Temperature Difference (CLTD) method developed by ASHRAE is one of the most effective methods for determining the cooling load of a room. This method considers various factors such as building orientation, material type, number of occupants, and local climate conditions [7]. However, research using this method has not yet been widely applied to worship spaces with intermittent occupancy in tropical climates such as Indonesia. This research gap indicates that the thermal comfort of worship spaces in Indonesia is often overlooked. Therefore, this study is necessary to determine the current cooling load and the cooling load required to achieve a comfortable temperature in worship spaces such as the Al-Furqon Mosque in Bekasi City, Indonesia. This study was conducted by measuring the temperature difference between the outdoor temperature, influenced by solar radiation, and the indoor temperature, followed by calculating heat transfer performance using the CLTD method. Thus, the cooling load can be calculated using this method.

METHODS

Cooling Load Temperature Difference (CLTD) Method

Cooling load calculations are necessary to determine the required HVAC system capacity [8]. The method commonly used for calculating cooling load is the CLTD method [9]. CLTD is a method for calculating cooling load that combines the temperature difference between indoor and outdoor air, daily temperature range, solar radiation, and heat from building construction [10]. This method is divided into two parts, namely external load and internal load.

External load is the load resulting from outdoor heat transfer through walls, roofs, floors, window glass, doors, and partitions, as shown in Equations (1), (2), (4), (5), and (6), as well as infiltration and ventilation loads in Equations (7) and (8) [11]. The cooling load calculation in this study refers to the *ASHRAE Handbook Fundamentals* [8].

$$Q_{wall} = U_{wall} \times A_{wall} \times CLTD_{corr} \quad (1)$$

$$Q_{roof} = U_{roof} \times A_{roof} \times CLTD_{corr} \quad (2)$$

$$CLTD_{corr} = \{(CLTD + LM) \times K + (25.5 - T_r) + (T_o - 29.4) \times f\} \quad (3)$$

$$Q_{glass} = \left(U_{glass} \times \Delta T \times A_{glass}\right) + \left(A_{kaca} \times SC \times SHGF \times CLF\right) \quad (4)$$

$$Q_{door} = U_{door} \times A_{door} \times \Delta T \quad (5)$$

$$Q_{partition} = U_{partition} \times A_{partition} \times \Delta T \quad (6)$$

$$Q_{s,inf\ \&\ vent} = 1.23 \times CFM \times \Delta T \quad (7)$$

$$Q_{l,inf\ \&\ vent} = 3010 \times CFM \times \Delta\omega \quad (8)$$

The cooling load (Q), expressed in Btu/h, is determined using the overall heat transfer coefficient (U) of each building component, the corresponding surface area (A), and the corrected Cooling Load Temperature Difference ($CLTD_{corr}$) and air duct factor (f). Conductive heat transfer is calculated using the indoor–outdoor temperature difference (ΔT), while heat gain through glazing includes both conductive and solar radiation components influenced by the shading coefficient (SC), maximum solar heat gain factor (SHGF), and cooling load factor (CLF). In addition, sensible and latent heat gains due to infiltration and ventilation are determined based on the airflow rate (CFM) and the difference in indoor–outdoor humidity ratio (Δω) [8].

In addition to external loads, internal loads are also generated within the room. These loads originate from heat produced by occupants, as shown in Equations (9) and (10), as well as from lamps and other electronic equipment, as shown in Equations (11), (12), and (13) [12].

$$Q_{s,human} = n \times SHG \times CLF \quad (9)$$

$$Q_{l,human} = n \times LHG \quad (10)$$

$$Q_{lighting} = P_{lamp} \times Ballast\ Factor \times CLF \quad (11)$$

$$Q_{s,electronics} = Heat\ Gain \times CLF \quad (12)$$

$$Q_{l,electronics} = Heat\ Gain \quad (13)$$

Internal cooling loads originate from occupants, lighting systems, and electronic equipment within the conditioned space. Occupant-related heat gains are calculated based on the number of occupants (n), considering both sensible heat gain (SHG) and latent heat gain (LHG) resulting from human activity, with the sensible component adjusted using the cooling load factor (CLF) to account for occupancy duration. Heat gains from lighting are determined using the installed lamp power and ballast factor, corrected by the cooling load factor to reflect the actual thermal contribution to the space. In addition, electronic equipment contributes sensible and latent heat depending on its operating characteristics. All internal heat gain components are summed to obtain the total internal cooling load, which is combined with the external cooling load to determine the overall cooling load required for HVAC system design [8].

Experimental Setup and Data Analysis Method

The CLTD cooling load calculation method requires actual measurements of outdoor and indoor temperatures in the worship space. Therefore, temperature measurements were taken using a Tzone Digital Temperature and Humidity Data Logger at 10 points, consisting of one point outside and nine points inside the room. The object of this study is the prayer room of Al-Furqon Mosque, located on Jalan Boulevard Hijau Raya, Kelurahan Pejuang, Kecamatan Medan Satria, Bekasi City, Indonesia. The geographical coordinates of the location are latitude −6.18706 and longitude 106.98105823743266. A sketch of the Al-Furqon Mosque prayer room is shown in Figure 1, where the X marks indicate the temperature measurement points.

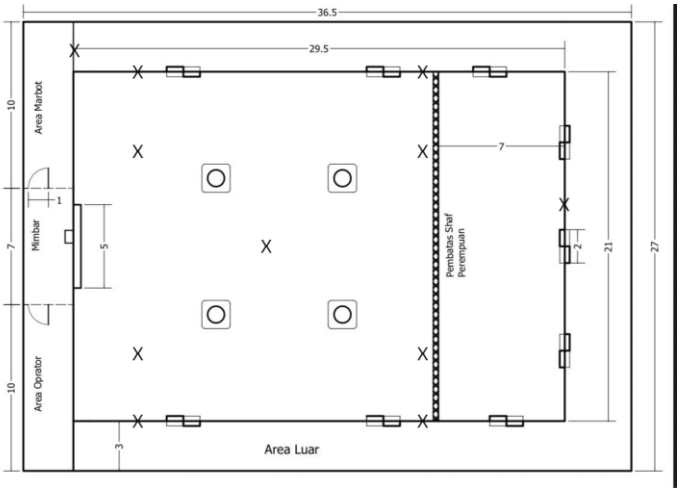

Figure 1. Sketch of the Prayer Hall of Al-Furqon Mosque

Room construction greatly affects the required cooling load [13]. The construction details of the Al-Furqon Mosque prayer room are shown in Table 1. Based on the floor plan and construction of the Al-Furqon Mosque, the heat transfer coefficient values, $CLTD_{corr}$, and SCL for each component are presented in Table 2 [14]. In addition to these components, other coefficients were obtained from ASHRAE standards and brand specifications, including U-values for walls, roof, doors, windows, infiltration and ventilation, as well as electronic heat gain and lamp ballast factors.

Table 1. Construction Details of the Al-Furqon Mosque

Component	Size	Quantity
Floor	619.5 m²	-
Wall area	21 m × 29.5 m × 9 m	4
Wall thickness	0.15 m	-
Door	2 m × 4 m	9
Glass window	2 m × 4 m	12
LED light	15 W	36
TV	-	2
Microphone	-	4
Passive speaker	-	9

Table 2. Room Component Variable Values

Component	U-Value (Btu/h·ft²·°F)	CLTD (°F)				SCL (°F)				SC
		U	S	T	B	U	S	T	B	
Roof	0.32	77	77	77	77	-	-	-	-	-
Walls	0.49	4	9	21	8	-	-	-	-	-
Doors	1.51	4	9	21	-	-	-	-	-	-
Door	1.04	4	9	21	-	8.475	11.23	15.373	-	1
Floor	0.217	-	-	-	-	-	-	-	-	-

The density of room occupancy during working hours and the comfortable room temperature need to be considered to determine their impact on the cooling load [15]. Therefore, based on the average number of visitors, the occupancy rate in this study was varied into low occupancy (100 people), medium occupancy (300 people), and high occupancy (600 people). Additionally, this study measured temperatures from before to after Friday prayers (11:00 a.m. to 1:00 p.m. WIB) at one-minute intervals on Fridays over one month (October 10 to November 7, 2025). This period was selected because these hours and days represent peak occupancy times. In accordance with SNI 03-6572-2001, the comfortable room temperature range is between 23°C and 27°C. To compare the actual cooling load with the cooling load required for comfortable room temperatures, this study also calculated the cooling load needed to achieve comfort at temperature variations of 23°C, 25°C, and 27°C.

RESULT AND DISCUSSION

Temperature Measurement Results

The results of outdoor and indoor temperature measurements are shown in Figure 2. In general, the outdoor temperature trend over the five Fridays showed a gradual increase until it peaked at around 13:00 WIB. Friday, October 31, recorded the highest outdoor temperature of 39.1°C, making it the day with the most extreme environmental thermal conditions during the observation period. On the other hand, indoor temperatures showed a similar pattern on each measurement day, with peak increases occurring around 12:00 p.m. This increase is related to high occupancy and Friday prayer activities taking place during that time frame, which increased latent and sensible heat indoors. These findings are in line with the study by Al-Homoud et al. (2021) [15], which reported that rooms with intermittent occupancy experience a surge in heat load during peak activity hours.

Overall, the indoor temperature did not reach the thermal comfort zone. The average room temperature was recorded at 31.32°C, with a minimum temperature of 29.26°C and a maximum of 33.30°C. These values are well above the comfort temperature range of 23°C to 27°C according to SNI 03-6572-2001. This condition indicates that the available cooling capacity is unable to effectively lower the room temperature during periods of increased activity and occupancy, consistent with the findings of Li, X., and Yao, R. (2020) [16] on buildings with high occupant density.

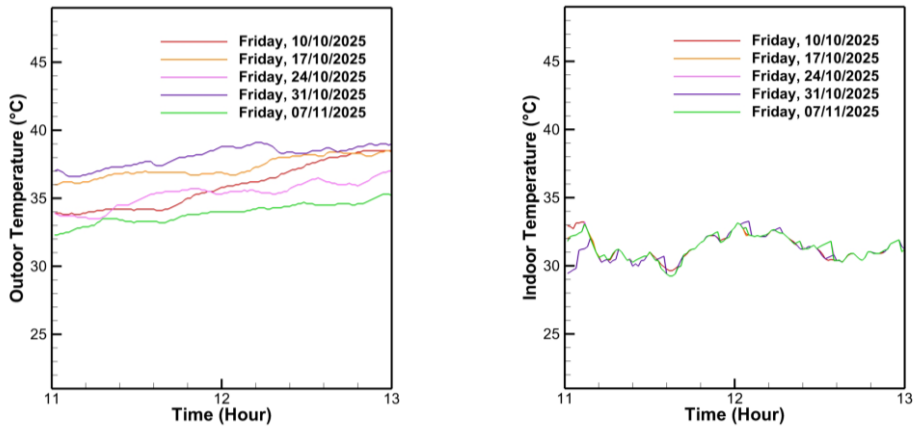

(a) (b)

Figure 2. Temperature Measurement Results: (a) Outdoor (surrounding environment), (b) Indoor

Cooling Load Calculation Results

The actual cooling load calculation results are shown in Figure 3. The actual cooling load was calculated based on the difference between the outdoor and indoor temperatures measured over five Fridays. The graph shows a consistent increase in cooling load between 12:00 p.m. and 1:00 p.m. This increase is due to a combination of higher ambient temperatures and an increase in the number of occupants during Friday prayers. These findings are in line with the study by Larhlida A et al. (2025) [13], which states that worship spaces with intermittent occupancy experience a significant surge in cooling load during peak hours of activity.

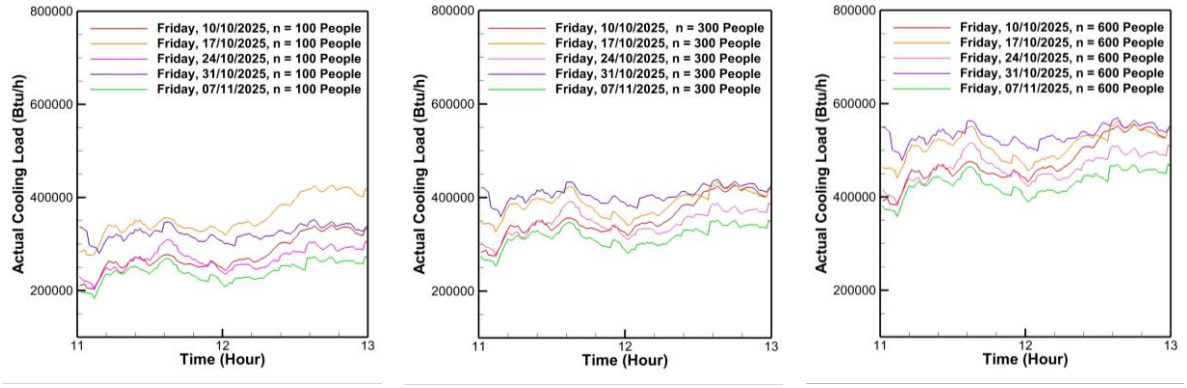

(a) (b) (c)

Figure 3. Actual Cooling Load Calculation Results: (a) Low Occupancy (100 People), (b) Medium Occupancy (300 People), (c) High Occupancy (600 People)

Friday, October 31, 2025, was recorded as the day with the highest cooling load, corresponding to the maximum outdoor temperature. Under high occupancy conditions, the average cooling load reached 482,786.8 Btu/h, with a peak of 570,116.3 Btu/h. Meanwhile, at medium occupancy, the average cooling load was 362,981.2 Btu/h, with a peak of 439,622.9 Btu/h. At low occupancy, the average cooling load was 283,110.8 Btu/h, with a peak of 352,627.3 Btu/h. This increase in cooling load is consistent with the findings of Chen et al. (2023) [17], which show that an increase in occupancy can raise the cooling load of a room by up to 40%.

Based on these calculations, it appears that the currently available cooling capacity is insufficient to reduce the room temperature to the thermal comfort zone recommended by SNI 03-6572-2001 (23–27°C). This indicates that the existing cooling system is undercapacity for the actual load, especially under high occupancy conditions.

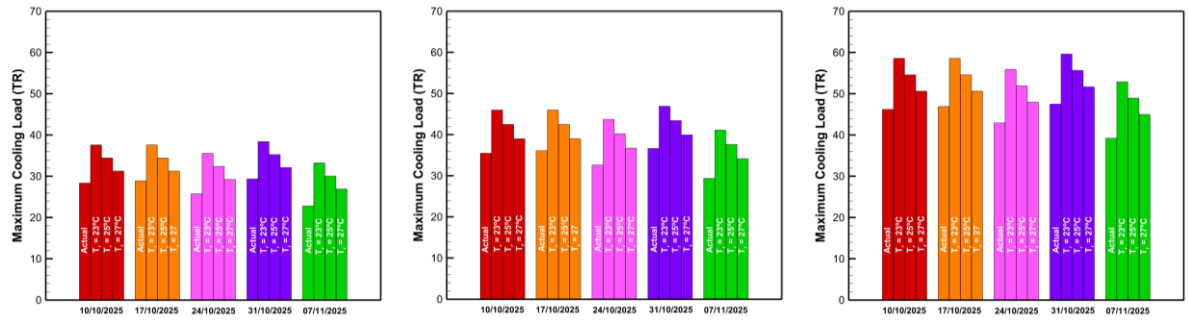

(a) (b) (c)

Figure 4. Comparison of Actual Maximum Cooling Load and Setpoint: (a) Low Occupancy (100 People), (b) Medium Occupancy (300 People), (c) High Occupancy (600 People)

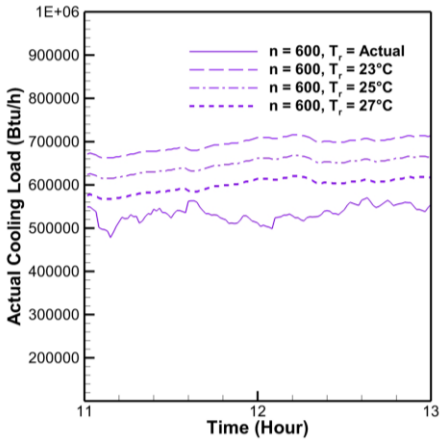

Figure 5. Comparison of Actual Cooling Load with Setpoints of 23°C, 25°C, and 27°C

The results of the cooling load calculations required to achieve comfortable room temperatures of 23°C, 25°C, and 27°C are shown in Figure 5. The graph presents calculation results based on the outdoor temperature and highest occupancy condition, which occurred on October 31, 2025, under high occupancy. It is clear that the current cooling capacity has not reached the level required to achieve thermal comfort. The average cooling load required to achieve a setpoint temperature of 23°C is 694,644.69 Btu/h, with a maximum value of 715,796.45 Btu/h under high occupancy. The average difference in cooling load for the 23°C setpoint is approximately 44% higher than the actual load during peak occupancy, while for the 25°C and 27°C setpoints, the differences are approximately 34% and 6% higher than the actual cooling load, respectively.

Analysis of peak cooling loads under both actual and setpoint conditions is necessary to determine the optimum cooling system capacity. The peak cooling load results for each condition are shown in a bar graph in Figure 6, expressed in TR (tons of refrigeration). The graph indicates that the existing cooling capacity must be increased to meet the cooling load required for comfortable room temperatures. To achieve a room temperature of 23°C, the cooling capacity needs to be increased by approximately 25% to 35% compared to the actual conditions. Meanwhile, to achieve the minimum comfort temperature of 27°C, the existing cooling capacity needs to be increased by approximately 8% to 15%. Based on occupancy variations, the cooling load required to achieve a temperature of 23°C is 38.43 TR at low occupancy, 46.91 TR at medium occupancy, and 59.65 TR at high occupancy. The relationship between the actual cooling load and the setpoint temperatures highlights the inadequacy of the currently available cooling capacity. These findings support the research by Mousavi Navaee, S. A. et al. (2025) [18], which emphasizes the relationship between setpoint temperature and cooling load.

In cooling system design, ASHRAE recommends a cooling load safety factor of approximately 15% to account for load uncertainty. With this factor applied, the recommended cooling capacities are approximately 44 TR for low occupancy, 54 TR for medium occupancy, and 69 TR for high occupancy, enabling the proposed system to achieve and maintain thermal comfort in accordance with SNI and ASHRAE standards.

CONCLUSIONS

This study successfully calculated the cooling load of the worship hall using the Cooling Load Temperature Difference (CLTD) method based on outdoor and indoor temperature measurements conducted over five Fridays and variations in room occupancy. The analysis results show that the current temperature of the worship hall is well above the thermal comfort range specified in SNI 03-6572-2001, indicating that the existing cooling system is unable to meet the comfort requirements of the space. The actual cooling load increases significantly during periods of high activity and occupancy, as well as on days with extreme ambient temperatures. Calculations of the cooling load required to achieve comfortable room temperatures indicate that the cooling capacity needs to be increased. Based on the analysis results and ASHRAE standards, the recommended cooling system capacity ranges from 44 to 69 TR, depending on the occupancy level. These findings confirm that cooling capacity planning for intermittently occupied worship spaces in tropical climates must consider daily load fluctuations, occupancy variations, and adequate design margins. In addition, this study provides insights into cooling system optimization, natural ventilation integration, and the use of building materials that are more adaptive to heat in order to improve the thermal comfort of worship spaces.

ACKNOWLEDGEMENT

The author would like to thank the management of DKM Masjid Al-Furqon, Bekasi City, for granting access and permission to conduct this research.

REFERENCES

[1] A. P. Sulistiawan, S. Wandri, E. Fauzan, and M. N. Bahari, "Thermal Comfort Investigation on Holy Mosque in Bandung Case Study : Lautze 2 Mosque Bandung," *J. Archit. Res. Educ.*, vol. 2, no. 1, pp. 82–89, 2020, doi: https://doi.org/10.17509/jare.v2i1.24105.

[2] J. C. Solano, E. Caamaño-Martín, L. Olivieri, and D. Almeida-Galárraga, "HVAC systems and thermal comfort in buildings climate control: An experimental case study," *Energy Reports*, vol. 7, pp. 269–277, 2021, doi: https://doi.org/10.1016/j.egyr.2021.06.045.

[3] D. N. Saeed, H. M. Rashad, B. SardarAbdullah, and Z. abdulghani Ramadhan, "Cooling Load Estimation in a Mosque: A Comparative Study of Traditional and Software-Based Methods," *IOP Conf. Ser. Earth Environ. Sci.*, vol. 1507, no. 1, p. 12074, 2025, doi: https://doi.org/10.1088/1755-1315/1507/1/012074.

[4] A. K. Jaya, C. O. Harahap, and R. Andarini, "Analisis Perhitungan Beban Pendinginan Ruang Dhammasala Vihara Padumuttara menggunakan Metode CLTD," *Ultim. Comput. J. Sist. Komput.*, vol. 12, no. 2, pp. 57–64, Nov. 2020, doi: https://doi.org/10.31937/sk.v12i2.1709.

[5] F. AlHarbi *et al.*, "Comparison of Cooling Load Calculations by E20 and HAP Software," *Univers. J. Mech. Eng.*, vol. 7, no. 5, pp. 285–298, 2019, doi: https://doi.org/10.13189/ujme.2019.070505.

[6] M. Prawibowo and Komarudin, "Comparative Analysis of Cooling Load Calculations: CLTD Method vs. Carrier HAP 5.01 Software for Hotel HVAC Design," *Int. J. Innov. Mech. Eng. Adv. Mater.*, vol. 6, no. 1, pp. 46–56, 2024, doi: http://dx.doi.org/10.22441/ijimeam.v6i1.23781.

[7] ASHRAE, "ANSI/ASHRAE Standard 55," *ASHRAE Standard 55*, vol. 2013. ASHRAE, 2020.

[8] C. Mao, J.-C. Baltazar, and J. S. Haberl, "Comparison of ASHRAE peak cooling load calculation methods," *Sci. Technol. Built Environ.*, vol. 25, no. 2, pp. 189–208, Feb. 2019, doi: https://doi.org/10.1080/23744731.2018.1510240.

[9] I. Omar, A. M. Mohsen, K. A. Hammoodi, and H. A. Al-Asadi, "Using total equivalent temperature difference approach to estimate air conditioning cooling load in buildings," *J. Eng. Therm. Sci.*, vol. 2, no. 1, pp. 59–68, 2022, doi: https://doi.org/10.21595/jets.2022.22684.

[10] A. Setyawan, "Effect of room temperature setting on the cooling load, supply air quantity, and apparatus dew point," *J. Eng. Sci. Technol.*, vol. 15, no. 3, pp. 1799–1814, 2020.

[11] H. Oktay, R. Yumrutaş, and M. Z. Işık, "Comparison of CLTD and TETD Cooling Load Calculation Methods for Different Building Envelopes," *Mugla J. Sci. Technol.*, vol. 6, no. 1, pp. 18–26, 2020, doi: https://doi.org/10.22531/muglajsci.631222.

[12] M. R. Fadilla and A. W. Biantoro, "Analisis Jumlah Beban Pendingin Pada Ruangan Test Stand Menggunakan Metode Cltd (Cooling Load Temperature Difference)," *J. Tek. Mesin*, vol. 11, no. 3, pp. 230–237, 2022, doi: https://dx.doi.org/10.22441/jtm.v11i3.15939.

[13] A. Larhlida, A. Mana, A. Fathi, B. Ouhammou, Z. Sadoune, and A. Jamil, "Towards Sustainable Mosques: A Review of AI and ML Approaches for Energy Use Forecasting," *Designs*, vol. 9, no. 6. p. 124, 2025. doi: https://doi.org/10.3390/designs9060124.

[14] R. Kalbasi and P. Hassani, "Buildings with less HVAC power demand by incorporating PCM into envelopes taking into account ASHRAE climate classification," *J. Build. Eng.*, vol. 51, p. 104303, 2022, doi: https://doi.org/10.1016/j.jobe.2022.104303.

[15] M. S. Al-Homoud and M. Krarti, "Energy efficiency of residential buildings in the kingdom of Saudi Arabia: Review

of status and future roadmap," *J. Build. Eng.*, vol. 36, p. 102143, 2021, doi: https://doi.org/10.1016/j.jobe.2020.102143.

[16] X. Li and R. Yao, "A machine-learning-based approach to predict residential annual space heating and cooling loads considering occupant behaviour," *Energy*, vol. 212, p. 118676, 2020, doi: https://doi.org/10.1016/j.energy.2020.118676.

[17] S. Chen *et al.*, "Occupant-centric dynamic heating and cooling loads simplified prediction model for urban community at energy planning stage," *Sustain. Cities Soc.*, vol. 90, p. 104406, 2023, doi: https://doi.org/10.1016/j.scs.2023.104406.

[18] S. A. Mousavi Navaee, A. Falavand Jozaei, A. Ghafouri, and M. Mahdavi Adeli, "The Impact of HVAC Setpoint Temperature on Reducing Building Energy Consumption in Different Climatic Regions of Iran," *J. Comput. Appl. Mech.*, vol. 56, no. 2, pp. 470–487, 2025, doi: https://doi.org/10.22059/jcamech.2025.391603.1400.

PISTON
Journal of Technical Engineering:

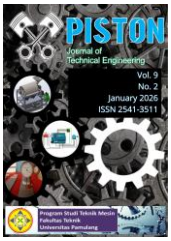

Utilization of Coconut Shells as a Source of Graphene Nanosheets Fe/N-GNS for Environmentally Friendly Primary Battery Electrodes

Giyanto[1], Jon Affi[1,a*)], Gunawarman[1], Murni Handayani[2], Yuli Yetri[3]

[1]*Department of Mechanical Engineering, Andalas University, Limau Manis Campus, Padang 25163, Indonesia*
[2]*Advanced Materials Research Center, National Research and Innovation Agency (BRIN), Indonesia*
[3]*Department of Mechanical Engineering, Padang State Polytechnic, Padang 25163, Indonesia*

E-mail: [a)] jon_affi@eng.unand.ac.id

Received: Desember 30, 2025 *Revision: January 05, 2026* *Accepted: January 11, 2026*

Abstract: The research on the performance of carbon (C)/d-orbital metals (graphite/graphene, graphene/N-graphene, graphite/Fe-graphene, graphite/Fe-N-graphene, and graphene/Fe-N-graphene) in primary battery electrode systems was carried out using a simple technology by mixing coconut shell powder with N and Fe. The purpose of this study was to determine the preparation method of Fe/GNS and Fe/N-GNS electrodes and to evaluate the performance of the electrolyte on electron distribution in Fe/GNS and Fe/N-GNS electrodes as primary battery anodes based on electrical conductivity values. This research was conducted as a laboratory experimental study. GNS and N-GNS were synthesized using a modified Hummers method, while Fe/GNS and Fe/N-GNS electrodes were synthesized using the impregnation method. GNS, N-GNS, Fe/GNS, and Fe/N-GNS after electrolyte combination were characterized using SEM–EDX and a multimeter, respectively. The SEM–EDX results at 170 °C and 500–600 °C showed a folded and wrinkled graphene structure with dispersed Fe (5.3 wt% by EDX), dominated by C and O. The addition of Fe–NH_3 acted as a catalyst to form more regularly structured graphite. The DHL test showed the highest electrical conductivity (~51,400 at 40 V) for Fe-N-GNS samples synthesized at 170 °C and 600 °C, which were identified as the most optimal synthesis conditions.

Keywords: Graphite/Fe-graphene, Graphene/Fe-N-graphene, Pyrolysis, Electrodes, Primary Battery.

Abstrak: *Penelitian ini mengkaji kinerja material karbon (C) berbasis logam d-orbital (grafit/graphene, graphene/N-graphene, grafit/Fe-graphene, grafit/Fe-N-graphene, dan graphene/Fe-N-graphene) sebagai sistem elektroda pada baterai primer. Material disintesis menggunakan teknologi sederhana melalui pencampuran serbuk tempurung kelapa dengan nitrogen (N) dan besi (Fe). Tujuan penelitian ini adalah menentukan metode preparasi elektroda Fe/GNS dan Fe/N-GNS serta mengevaluasi pengaruh elektrolit terhadap distribusi elektron pada elektroda Fe/GNS dan Fe/N-GNS sebagai anoda baterai primer berdasarkan nilai konduktivitas listrik. Penelitian dilakukan secara eksperimental di laboratorium. GNS dan N-GNS disintesis menggunakan metode Hummers termodifikasi, sedangkan elektroda Fe/GNS dan Fe/N-GNS disintesis menggunakan metode impregnasi. Karakterisasi morfologi dan komposisi unsur GNS, N-GNS, Fe/GNS, dan Fe/N-GNS setelah penambahan elektrolit dilakukan menggunakan SEM–EDX, sedangkan pengukuran konduktivitas listrik dilakukan menggunakan multimeter. Hasil SEM–EDX pada suhu 170 °C dan 500–600 °C menunjukkan struktur graphene yang terlipat dan berkerut dengan distribusi Fe yang merata (5,3 % berat berdasarkan EDX), dengan unsur dominan C dan O. Penambahan Fe–NH_3 berperan sebagai katalis dalam pembentukan struktur grafit yang lebih teratur. Uji DHL menunjukkan nilai konduktivitas listrik tertinggi (sekitar 51.400 pada tegangan 40 V) pada sampel Fe-N-GNS yang disintesis pada suhu 170 °C dan 600 °C, sehingga kondisi tersebut diidentifikasi sebagai kondisi sintesis paling optimal.*

Kata kunci: *Grafit/Fe-graphene, Graphene/Fe-N-graphene, Pirolisis, Elektroda, Baterai Primer.*

INTRODUCTION

The research institute of the Thai Institute of Technology and Science revealed that coconut shell charcoal has a calorific value of around 4,830 kcal/kg. Arif further stated that Indonesian coconut shell charcoal

has a higher calorific value, ranging from approximately 6,700 to 7,100 kcal/kg. This difference is attributed to Indonesia's fertile soil composition and its geographical location in a tropical climate, which are considered the main contributing factors [1]. The main components of charcoal include carbon, ash, moisture, nitrogen, and sulfur. In addition, some large pores are still covered by impurities such as tar and other organic compounds. Charcoal also contains inorganic elements, including magnesium (Mg), aluminum (Al), potassium (K), calcium (Ca), and iron (Fe), as reported by Rampe et al [2]. The results of artificial anode studies indicate that palm oil biomass can be utilized as a promising and low-cost material to improve the performance of microbial fuel cell (MFC) anodes [3]. This highlights the potential of biomass-derived carbon materials as sustainable electrode materials.

Graphene is a two-dimensional (2D) material that has attracted significant attention from researchers worldwide due to its outstanding properties, such as large specific surface area, excellent chemical stability, high electron mobility, and superior electrical conductivity [4]. Structurally, graphene has a honeycomb-like hexagonal crystal lattice and exhibits semimetallic behavior with a zero band gap [5]. Cheap and renewable coconut shell biomass waste can therefore be selected as a carbon source to prepare 2D graphite- and graphene-based electrode materials with excellent capacitive performance [6]. During the carbonization process, carbon is gradually transformed into graphite and subsequently into charcoal with a more ordered structure [7]. Furthermore, graphene or modified graphene sheets can also be produced from this biomass source [8].

Graphene nanosheets (GNS) and Fe/GNS were synthesized using a modified Hummers method combined with an impregnation technique [9]. Graphite oxide was reduced to graphene by dissolving the graphite oxide in distilled water, followed by ultrasonication for 90 minutes to obtain a homogeneous solution [10]. The resulting reduced graphene oxide (rGO) was then subjected to repeated washing and heating processes [11]. In related material processing studies, cellulose fibers were isolated from the bark of jicama tubers (*Pachyrhizus erosus*). A suspension consisting of distilled water, starch, and glycerol was mixed with various cellulose loadings (0, 2, 6, and 10 g) and gelatinized using a hot plate equipped with a magnetic stirrer. The biocomposite gel was subsequently sonicated using an ultrasonic probe (47.78 W/cm² for 4 minutes) [12]. Characterization of the synthesized materials was carried out using scanning electron microscopy (SEM), density measurements, and Vickers hardness number (VHN) analysis [13]. In addition, the development of low-cost potentiostats as electrochemistry-based analytical instruments was considered, while the roles of NH_3 and Fe as catalysts in improving the structural quality of graphene oxide (GO) reduction to rGO were evaluated. Further analyses included crystallinity and phase identification, morphology and compositional characterization, assessment of structural defects and regularity, functional group identification, and electrical conductivity measurements [14].

METHODS

The graphene material used in this study was synthesized from old coconut shells that had been dried and soaked in an aluminum kettle at temperatures of 170 °C and 220 °C for 2 hours. The coconut shells were then cleaned from coconut flesh and fibers and burned with an initial combustion at a temperature of 300 °C for 1 hour. After 1 hour, the temperature was increased to 500 °C and 600 °C for 1 hour. After becoming charcoal, the charcoal was ground using a mortar and sieved to a particle size of 200 mesh.

Coconut shell charcoal was soaked in distilled water in a test tube for 24 hours to clean the charcoal from impurities, then filtered using Whatman filter paper and dried at room temperature for 48 hours. The sample was then dried at a temperature of 90 °C for 1 hour and 30 minutes using a furnace. This process aimed to remove moisture content. The sonication process was carried out for 30 minutes, and the sample was dried at room temperature for 24 hours. Subsequently, the drying process was carried out using a 100 °C hotplate for 2.5 hours. The sample was then doped with 25% ammonia solution (NH_3) using a hotplate magnetic stirrer.

First, an Erlenmeyer was prepared and filled with 30 mL of aquadest. Then, 1.2 g of sample and 1 mL of NH_3 were added. The flask was placed on a hotplate and set to 100 °C, with stirring at 150 rpm. A magnetic stir bar was inserted into the Erlenmeyer flask, and a temperature sensor rod was placed inside the flask to detect the internal temperature. The heater and magnetic stirrer were then turned on. This process lasted for approximately 50 minutes. During this process, the moisture content in the sample evaporated due to heating. After approximately 50 minutes, the sample in the flask dried and returned to powder form, which was ready to be transferred into a sample bottle for the next step involving mixing with $FeCl_3$ and $NaBH_4$.

A total of 0.12 g of $FeCl_3$ was mixed with 100 mL of aquadest and stirred for 15 minutes using a magnetic stirrer at a speed of 300 rpm. 0.2 g of GNS was mixed with 200 mL of aquadest and then sonicated for 30 minutes. The $FeCl_3$ solution was then poured into the GNS suspension and stirred for 12 hours at 650 rpm. Subsequently, 0.12 g of $NaBH_4$ was mixed with 100 mL of aquadest and stirred for 15 minutes at 300 rpm. After completion,

the $NaBH_4$ solution was added to the GNS–$FeCl_3$ mixture and stirring was continued for 1 hour. After the stirring process was complete, the mixture was filtered using Whatman filter paper No. 42, then placed in a bowl and dried using a furnace at 60 °C for 6 hours until Fe–N doped graphene powder was obtained.

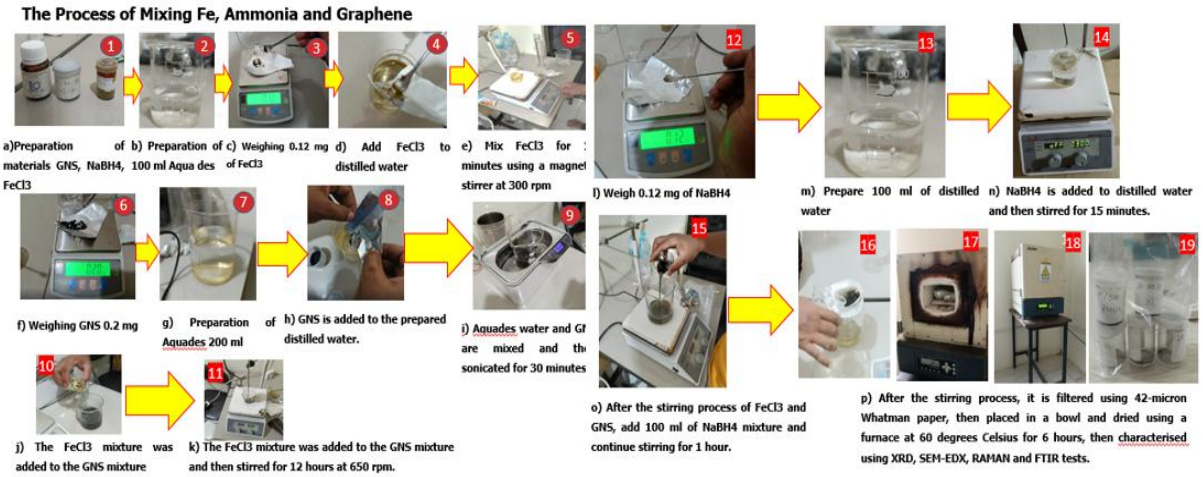

Figure 1. Synthesis process of Fe–N-doped GNS

SEM–EDX analysis was conducted at an accelerating voltage of 15.00 kV to observe the morphology of graphene (folded, wrinkled, and sheet-like structures) and to determine the elemental composition (C, O, and Fe). The electrical conductivity test was performed using a pellet compacted from approximately 1.00 g of sample and covered with a pellet holder. Crocodile clip cables were connected to the negative and positive terminals of a digital multimeter and a regulated DC power supply. Electrical conductivity was measured by applying voltage variations of 40, 44, 48, 51, and 55 V, while recording the corresponding current values. The instrument used for this conductivity test was a multitester power supply, which functions as a device to supply electric current with various voltage levels.

RESULT AND DISCUSSION

SEM–EDX Test Results of Pyrolysis at 170 °C, 500 °C, and 600 °C (Fe–N-Doped GNS)

SEM examination was carried out on graphite, graphite oxide, and graphene samples to observe the morphology of graphene resulting from Fe doping using 0.12 g of $FeCl_3$ and 0.12 g of $NaBH_4$ to form Fe–N-GNS. Figure 2(a) shows morphological differences in the graphene samples, where graphene appears in the form of small flakes irregularly dispersed. After oxidation into graphite oxide, the morphology changes into thicker layered structures, which then revert to graphene after the reduction process. The particle dispersion shows the presence of white spots scattered over the surface of the GNS sheets; these particles correspond to Fe nanoparticles formed during the pyrolysis process.

The EDX results indicate that the main constituent is carbon (75.7%), corresponding to graphene nanosheets, followed by iron (5.3%), which confirms the successful doping of Fe nanoparticles, and oxygen (19.0%), originating from residual functional groups formed during the synthesis and oxidation processes. Figure 2(b) shows a wrinkled, sheet-like, and folded GNS morphology with Fe nanoparticles dispersed as white spots on the surface. However, the number of these particles appears reduced and more uniformly distributed compared to the sample pyrolyzed at 500 °C.

The EDX analysis further reveals that the carbon content increases significantly from 75.7% to 87.5%, indicating that pyrolysis at 600 °C is more effective in reducing oxygen-containing functional groups and improving the crystallinity of the GNS carbon framework. The oxygen content decreases from 19.0% to 10.5%, supporting the effectiveness of thermal reduction, while the iron content decreases from 5.3% to 2.0%, likely due to phase transformation of Fe crystals resulting in a smoother and more homogeneous distribution.

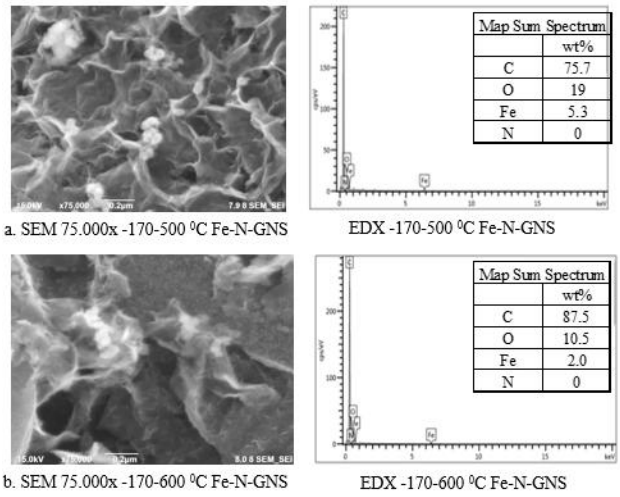

Figure 2. SEM images (75,000×) and EDX spectra of Fe–N-doped GNS: (a) pyrolysis at 500 °C and (b) pyrolysis at 600 °C after baking at 170 °C

Conductivity Test

Electrical conductivity tests were conducted at baking temperatures of 170 °C and 220 °C and pyrolysis temperatures of 500 °C (Fe–N-GNS) and 600 °C (Fe–N-doped GNS) using a compressed pellet with a mass of approximately 0.50 g under various applied voltage conditions. The electrical conductivity was determined based on the relationship between voltage and current using the equations $R = V/I$ and $\mathrm{DHL} = 1/R$. The complete electrical conductivity data obtained from these measurements are presented in Tables 1 and 2.

Table 1. Electrical conductivity of Fe–N-doped GNS after baking at 170 °C and pyrolysis at 500 °C

Voltage (V)	Current (μA)	Resistance (Ω)	Conductivity (μS)
40	2033	0.019675356	50.825
44	2102	0.020932445	47.772
48	2198	0.021838034	45.791
51	2224	0.022931654	43.607
55	2344	0.023464163	42.618

Table 2. Electrical conductivity of Fe–N-doped GNS after baking at 170 °C and pyrolysis at 600 °C

Voltage (V)	Current (μA)	Resistance (Ω)	Conductivity (μS)
40	2056	0.019455252	51.400
44	2282	0.019281332	51.863
48	2328	0.020618556	48.500
51	2359	0.021619330	46.254
55	2421	0.022717885	44.018

Based on the conductivity graphs, current measurements were conducted at voltages of 40, 44, 48, 51, and 55 V to evaluate electrical conductivity accuracy and stability. The results indicate that graphene exhibits relatively stable electrical behavior, with a gradual decrease in conductivity corresponding to increasing voltage. This behavior suggests controlled electron mobility, attributed to graphene's ability to store charge carriers and release electrons gradually, resulting in stable electrical performance.

CONCLUSIONS

1. SEM analysis at a baking temperature of 170 °C and pyrolysis temperatures of 500 °C and 600 °C for Fe–N-doped GNS, observed at a magnification of 75,000×, reveals that the morphology of Fe–N-GNS particles consists of tightly packed structures resembling graphene sheets. The EDX results confirm the successful incorporation of iron (Fe) into the graphene-based material, with a relatively high Fe content of 5.3 wt%. Carbon is identified as the dominant element, while oxygen is present as residual functional groups originating from the synthesis process.
2. Electrical conductivity decreases with increasing applied voltage. The highest conductivity value (~51.4 μS at 40 V) was obtained for Fe–N-doped GNS synthesized under baking at 170 °C and pyrolysis at 600 °C, indicating that these conditions are the most optimal for achieving superior electrical conductivity.

ACKNOWLEDGEMENT

The authors would like to express their gratitude to all parties who contributed to the completion of this research. Special thanks are extended to the National Research and Innovation Agency (BRIN) for providing access to materials characterization facilities.

REFERENCES

[1] A. Hidayat, S. Setiadji, and E. P. Hadisantoso, "Sintesis Oksida Grafena Tereduksi (rGO) dari Arang Tempurung Kelapa (Cocos nucifera)," *Al Kim. J. Ilmu Kim. Dan Terap.*, vol. 5, no. 2, pp. 68–73, 2019, doi: https://doi.org/10.15575/ak.v5i2.3810.

[2] V. A. Tiwow, M. J. Rampe, H. L. Rampe, and A. Apita, "Pola Inframerah Arang Tempurung Kelapa Hasil Pemurnian Menggunakan Asam," *Chem. Prog.*, vol. 14, no. 2, pp. 116–123, 2021, doi: https://doi.org/10.35799/cp.14.2.2021.37191.

[3] A. A. Yaqoob, M. N. M. Ibrahim, A. S. Yaakop, K. Umar, and A. Ahmad, "Modified graphene oxide anode: A bioinspired waste material for bioremediation of Pb2+ with energy generation through microbial fuel cells," *Chem. Eng. J.*, vol. 417, no. December, p. 128052, 2021, doi: https://doi.org/10.1016/j.cej.2020.128052.

[4] J. Affi *et al.*, "Electrochemical and capacitive behavior of reduced graphene oxide from green reduction of graphene oxide by urea for supercapacitor electrodes," *J. Mater. Sci. Mater. Electron.*, vol. 34, no. 22, p. 1638, 2023, doi: https://doi.org/10.1007/s10854-023-11076-4.

[5] N. A. Putri, "Sintesis Reduced Graphene Oxide (rGO) Dengan Metode Hummer Termodifikasi," Universitas Islam Negeri Maulana Malik Ibrahim, 2021.

[6] L. Sun *et al.*, "From coconut shell to porous graphene-like nanosheets for high-power supercapacitors," *J. Mater. Chem. A*, vol. 1, no. 21, pp. 6462–6470, 2013, doi: https://doi.org/10.1039/C3TA10897J.

[7] T. M. Radadiya, "A Properties of Graphene," *Eur. J. Mater. Sci.*, vol. 2, no. 1, pp. 6–18, 2015, doi: https://doi.org/10.37745/ejms.2014.

[8] M. P. Lavin-Lopez *et al.*, "Synthesis and characterization of graphene: influence of synthesis variables," *Phys. Chem. Chem. Phys.*, vol. 16, no. 7, pp. 2962–2970, 2014, doi: DOI https://doi.org/10.1039/C3CP54832E.

[9] R. Siburian *et al.*, "Distribution model of Iron (Fe) on Fe/Graphene Nano Sheets," *Ceram. Int.*, vol. 49, no. 17, Part B, pp. 28571–28579, 2023, doi: https://doi.org/10.1016/j.ceramint.2023.06.110.

[10] D. A. Safitri, D. Susanti, and H. Nurdiansyah, "Analisis Pengaruh Doping Nitrogen Terhadap Sifat Kapasitif Superkapasitor Berbahan Graphene," *J. Tek. ITS*, vol. 6, no. 1, pp. 90–95, 2017.

[11] X. Hong and D. D. L. Chung, "Exfoliated graphite with relative dielectric constant reaching 360, obtained by exfoliation of acid-intercalated graphite flakes without subsequent removal of the residual acidity," *Carbon N. Y.*, vol. 91, no. 716, pp. 1–10, 2015, doi: https://doi.org/10.1016/j.carbon.2015.04.042.

[12] F. Hafizulhaq, H. Abral, A. Kasim, S. Arief, and J. Affi, "Moisture Absorption and Opacity of Starch-Based Biocomposites Reinforced with Cellulose Fiber from Bengkoang," *Fibers*, vol. 6, no. 3. p. 62, 2018. doi: https://doi.org/10.3390/fib6030062.

[13] A. Indra, R. B. Setiawan, I. H. Mulyadi, J. Affi, and Gunawarman, "The effect of PVA addition as binders on the properties of hydroxyapatite sintered body," in *Proceedings of the 2nd International Conference on Industrial and Technology and Information Design, ICITID 2021*, Yogyakarta: EAI, 2021. doi: http://dx.doi.org/10.4108/eai.30-8-2021.2311514.

[14] I. Anshori *et al.*, "ESPotensio: A Low-Cost and Portable Potentiostat With Multi-Channel and Multi-Analysis Electrochemical Measurements," *IEEE Access*, vol. 10, pp. 112578–112593, 2022, doi: https://doi.org/10.1109/ACCESS.2022.3213725.

PISTON
Journal of Technical Engineering:

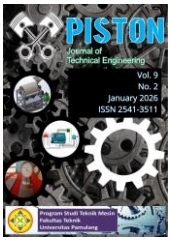

Synthesis of Graphene-Like Carbon from Coconut Shell and Electrical Conductivity Properties

Nur Rohmat[1], Jon Affi[1,a*)], Gunawarman[1], Murni Handayani[2], Yuli Yetri[3]

[1]*Department of Mechanical Engineering, Andalas University, Limau Manis Campus, Padang 25163, Indonesia*
[2]*Research Center for Nanotechnology Systems, National Research and Innovation Agency (BRIN), Indonesia*
[3]*Department of Mechanical Engineering, Padang State Polytechnic, Padang 25163, Indonesia*

E-mail: [a)] jon_affi@eng.unand.ac.id

Received: Desember 30, 2025 *Revision: January 07, 2026* *Accepted: January 14, 2026*

Abstract: Demand for batteries continues to increase in line with the growth of electric vehicles, while the availability of lithium in nature is limited. One alternative is the use of renewable natural materials, such as coconut shells, to produce functional carbon materials. This study aims to synthesize graphene-like carbon (GLC) from coconut shells using pyrolysis and sonication methods. The process was carried out through drying at 150–200 °C and pyrolysis at 700 °C. XRD characterization showed main peaks at 2θ ≈ 23.11° and 43.75° (150 °C/700 °C), and 23.15° and 43.38° (200 °C/700 °C), with an interlayer spacing of 0.35 nm and a shift in the C (002) peak from pure graphite, indicating the formation of nanosized graphene layers. FTIR analysis confirmed the presence of O–H, aromatic C=C, C=O, and C–O groups, indicating a hexagonal carbon framework with oxygen functionality on the surface. The Raman spectrum showed ID/IG ratios of 0.84 and 0.83, indicating structural disorder while still consistent with graphene-like characteristics. Conductivity tests showed relatively stable electrical conductivity with gradual electron energy loss at small current increases, allowing better control of electron mobility.

Keywords: Graphene-like carbon (GLC), Coconut shell, Pyrolysis, Sonication, Functional carbon materials.

Abstrak: *Permintaan baterai terus meningkat seiring dengan pertumbuhan kendaraan listrik, sementara ketersediaan litium di alam semakin terbatas. Salah satu alternatif yang dapat dikembangkan adalah pemanfaatan bahan alam terbarukan, seperti tempurung kelapa, untuk menghasilkan material karbon fungsional. Penelitian ini bertujuan untuk mensintesis graphene-like carbon (GLC) dari tempurung kelapa melalui metode pirolisis dan sonikasi. Proses sintesis dilakukan melalui tahap pengeringan pada suhu 150–200 °C dan pirolisis pada suhu 700 °C. Karakterisasi XRD menunjukkan puncak utama pada 2θ ≈ 23,11° dan 43,75° (150 °C/700 °C), serta 23,15° dan 43,38° (200 °C/700 °C), dengan jarak antar-lapis sebesar 0,35 nm serta pergeseran puncak C (002) dari grafit murni, yang mengindikasikan terbentuknya lapisan grafena berukuran nano. Analisis FTIR mengonfirmasi keberadaan gugus O–H, C=C aromatik, C=O, dan C–O, yang menunjukkan kerangka karbon heksagonal dengan keberadaan gugus oksigen pada permukaan. Spektrum Raman menunjukkan rasio ID/IG sebesar 0,84 dan 0,83, yang mengindikasikan adanya ketidakteraturan struktur namun masih konsisten dengan karakteristik graphene-like. Uji konduktivitas menunjukkan nilai konduktivitas listrik yang relatif stabil dengan kehilangan energi elektron yang bertahap pada peningkatan arus yang kecil, sehingga memungkinkan kontrol mobilitas elektron yang lebih baik.*

Kata kunci: *Graphene-like carbon (GLC), Tempurung kelapa, Pirolisis, Sonikasi, Material karbon fungsional.*

INTRODUCTION

The demand for high-energy-density storage systems continues to increase along with the growth of electrical appliances and electric vehicles. Lithium-ion batteries (LIBs) have been used as the dominant energy source for electronic equipment. However, large-scale commercial production of LIBs faces severe challenges, including limited natural resources, high production costs, and post-consumer waste. The need for high-performance and low-cost batteries is driven by the growth of the electromobility market to meet key requirements such as adequate driving range and fast-charging capabilities. The development of efficient and cost-effective energy storage systems is essential for creating a renewable energy-based power supply. Graphite has dominated

the market share of anode materials to date. Carbon-based materials are widely adopted and play an important role in mankind's culture [1].

Graphene is considered one of the most remarkable achievements in the field of science and technology. Single-layer hexagonal crystals of graphite, which represent the simplest form of carbon materials with a C–C bond distance of 0.142 nm, have received great attention in the fields of sensors, biomedicine, composite materials, and microelectronics [2], [3]. A wide variety of applications such as conductive transparent films, ultra-sensitive chemical sensors, thin-film transistors, quantum dot devices, and anti-corrosion coatings have been tested and established. Industrial-scale production of graphene for these applications relies heavily on the scalability and simplicity of synthesis methods. This factor was a major bottleneck in the past but has been significantly improved in recent years [4].

Along with its unique quantum confinement phenomena, graphene exists in several forms such as graphene nanoribbons, nanosheets, nanoplates, and three-dimensional graphene. The electronic and quantum properties of graphene remain subjects of fundamental research. Each carbon atom in graphene is sp^2-hybridized and forms three covalent bonds with neighboring carbon atoms. The sp^2 hybridization results from the combination of s, p_x, and p_γ orbitals, leaving one free electron per carbon atom. This free electron occupies the p_z orbital, which lies perpendicular to the graphene plane and forms a π bond. The p_z orbitals play an important role in determining the chemical and physical behavior of graphene [5]. Owing to its ability to accommodate a wide variety of intercalants and alloying species, graphite can be considered a versatile electrode material for use in sodium-ion batteries and potassium-ion batteries. However, graphite in various forms such as natural graphite, synthetic graphite, soft carbon, and hard carbon still suffers from significant crystal structure expansion during charge–discharge cycles under high-power conditions.

METHODS

Preparation of Graphene-Like Carbon

This study employed a pyrolysis method to produce graphene-like carbon (GLC) sheets from coconut shells. The process was initiated with a preliminary combustion step at temperatures of 150 °C and 200 °C for 2 hours. This was followed by pyrolysis at 300 °C for 1 hour and further pyrolysis at 700 °C for 1 hour. Sonication was subsequently performed for 1 hour to assist in the exfoliation of carbon layers. Prior to the pyrolysis process, coconut shell powder was soaked in distilled water for 72 hours. The soaked material was then dried for 1 hour and subsequently dried on a hot plate at a temperature of 100 °C for 1 hour.

RESULT AND DISCUSSION

Characterization of Graphene like carbon

It is well known that the diffraction peak of pure graphite appears at 2θ around 26° due to its interlayer spacing of 0.335 nm [6]. The X-ray diffraction (XRD) patterns of coconut shell–derived carbon were analyzed for samples dried at temperatures of 150 °C and 200 °C, followed by pyrolysis at 700 °C, as illustrated in Figure 1. The results confirm the formation of graphene-like structures from coconut shells under the applied conditions.

For samples dried at 150 °C and subsequently pyrolyzed, diffraction peaks were observed at 2θ around 23.11° and 43.75°. Meanwhile, samples dried at 200 °C and pyrolyzed under the same conditions exhibited diffraction peaks at 2θ around 23.15° and 43.38°. These results are consistent with previous studies reporting similar diffraction characteristics for graphene-like carbon materials [1], [7], [8].

Based on Figure 1(a), variations in the drying temperature do not significantly affect the diffraction characteristics of the samples. This is indicated by the relatively similar peak positions observed in each sample, suggesting the successful formation of graphene-like carbon. In addition, a slight shift of the diffraction peaks toward lower angles compared to pure graphite was observed, which is commonly associated with increased interlayer spacing and structural disorder in graphene-like carbon materials [9]. The weak intensity of the diffraction peaks further indicates the presence of nanosized graphene layers with limited stacking order within the carbon structure [10].

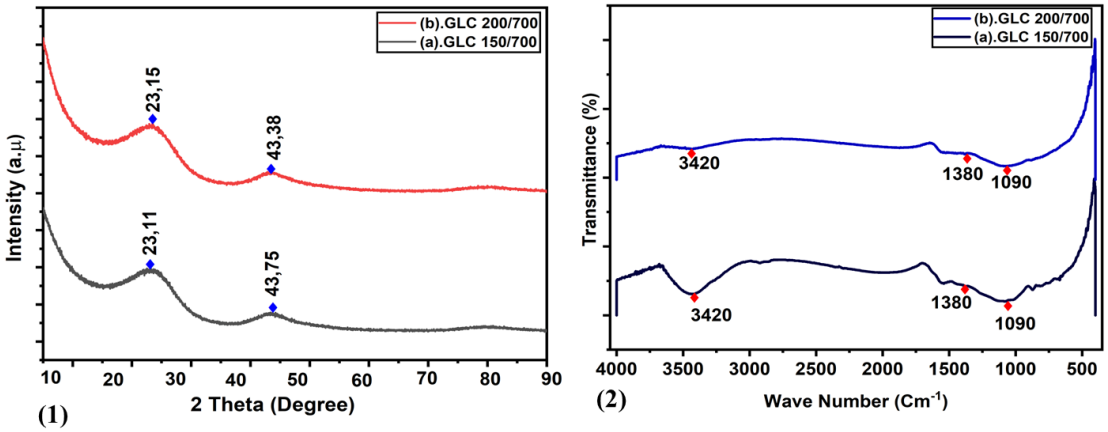

Figure 1. (a) XRD patterns and (b) FTIR spectra of graphene-like carbon derived from coconut shells

Figure 1(b) presents the FTIR spectra of graphene-like carbon obtained from coconut shells at a drying temperature of 150 °C followed by pyrolysis at 700 °C. A strong and broad absorption band observed at approximately 3420 cm^{-1} corresponds to O–H stretching vibrations, indicating the presence of hydroxyl groups on the surface of the material. This confirms the existence of oxygen-containing functional groups in the graphene-like carbon structure. An absorption band at around 1380 cm^{-1} is associated with C–H bending vibrations, which typically indicate the presence of methyl groups (–CH_3), particularly symmetric bending modes. In addition, the band observed at approximately 1090 cm^{-1} corresponds to C–O stretching vibrations, suggesting that single carbon–oxygen bonds remain within the carbon framework [11], [12].

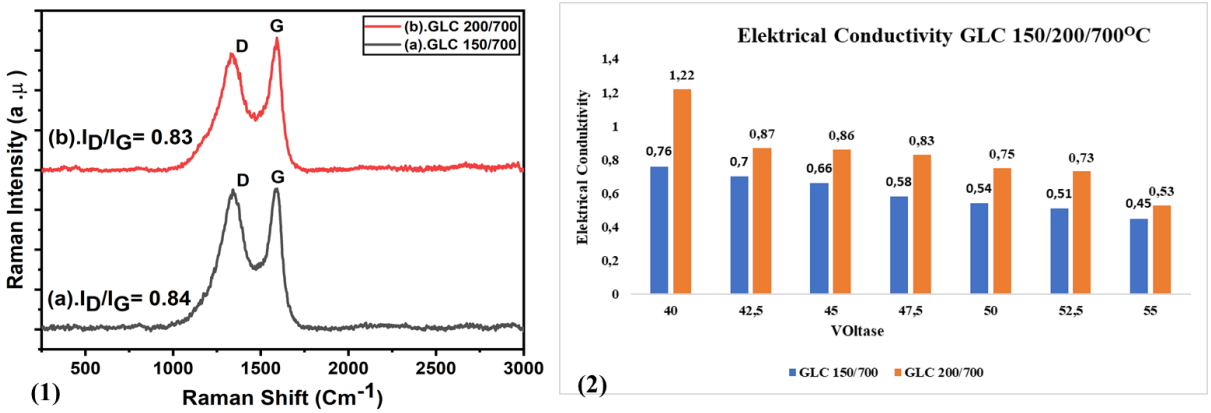

Figure 2. (a) Raman spectra and (b) electrical conductivity of graphene-like carbon derived from coconut shells

Figure 2(a) shows the Raman spectra of graphene-like carbon samples. The Raman spectrum of the sample dried at 150 °C and pyrolyzed at 700 °C exhibits two dominant peaks at 1342.67 cm^{-1} corresponding to the D band and 1592.87 cm^{-1} corresponding to the G band, with an ID/IG ratio of 0.84, indicating the presence of structural disorder. Meanwhile, the sample dried at 200 °C and pyrolyzed at 700 °C shows dominant peaks at 1340.65 cm^{-1} for the D band and 1592.91 cm^{-1} for the G band, with an ID/IG ratio of 0.83. These results indicate similar structural characteristics for both samples and are consistent with previous studies on graphene-like carbon derived from biomass materials [13], [14].

Figure 2(b) presents the electrical conductivity behavior of graphene-like carbon samples under varying applied voltages. Electrical conductivity measurements were performed using approximately 0.40 g of sample placed inside a fuse holder and covered with a fuse cap. Alligator clips were connected to the positive and negative terminals of a digital multimeter and a DC power supply. The applied voltages were varied at 40 V, 42.5 V, 45 V, 47.5 V, 50 V, 52.5 V, and 55 V, while the current was maintained at 9 A.

At an applied voltage of 40 V, the sample dried at 150 °C and pyrolyzed at 700 °C exhibited a current of 0.76 µA, which decreased to 0.45 µA at 55 V. In contrast, the sample dried at 200 °C and pyrolyzed at 700 °C produced a higher current of 1.22 µA at 40 V and 0.53 µA at 55 V. These results indicate that the combination of drying at 200 °C and pyrolysis at 700 °C produces graphene-like carbon with improved electrical conductivity and lower initial resistance compared to the sample dried at 150 °C. The observed conductivity behavior suggests good electrical stability of graphene-like carbon, characterized by gradual electron energy loss at relatively small current changes. This behavior enables more effective control of electron mobility and supports stable electrical conduction, which is advantageous for extending the service life of graphene-based battery materials [15], [16].

CONCLUSIONS

Graphene-like carbon (GLC) was successfully synthesized from coconut shells through drying at temperatures of 150 °C to 200 °C followed by pyrolysis at 700 °C. XRD, FTIR, and Raman characterizations confirmed the formation of a graphene-like nanostructure with oxygen-containing functional groups. Electrical conductivity measurements demonstrated relatively stable electrical properties under varying applied voltages. Overall, the results indicate that graphene-like carbon derived from coconut shells has strong potential as a sustainable carbon-based functional material for energy-related applications.

ACKNOWLEDGEMENT

The authors gratefully acknowledge all parties who contributed to the completion of this research. This work was supported by the Directorate of Higher Education of Indonesia through Andalas University under the National Competitive Research Program, Doctoral Dissertation Research scheme, with contract number 28/UN16.19/PT.01.03/PL/2024. The authors also express their sincere gratitude to the National Research and Innovation Agency of Indonesia (BRIN) for providing access to material characterization facilities.

REFERENCES

[1] N. Rohmat *et al.*, "The effect of nitrogen doped graphene-like carbon synthesized from coconut shell on conductivity property," *AIP Conf. Proc.*, vol. 3223, no. 1, p. 50010, Jan. 2025, doi: https://doi.org/10.1063/5.0243954.

[2] K. C. Wasalathilake, H. Li, L. Xu, and C. Yan, "Recent advances in graphene based materials as anode materials in sodium-ion batteries," *J. Energy Chem.*, vol. 42, pp. 91–107, 2020, doi: https://doi.org/10.1016/j.jechem.2019.06.016.

[3] S. K. Tiwari, S. Sahoo, N. Wang, and A. Huczko, "Graphene research and their outputs: Status and prospect," *J. Sci. Adv. Mater. Devices*, vol. 5, no. 1, pp. 10–29, 2020, doi: https://doi.org/10.1016/j.jsamd.2020.01.006.

[4] Y. Yetri, R. F. Nuradi, R. Rusdianasari, S. Mulyadi, and D. Tashima, "Optimizing the Eco-Friendly Electrode Analysis from Theobroma cacao Peels Activated Carbon," *Int. J. Thin Film Sci. Technol.*, vol. 14, no. 2, pp. 97–104, 2025, doi: http://dx.doi.org/10.18576/ijtfst/140204.

[5] A. K. Sood *et al.*, "Review of Graphene Technology and Its Applications for Electronic Devices," *Graphene - New Trends Dev.*, 2015, doi: https://doi.org/10.5772/61316.

[6] Q. Xie *et al.*, "Reed straw derived active carbon/graphene hybrids as sustainable high-performance electrodes for advanced supercapacitors," *J. Solid State Electrochem.*, vol. 20, no. 2, pp. 449–457, 2016, doi: https://doi.org/10.1007/s10008-015-3061-y.

[7] M. Supeno and R. Siburian, "New route: Convertion of coconut shell tobe graphite and graphene nano sheets," *J. King Saud Univ. - Sci.*, vol. 32, no. 1, pp. 189–190, 2020, doi: https://doi.org/10.1016/j.jksus.2018.04.016.

[8] F. M. Wachid, A. Y. Perkasa, F. A. Prasetya, N. Rosyidah, and Darminto, "Synthesis and characterization of nanocrystalline graphite from coconut shell with heating process," *AIP Conf. Proc.*, vol. 1586, pp. 202–206, 2014, doi: https://doi.org/10.1063/1.4866759.

[9] T. Hu *et al.*, "Rapid synthesis of nitrogen-doped graphene for a lithium ion battery anode with excellent rate performance and super-long cyclic stability," *Phys. Chem. Chem. Phys.*, vol. 16, no. 3, pp. 1060–1066, 2014, doi: http://dx.doi.org/10.1039/C3CP54494J.

[10] A. Y. Nugraheni, M. Nashrullah, F. A. Prasetya, F. Astuti, and Darminto, "Study on Phase, Molecular Bonding, and Bandgap of Reduced Graphene Oxide Prepared by Heating Coconut Shell," *Mater. Sci. Forum*, vol. 827, pp. 285–289, 2015, doi: https://doi.org/10.4028/www.scientific.net/MSF.827.285.

[11] G. Lombardo, B. Ebin, M. R. St. J. Foreman, B.-M. Steenari, and M. Petranikova, "Chemical Transformations in Li-Ion Battery Electrode Materials by Carbothermic Reduction," *ACS Sustain. Chem. Eng.*, vol. 7, no. 16, pp. 13668–13679, Aug. 2019, doi: https://doi.org/10.1021/acssuschemeng.8b06540.

[12] M. Handayani *et al.*, "Fabrication of Graphene Oxide/Calcium Carbonate/Chitosan Nanocomposite Film with Enhanced Mechanical Properties," *IOP Conf. Ser. Mater. Sci. Eng.*, vol. 578, p. 012073, 2019, doi: https://doi.org/10.1088/1757-899X/578/1/012073.

[13] A. Eckmann *et al.*, "Probing the Nature of Defects in Graphene by Raman Spectroscopy," *Nano Lett.*, vol. 12, no. 8, pp. 3925–3930, Aug. 2012, doi: https://doi.org/10.1021/nl300901a.

[14] Y.-R. Kim *et al.*, "Green supercapacitor patterned by synthesizing MnO/laser-induced-graphene hetero-nanostructures on wood via femtosecond laser pulses," *Biochar*, vol. 6, no. 1, p. 36, 2024, doi: https://doi.org/10.1007/s42773-024-00320-7.

[15] R. R. Simanjuntak, R. Siburian, F. Sebayang, F. Y. S. T. Hutagalung, S. P. Aritonang, and C. Simanjuntak, "Performance of electrodes Mg/Graphene nanosheet (GNS) and Mg/N-Graphene nanosheet (N-GNS) as anode of battery," *IOP Conf. Ser. Mater. Sci. Eng.*, vol. 1122, p. 012088, 2021, doi: https://doi.org/10.1088/1757-899x/1122/1/012088.

[16] F. Y. S. T. Hutagalung, R. Siburian, and M. Supeno, "The performance conductivity of Mg/Graphene nanosheet as anode of battery," *IOP Conf. Ser. Mater. Sci. Eng.*, vol. 1122, p. 012090, 2021, doi: https://doi.org/10.1088/1757-899x/1122/1/012090.

PISTON
Journal of Technical Engineering:

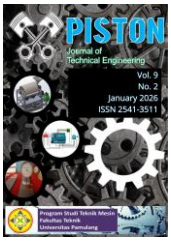

Performance Analysis of a Two-Stage Savonius Rotor Using Numerical Methods

Abdul Aziz[1], Hilfama Rama[1], M. Firash Al-Huda[1], Mirwan Zahndi[1], Ruzita Sumiati[1,a)]

[1]*Politeknik Negeri Padang, Kampus Street, Limau Manis, Pauh District, Padang City, West Sumatra 25164, Indonesia*

E-mail: [a)] ruzitasumiati@pnp.ac.id

Received: October 19, 2025 *Revision: January 07, 2026* *Accepted: January 14, 2026*

Abstract: The POCREN system is a hybrid renewable energy device that integrates wind, solar, and water current energy sources to generate electrical power. The main objective of developing POCREN is to provide a sustainable electricity supply, particularly for floating fish farmers in coastal regions where the average wind speed ranges from 3 to 5 m/s. Currently, most floating cage farmers rely heavily on diesel engines to meet their electricity needs, which are costly and environmentally unsustainable. This study focuses on one of the key components of the POCREN system, namely a two-stage Savonius wind turbine, to evaluate its performance in power generation. The analysis was conducted numerically using ANSYS Fluent software. The results show that the maximum power coefficient (Cp) of the two-stage turbine was achieved at a wind speed of 5 m/s with a tip speed ratio (TSR) of 0.7, yielding a Cp value of 0.26. At a lower wind speed of 3 m/s, the maximum Cp reached 0.22 at the same TSR of 0.7. Pressure contour analysis indicates that the two-stage Savonius turbine can operate effectively at low wind speeds of approximately 3 m/s. The pressure distribution shows higher pressure on the concave side of the advancing blade compared to the convex side, generating torque that drives rotor rotation. This confirms that the two-stage configuration enhances torque continuity and enables stable operation under low wind conditions. Based on these findings, the two-stage Savonius turbine in the POCREN system is suitable for renewable energy applications in coastal environments, offering a promising alternative to reduce dependence on diesel-powered generators for floating fish farming activities.

Keywords: Energy Conversion, POCREN, Vertical Axis Wind Turbine, Power Coefficient (Cp), Torque Coefficient (Ct), Two-Stage Savonius.

Abstrak: *Sistem POCREN merupakan perangkat energi terbarukan hibrida yang mengintegrasikan sumber energi angin, energi surya, dan energi arus air untuk menghasilkan daya listrik. Tujuan utama pengembangan sistem POCREN adalah menyediakan pasokan listrik yang berkelanjutan, khususnya bagi petani ikan keramba terapung di wilayah pesisir dengan kecepatan angin rata-rata berkisar antara 3 hingga 5 m/s. Saat ini, sebagian besar petani ikan keramba masih bergantung pada mesin diesel untuk memenuhi kebutuhan listrik, yang memiliki biaya operasional tinggi dan berdampak negatif terhadap lingkungan. Penelitian ini berfokus pada salah satu komponen utama sistem POCREN, yaitu turbin angin Savonius dua tingkat, untuk mengevaluasi kinerjanya dalam menghasilkan daya listrik. Analisis dilakukan secara numerik menggunakan perangkat lunak ANSYS Fluent. Hasil penelitian menunjukkan bahwa koefisien daya maksimum (Cp) pada turbin dua tingkat dicapai pada kecepatan angin 5 m/s dengan nilai tip speed ratio (TSR) sebesar 0.7, menghasilkan Cp sebesar 0.26. Pada kecepatan angin yang lebih rendah, yaitu 3 m/s, nilai Cp maksimum sebesar 0.22 juga diperoleh pada TSR yang sama. Analisis kontur tekanan menunjukkan bahwa turbin Savonius dua tingkat mampu beroperasi secara efektif pada kecepatan angin rendah, sekitar 3 m/s. Distribusi tekanan memperlihatkan tekanan yang lebih tinggi pada sisi cekung bilah yang menerima aliran angin dibandingkan dengan sisi cembung, sehingga menghasilkan torsi yang memutar rotor. Hal ini membuktikan bahwa konfigurasi dua tingkat dapat meningkatkan kontinuitas torsi dan memungkinkan operasi yang stabil pada kondisi kecepatan angin rendah. Berdasarkan hasil tersebut, turbin Savonius dua tingkat pada sistem POCREN dinilai layak untuk diaplikasikan sebagai sumber energi terbarukan di lingkungan pesisir dan berpotensi mengurangi ketergantungan petani ikan keramba terapung terhadap generator berbahan bakar diesel.*

Kata kunci: *Konversi Energi, POCREN, Turbin Angin Sumbu Vertikal, Koefisien Daya (Cp), Koefisien Torsi (Ct), Savonius Dua Tingkat.*

INTRODUCTION

Wind energy is one of the renewable energy sources with abundant availability; however, its utilization remains relatively limited. This energy source has significant potential to be developed for power generation applications. The main advantage of wind energy lies in its environmentally friendly nature, as it produces no CO_2 emissions and therefore does not contribute to greenhouse gas accumulation [1]. The conversion of wind energy into useful power is achieved using a wind turbine, which is a mechanical system that transforms the kinetic energy of wind into mechanical or electrical energy [2]. The amount of energy generated by a wind turbine is strongly influenced by wind velocity and the swept area of the turbine blades [3]–[8].

In most regions of Indonesia, wind velocities are relatively low. Under low wind speed conditions, Savonius-type wind turbines are commonly employed due to their excellent self-starting capability [9]. However, Savonius turbines generally exhibit lower efficiency compared to other types of wind turbines, making performance optimization an important research focus. The performance of a Savonius turbine is commonly evaluated using two key parameters, namely the power coefficient (Cp) and the torque coefficient (Ct) [10]. The power coefficient represents the effectiveness of a turbine in converting wind kinetic energy into mechanical or electrical power. Numerous studies have investigated methods to improve Cp and Ct values through geometric modifications in order to achieve optimal turbine performance [10]–[15]. The efficiency of a Savonius turbine is influenced by several design parameters, including overlap ratio, number of blades, number of stages, end plates, and guide vanes [16].

Among these parameters, the number of stages plays a significant role in improving turbine performance. Previous studies have reported that two-stage Savonius turbines exhibit higher efficiency compared to single-stage or multi-stage configurations. Yuli Setyo I et al. [17] reported that a two-stage rotor equipped with an additional valve achieved a 68 percent reduction in static torque fluctuation, a 4 percent increase in maximum power, and a 17 percent improvement in the average static torque coefficient. Anuj Kumar et al. [18] reported a maximum power coefficient of 0.44 for a two-stage turbine operating at a tip speed ratio of 0.9, based on numerical analysis. Muhammad Syahmy Mohd Halmy et al. [19] demonstrated that a two-blade configuration in a double-stage turbine produced higher torque and output power compared to other design models. Dundun M. P. analyzed torque distribution, velocity flow patterns, and power coefficient values, and reported that a modified two-stage Savonius turbine achieved the highest Cp among the tested configurations. Mounia Zemamou et al. [20] also stated that among Savonius rotors with identical aspect ratios, the highest Cp value was obtained from a two-stage configuration.

Based on the aforementioned background, this study presents a numerical analysis to evaluate the performance of a two-stage Savonius turbine with a modified blade geometry derived from the conventional Savonius design. The blade geometry is arc-shaped and obtained by cutting a circular profile, which constitutes the main novelty of this study. The modified Savonius turbine is implemented as a component of a power generation system known as POCREN (Portable Combined Renewable Energy). The POCREN system is designed to utilize three renewable energy sources, namely wind, solar, and water currents, and is illustrated in Figure 1.

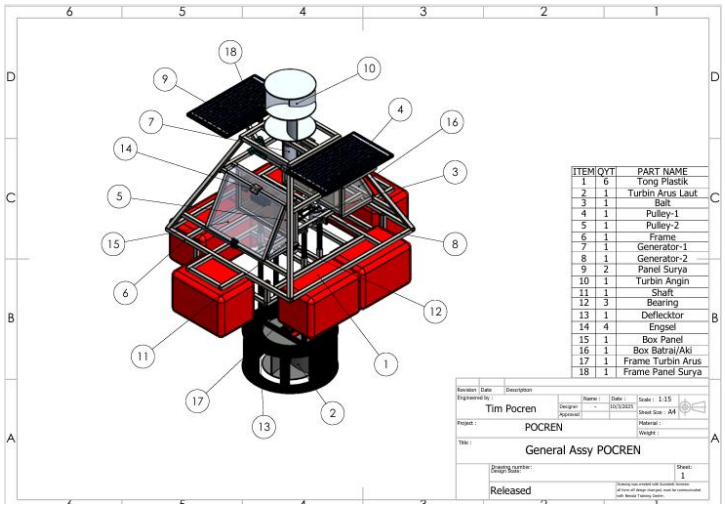

Figure 1. POCREN

One of its key components is a two-stage Savonius wind turbine. The primary objective of this study is to numerically evaluate the performance of the two-stage Savonius turbine integrated into the POCREN system.

METHODS

Geometry Details

The turbine model was developed using SolidWorks software, and the detailed geometric configuration is shown in Figure 2. The POCREN wind turbine employs a two-bladed, two-stage Savonius rotor with an overlap ratio of 0.15 and an aspect ratio of 1.

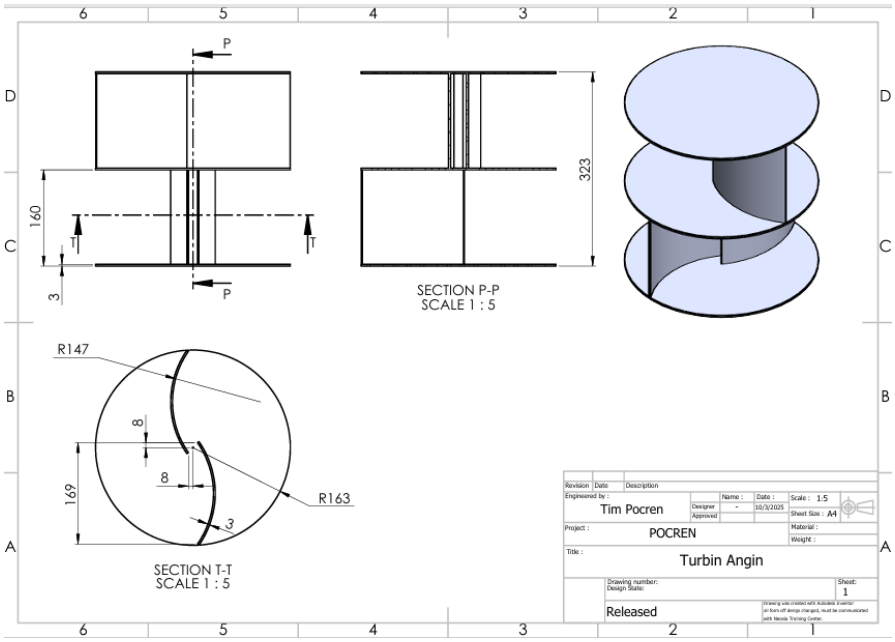

Figure 2. Dimensional Details

Mathematical Model

The performance of the Savonius turbine is evaluated using two main parameters, namely the torque coefficient (Ct) and the power coefficient (Cp). Turbine performance is commonly presented as a function of the tip speed ratio (TSR), which is defined as the ratio between the tangential velocity at the rotor tip and the free-stream wind velocity. The following mathematical expressions are used to quantify the performance of the Savonius turbine:

$$C_p = \frac{P}{P_A} \tag{1}$$

where:

$$P_A = \frac{1}{2}\rho A U^3 \tag{2}$$

$$P = T.\omega \tag{3}$$

$$C_T = \frac{T}{T_A} = \frac{T}{\frac{1}{2}\rho A U^2 R} \tag{4}$$

$$TSR\ (\lambda) = \frac{\omega R}{U} \tag{5}$$

Air density is denoted by ρ (kg·m^{-3}), while the free-stream wind speed is represented by U (m·s^{-1}). The rotor radius is denoted by R (m), and the rotor swept area A is expressed in m^2; for a Savonius rotor, the swept area is defined as A = D·H, where H is the blade height. The measured torque acting on the rotor shaft is represented by T (N·m), and the angular velocity of the rotor is denoted by ω (rad·s^{-1}). The tip-speed ratio (λ) is defined as the ratio of the blade tip speed to the free-stream wind speed, given by λ = ωR/U. The mechanical power extracted by the rotor (P) is calculated as the product of torque and angular velocity (P = Tω), while the power available in the wind (P_a) is given by P_a = ½ρAU^3.

Numerical Method

The present study employs Computational Fluid Dynamics (CFD) analysis using ANSYS software. The computational domain configuration is illustrated in Figure 3. The domain is divided into two regions, namely a stationary region and a rotating region that contains the turbine blades.

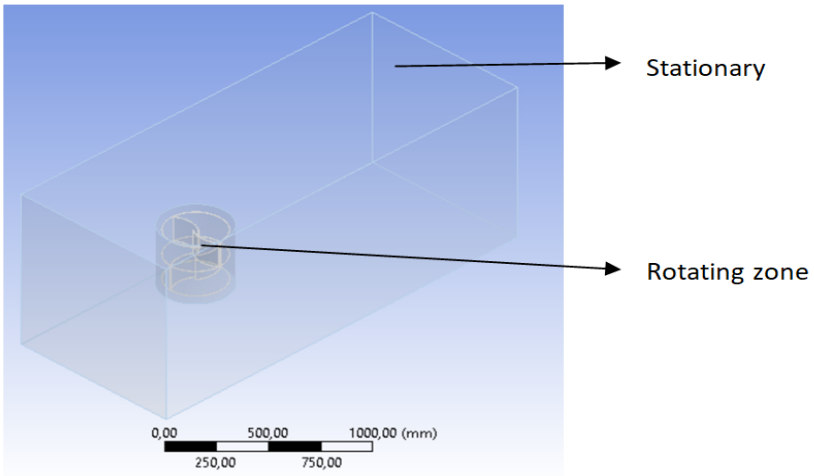

Figure 3. Computational Domain

The three-dimensional computational domain was discretized using unstructured triangular meshes. Mesh refinement was applied in the vicinity of the rotor blades, where additional inflation layers were introduced along the blade surfaces to accurately capture near-wall flow behavior, as shown in Figure 4.

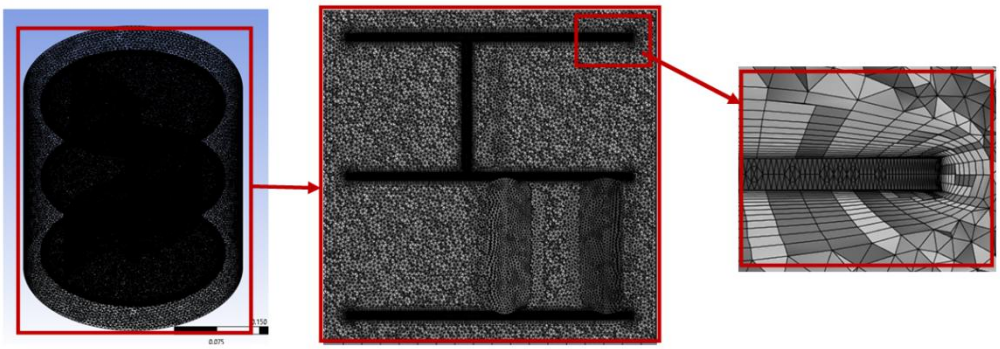

Figure 4. Mesh distribution in the rotating zone

The unsteady Reynolds-Averaged Navier–Stokes (URANS) equations were employed to capture the transient characteristics of the flow, particularly the interaction between the rotating blades and the surrounding fluid. To model turbulence effects, the k–ω Shear Stress Transport (SST) turbulence model was adopted. Previous comparative studies reported by Jin et al. [21] demonstrated that the SST k–ω model provides better agreement with experimental data compared to the realizable k–ε model, especially in predicting complex vortex structures and pressure distributions. Therefore, the SST k–ω model was selected for this study.

A rotating sub-domain was defined for the turbine blades, where the cell zone motion was prescribed according to varying TSR values ranging from 0.4 to 1.0. This range was selected to investigate the aerodynamic performance of the turbine under low to moderate operating conditions.

The boundary conditions included a velocity inlet with wind speeds of 3 m/s and 5 m/s and a turbulence intensity of 5 percent. The outlet boundary was defined with a gauge pressure of 0 Pa. The interfaces between the rotating and stationary regions were defined to ensure smooth data exchange between domains. The blade surfaces were treated as no-slip walls, implying zero relative velocity between the fluid and the blade surface.

To accurately capture the unsteady rotational motion of the turbine, the sliding mesh technique was employed. The pressure–velocity coupling was solved using the SIMPLE algorithm. Spatial gradients were computed using the least-squares cell-based method, while pressure and momentum equations were discretized using a second-order upwind scheme to improve numerical accuracy and solution stability.

RESULT AND DISCUSSION

The performance curves of the two-stage Savonius turbine at wind velocities of 3 m/s and 5 m/s are presented in Figure 5. The variations of the power coefficient (Cp) and torque coefficient (Ct) with respect to the tip speed ratio (TSR) illustrate the aerodynamic behavior of the turbine under different flow conditions.

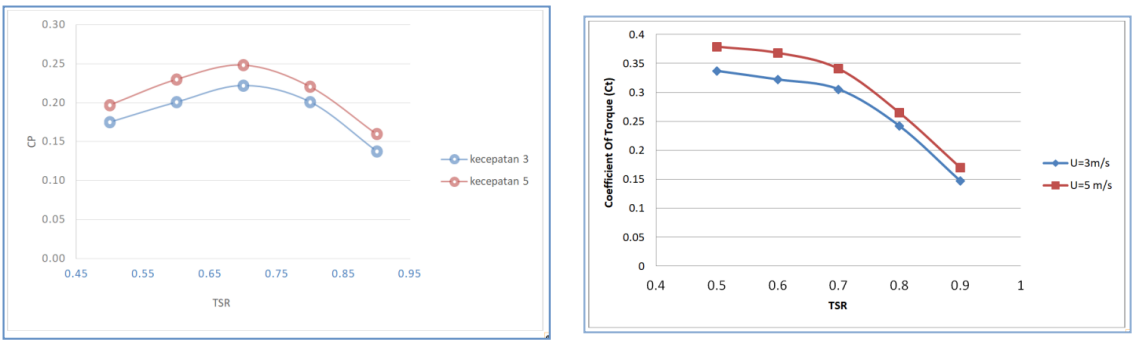

(a) (b)

Figure 5. Performance of the POCREN Savonius wind turbine: (a) Cp–TSR and (b) Ct–TSR

The Cp–TSR curves exhibit a characteristic trend typical of drag-type vertical-axis wind turbines. At both wind velocities, the Cp increases with increasing TSR until reaching an optimum value, after which it decreases due to increased aerodynamic losses and a reduction in pressure differential across the blades.

The maximum Cp is observed at a TSR in the range of approximately 0.7 to 0.75, which corresponds to the most efficient operating condition of the turbine. At a wind speed of 3 m/s, the peak Cp reaches approximately 0.22, while at 5 m/s, the Cp increases to about 0.26. This result indicates that the turbine achieves higher efficiency at increased wind velocity. The improved performance at higher wind speed can be attributed to better flow attachment on the advancing blade and stronger pressure gradients between the concave and convex blade surfaces. Umesh K. Patel et al. [22] reported a maximum Cp of 0.22 at a TSR of 0.8 for a two-stage Savonius turbine. In the present study, a comparable Cp value of approximately 0.25 was achieved, which is likely influenced by differences in blade geometry, although the rotor design is still based on a circular arc profile.

The Ct–TSR curves show a decreasing trend with increasing TSR. At lower TSR values of approximately 0.5, the turbine produces the highest torque coefficient, reaching around 0.37 at 5 m/s and 0.33 at 3 m/s. This behavior is consistent with the operating principle of Savonius turbines, where torque generation is dominated by drag forces resulting from pressure differences between the blade surfaces. As the rotational speed increases, the relative velocity between the returning blade and the incoming flow becomes larger, reducing the effective pressure differential and consequently lowering the generated torque.

The results confirm that the two-stage configuration improves torque continuity throughout a full rotation cycle, resulting in smoother power output compared to a single-stage rotor. The higher performance observed at a wind speed of 5 m/s indicates that the turbine operates more efficiently under moderate wind conditions, which are commonly found in low-wind or urban environments. However, beyond the optimal TSR range, both Cp and Ct decrease sharply, suggesting that excessive rotational speed leads to increased flow separation and vortex shedding near the overlap region. These findings are consistent with previous studies, which reported that two-stage Savonius turbines exhibit superior efficiency compared to single-stage configurations [17]–[20].

Pressure Contour Analysis

In the numerical simulation, pressure contours on the Savonius turbine blades were analyzed at several angular positions. Figure 6 shows the pressure distribution on the two-stage Savonius turbine, which is a component of the POCREN system. The presented pressure contour corresponds to a TSR of 0.7 at a wind velocity of 3 m/s.

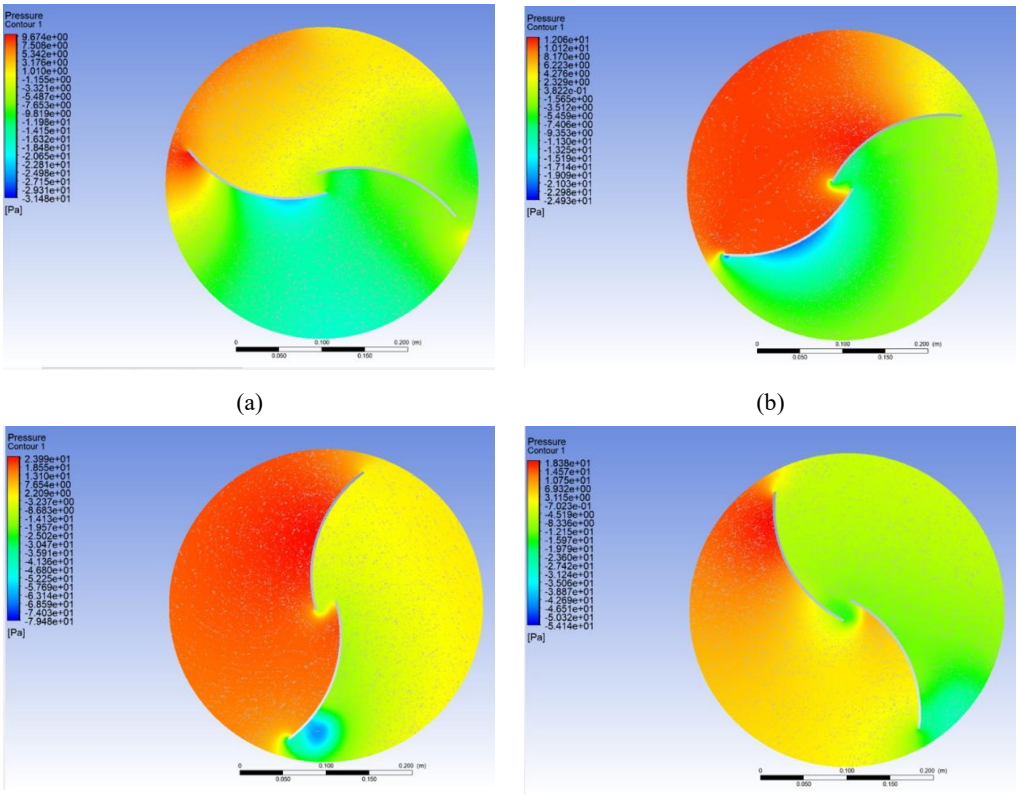

Figure 6. Pressure contour of the two-stage Savonius turbine

The contour plots reveal a clear pressure difference between the concave and convex surfaces of the blades, which is responsible for torque generation and rotor rotation. High-pressure regions are observed on the windward side of the advancing blade, while low-pressure regions appear on the leeward side. This pressure imbalance produces a net driving moment on the turbine shaft.

The pressure gradient is most pronounced near the blade overlap and tip regions, where flow separation and vortex formation occur. These flow phenomena enhance aerodynamic interaction between the turbine stages and contribute to torque generation. At an angular position of 30 degrees, the pressure contour shows that the concave surface of the advancing blade experiences high pressure of approximately +120 Pa due to direct flow impingement and deceleration. In contrast, the convex surface exhibits low-pressure regions with values reaching approximately −240 Pa, resulting from flow acceleration and partial separation along the curved blade profile. This pressure distribution produces a pressure difference of approximately 360 Pa across the blade surfaces, generating a dominant drag force that drives rotor rotation.

At certain angular positions, the downstream blade experiences partial shielding from the upstream blade, which promotes pressure recovery and reduces drag on the returning blade. This interaction highlights the effectiveness of the two-stage configuration in maintaining torque continuity throughout a complete rotational cycle. Overall, the pressure contour analysis confirms that the aerodynamic performance of the two-stage Savonius turbine is primarily governed by pressure asymmetry induced by blade geometry and flow interaction.

CONCLUSIONS

The results of the numerical simulation and performance evaluation clearly demonstrate the aerodynamic behavior of the two-stage Savonius turbine. Pressure contour analysis reveals a distinct asymmetry in pressure distribution between the concave and convex blade surfaces, which serves as the primary mechanism for torque generation. High-pressure regions are concentrated on the windward side of the advancing blade, while low-pressure zones develop on the leeward side of the returning blade. The strongest pressure gradients are observed near the overlap and blade tip regions, where flow separation and vortex shedding occur. These flow phenomena enhance aerodynamic interaction between the two stages, improving torque continuity and reducing rotational fluctuations over a complete cycle.

The performance curves indicate that both the torque coefficient (Ct) and power coefficient (Cp) are strongly influenced by the tip speed ratio (TSR). The turbine achieves optimum performance at a TSR in the range of 0.7 to 0.75, with a maximum Cp of approximately 0.22 at a wind velocity of 3 m/s and 0.26 at 5 m/s. This result confirms that the turbine operates more efficiently under moderate wind conditions, as increased wind velocity strengthens the pressure differential and stabilizes the flow around the rotor. Meanwhile, the Ct value decreases gradually with increasing TSR, which is consistent with the operating characteristics of drag-based vertical-axis wind turbines, where higher rotational speeds reduce the effective pressure difference across the blades and consequently lower the generated torque.

ACKNOWLEDGEMENT

This work was supported by the PKM-KC Research Grant from the Ministry of Education and Culture of the Republic of Indonesia under Grant No. 068/E2/PPK/SPPK/PKM/2025. The authors also gratefully acknowledge the facility support provided by Politeknik Negeri Padang, West Sumatra, Indonesia, during the research activities. This article serves as an additional output of the PKM-KC program, also known as the Student Creativity Program in the Scientific Creation category.

REFERENCES

[1] E. S. Hamid and B. S. Wibowo, "The impact of CO2 emission on health expenditure: lesson learned from ASEAN five countries," *IOP Conf. Ser. Earth Environ. Sci.*, vol. 1180, no. 1, p. 12044, 2023, doi: https://doi.org/10.1088/1755-1315/1180/1/012044.

[2] R. Sumiati, U. G. S. Dinata, and D. A. Saputra, "Enhancing savonius rotor performance with wavy pattren in the concave surface - A short review," *AIP Conf. Proc.*, vol. 3223, no. 1, p. 30013, Jan. 2025, doi: https://doi.org/10.1063/5.0243088.

[3] K. A. H. Al-Gburi, F. B. I. Alnaimi, B. A. Al-quraishi, E. Sann Tan, and M. M. Maseer, "A comparative study review: The performance of Savonius-type rotors," *Mater. Today Proc.*, vol. 57, pp. 343–349, 2022, doi: https://doi.org/10.1016/j.matpr.2021.09.226.

[4] A. Jebelli, N. Lotfi, M. Saeid Zare, and M. C. E. Yagoub, "A comprehensive review of effective parameters to improve the performance of the Savonius turbine using a computational model and comparison with practical results," *Water-Energy Nexus*, vol. 7, pp. 266–274, Dec. 2024, doi: https://doi.org/10.1016/j.wen.2024.11.002.

[5] M. Al-Ghriybah, M. F. Zulkafli, D. H. Didane, and S. Mohd, "Review of the Recent Power Augmentation Techniques for the Savonius Wind Turbines," *J. Adv. Res. Fluid Mech. Therm. Sci.*, vol. 60, no. 1, pp. 71–84, Mar. 2024.

[6] P. M. Kumar, K. Sivalingam, S. Narasimalu, T.-C. Lim, S. Ramakrishna, and H. Wei, "A Review on the Evolution of Darrieus Vertical Axis Wind Turbine: Small Wind Turbines," *J. Power Energy Eng.*, vol. 7, no. 4, pp. 27–44, 2019, doi: https://doi.org/10.4236/jpee.2019.74002.

[7] J. V. Akwa, H. A. Vielmo, and A. P. Petry, "A review on the performance of Savonius wind turbines," *Renew. Sustain. Energy Rev.*, vol. 16, no. 5, pp. 3054–3064, 2012, doi: https://doi.org/10.1016/j.rser.2012.02.056.

[8] L. Chen, J. Chen, and Z. Zhang, "Review of the Savonius rotor's blade profile and its performance," *J. Renew. Sustain. Energy*, vol. 10, no. 1, p. 13306, Jan. 2018, doi: https://doi.org/10.1063/1.5012024.

[9] R. Sumiati, "Pengujian turbin angin savonius tipe U tiga sudu di lokasi Pantai Air Tawar Padang," *J. Tek. Mesin*, vol. 9, no. 1, pp. 26–32, 2012.

[10] N. Alom and U. K. Saha, "Evolution and Progress in the Development of Savonius Wind Turbine Rotor Blade Profiles and Shapes," *J. Sol. Energy Eng.*, vol. 141, no. 3, p. 030801, Nov. 2018, doi: https://doi.org/10.1115/1.4041848.

[11] P. A. Setiawan, T. Yuwono, and W. A. Widodo, "Effect of a circular cylinder in front of advancing blade on the Savonius water turbine by using transient simulation," *Int. J. Mech. Mechatronics Eng.*, vol. 19, no. 1, pp. 151–159, 2019.

[12] W. Yahya, K. Ziming, W. Juan, M. S. Qurashi, M. Al-Nehari, and E. Salim, "Influence of tilt angle and the number of guide vane blades towards the Savonius rotor performance," *Energy Reports*, vol. 7, pp. 3317–3327, 2021, doi: https://doi.org/10.1016/j.egyr.2021.05.053.

[13] C. R. Sonawane, Y. Sasar, M. Shaikh, Y. Kokande, M. Mustafa, and A. Pandey, "Numerical simulation of Savonius rotors used for low wind speed application," *Mater. Today Proc.*, vol. 49, pp. 1610–1616, 2022, doi: https://doi.org/10.1016/j.matpr.2021.07.420.

[14] N. Alom and U. K. Saha, "Examining the Aerodynamic Drag and Lift Characteristics of a Newly Developed Elliptical-Bladed Savonius Rotor," *J. Energy Resour. Technol.*, vol. 141, no. 5, p. 051201, Jan. 2019, doi: https://doi.org/10.1115/1.4041735.

[15] M. Al-Ghriybah, M. F. Zulkafli, D. H. Didane, and S. Mohd, "Performance of the Savonius Wind Rotor with Two Inner Blades at Low Tip Speed Ratio," *CFD Lett.*, vol. 12, no. 3, pp. 11–21, 2020, doi: https://doi.org/10.37934/cfdl.12.3.1121.

[16] R. Sumiati, U. G. S. Dinata, D. A. Saputra, and Y. D. Herlambang, "Enhancing Savonius Rotor Performance with Zigzag in Concave Surface-CFD Investigation," *CFD Lett.*, vol. 17, no. 5, pp. 101–114, 2025, doi: https://doi.org/10.37934/cfdl.17.2.100114.

[17] Y. S. Indartono, I. Farozan, and G. T. Fauzanullah, "Experimental Study into The Effect of Multi-staging and Check Valve Addition on The Performance of Savonius Wind Rotors with Modified-Bach Blade," *Int. J. Technol.*, vol. 16, no. 2, pp. 291–319, 2025, doi: https://doi.org/10.14716/ijtech.v16i2.6389.

[18] A. Kumar, R. P. Saini, G. Saini, and G. Dwivedi, "Effect of number of stages on the performance characteristics of modified Savonius hydrokinetic turbine," *Ocean Eng.*, vol. 217, p. 108090, 2020, doi: https://doi.org/10.1016/j.oceaneng.2020.108090.

[19] M. S. M. Halmy, D. H. Didane, L. O. Afolabi, and S. Al-Alimi, "Computational Fluid Dynamics (CFD) Study on the Effect of the Number of Blades on the Performance of Double-Stage Savonius Rotor," *CFD Lett.*, vol. 13, no. 4, pp. 1–10, Apr. 2021, doi: https://doi.org/10.37934/cfdl.13.4.110.

[20] M. Zemamou, A. Toumi, K. Mrigua, and M. Aggour, "Modified Design of Savonius Wind Turbine Blade for Performance Improvement," *Int. J. Innov. Technol. Explor. Eng.*, vol. 9, no. 1, pp. 1432–1437, 2019, doi: http://doi.org/10.35940/ijitee.A4202.119119.

[21] X. Jin, Y. Wang, W. Ju, J. He, and S. Xie, "Investigation into parameter influence of upstream deflector on vertical axis wind turbines output power via three-dimensional CFD simulation," *Renew. Energy*, vol. 115, pp. 41–53, 2018, doi: https://doi.org/10.1016/j.renene.2017.08.012.

[22] U. K. Patel, N. Alom, and U. K. Saha, "Aerodynamic analysis of a 2-stage elliptical-bladed Savonius wind rotor: Numerical simulation and experimental validation," *Int. J. Green Energy*, vol. 21, no. 1, pp. 102–115, Jan. 2024, doi: https://doi.org/10.1080/15435075.2023.2194975.

PISTON
Journal of Technical Engineering:

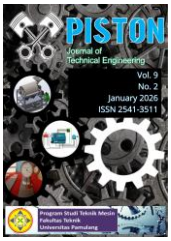

Development of Regulatory Recommendations for City Bus Bumper Bars through Design and Analysis Based on Standard 67 Pa. Code § 171.44

Leonardo Paksi Sukoco[1,a)], Mochammad Avrieza Havies Aravy[2], Nurrahim Hasan Al Banna[2], Feby Ayu Winesti[2]

[1]*Land Transportation Management Center (BPTD) Class III Bengkulu, Indonesia*
[2]*Automotive Engineering Technology, Polytechnic of Road Transportation Safety, Tegal, Indonesia*

E-mail: [a)] leonardopaksi@gmail.com

Received: December 30, 2025 *Revision: January 13, 2026* *Accepted: January 15, 2026*

Abstract: Indonesia currently does not have specific technical regulations governing the design of urban bus bumper bars, unlike passenger vehicles, which are regulated by national and international standards. Data from the Indonesian National Police Traffic Corps in 2022 recorded 3,847 bus-related accidents resulting in 587 fatalities, with 42 percent occurring in urban areas at speeds ranging from 30 to 50 km/h. This study aims to develop regulatory recommendations for urban bus bumper bars by adapting the standard 67 Pa. Code §171.44 to Indonesian operational conditions. The research methodology includes field observations of 10 Trans Jogja buses, bumper bar design using a combination of 6061-T6 aluminum alloy and elastomer materials, and structural performance analysis through impact simulations based on the Explicit Dynamics finite element method using ANSYS software. The simulation results show that the proposed bumper bar design satisfies safety requirements, with maximum stress values of 260 MPa at 30 km/h and 293 MPa at 50 km/h. Although the stress at 50 km/h exceeds the material yield strength of 280 MPa, the response indicates localized plastic deformation without global structural failure. Controlled deformation of 163.04 mm at 30 km/h and 275.78 mm at 50 km/h, following a localized progressive deformation pattern without excessive intrusion, along with an energy absorption capacity of at least 5 kJ, demonstrates effective passenger protection. The resulting regulatory recommendations include dimensional specifications (height 400–600 mm, width ≥2000 mm), material requirements (yield strength ≥250 MPa), and performance criteria to support the revision of Minister of Transportation Regulation No. 33 of 2018.

Keywords: Bumper Bar Regulations, Urban Bus Safety, Passive Vehicle Safety, Impact Performance Criteria, ANSYS Explicit Dynamics.

Abstrak: *Indonesia saat ini belum memiliki regulasi teknis spesifik yang mengatur perancangan bumper bar bus perkotaan, berbeda dengan kendaraan penumpang yang telah diatur melalui standar nasional maupun internasional. Data Korps Lalu Lintas Kepolisian Republik Indonesia tahun 2022 mencatat 3.847 kecelakaan yang melibatkan bus dengan 587 korban meninggal dunia, di mana 42 persen kejadian terjadi di kawasan perkotaan pada rentang kecepatan 30 hingga 50 km/jam. Penelitian ini bertujuan untuk mengembangkan rekomendasi regulasi bumper bar bus perkotaan melalui adaptasi standar 67 Pa. Code §171.44 yang disesuaikan dengan kondisi operasional di Indonesia. Metodologi penelitian meliputi observasi lapangan terhadap 10 unit bus Trans Jogja, perancangan bumper bar menggunakan kombinasi material aluminium alloy 6061-T6 dan elastomer, serta analisis kinerja struktural melalui simulasi impak berbasis metode elemen hingga Explicit Dynamics dengan bantuan perangkat lunak ANSYS. Hasil simulasi menunjukkan bahwa desain bumper bar yang diusulkan memenuhi kriteria keselamatan, dengan tegangan maksimum sebesar 260 MPa pada kecepatan 30 km/jam dan 293 MPa pada 50 km/jam. Meskipun tegangan pada kecepatan 50 km/jam melebihi batas kekuatan luluh material sebesar 280 MPa, respons struktur menunjukkan terjadinya deformasi plastis lokal tanpa menyebabkan kegagalan struktural global. Deformasi terkendali sebesar 163,04 mm pada 30 km/jam dan 275,78 mm pada 50 km/jam dengan pola deformasi progresif terlokalisasi tanpa intrusi berlebihan, serta kapasitas absorpsi energi minimal 5 kJ, mengindikasikan kemampuan perlindungan penumpang yang efektif. Rekomendasi regulasi yang dihasilkan mencakup spesifikasi dimensi (tinggi 400–600 mm, lebar ≥2000 mm), persyaratan material (kekuatan luluh ≥250 MPa), serta kriteria kinerja untuk mendukung revisi Peraturan Menteri Perhubungan Nomor 33 Tahun 2018.*

Kata kunci: *Regulasi Bumper Bar, Keselamatan Bus Perkotaan, Keselamatan Kendaraan Pasif, Metode Elemen Hingga, ANSYS Explicit Dynamics.*

INTRODUCTION

Passive vehicle safety is a top priority in public transportation design to protect road users from the risk of fatal injuries [1]. Bumper bars on city buses serve to absorb impact energy and distribute the load to minimize structural damage and passenger injury [2]–[5]. City buses operate in dense corridors with intensive interaction with light vehicles, pedestrians, and road infrastructure [6]. The design of urban bus bumper bars in Indonesia is generally not based on systematic crashworthiness analysis without crash performance validation [7]. This study develops regulatory recommendations for urban bus bumper bars through design and analysis based on the 67 Pa. Code §171.44 standard, adapted to Indonesian operating conditions using Explicit Dynamics Finite Element Analysis.

Data from the Indonesian National Police Traffic Corps in 2022 recorded 3,847 accidents involving buses with 587 fatalities, of which 42% occurred in urban areas at speeds of 30–50 km/h [8]. The geometric mismatch between bus bumpers and light vehicles increases the risk of injury by up to 2.5 times [9]. A collision between a TransJakarta bus and a motorcycle in 2021 showed that inadequate bumper design contributed to fatal injuries [10]. Indonesian city buses carry approximately 2.3 million trips daily [11], with a potential economic loss of IDR 1.2 trillion annually [12], highlighting the urgency of implementing crashworthiness-based bumper bar standards.

Motor vehicle safety regulations in Indonesia refer to Minister of Transportation Regulation No. 33 of 2018, which adopts parts of the UNECE (United Nations Economic Commission for Europe) Regulations [13]. UNECE R42 regulates bumpers for M1 category vehicles, while UNECE R93 regulates front underrun protection devices for N2 and N3 trucks. However, there are no specific regulations governing bumper bars for M3 category urban buses with a gross vehicle weight of less than 12 ton [14]. Pennsylvania Code 67 §171.44 specifies standards for school bus bumpers, including a height of 406–610 mm, strength of 22.24 kN, and yield strength of 248 MPa [15]. A survey of 15 national bus manufacturers revealed variations in bumper height ranging from 300 to 800 mm without technical justification [16], forming the basis for adapting the 67 Pa. Code §171.44 standard to the Indonesian context.

This study adapts the 67 Pa. Code §171.44 standard through three stages: (1) field observations of 10 Trans Jogja bus units to measure existing bumper dimensions [17]; (2) redesign of the bumper bar using a combination of aluminum alloy, elastomer, and structural steel materials for collision scenarios at 30 km/h and 50 km/h; and (3) numerical impact analysis using ANSYS Explicit Dynamics with the AUTODYN solver [18].

The Finite Element Method has been proven effective for crashworthiness evaluation, offering high accuracy and cost efficiency, with costs up to 80% lower than physical testing [4], [5], [19], [20]. Aluminum alloy was selected due to its high strength-to-weight ratio and good energy absorption capability [20], [21]. Material modeling employed the Johnson–Cook plasticity model for aluminum alloy with a yield stress of 250 MPa and the Ogden hyperelastic model for the elastomer with μ_1 = 700 kPa. The mesh used 20 mm tetrahedral elements with a total of 84,987 elements, and energy balance validation showed an error of less than 10%.

Existing research on bumper crashworthiness reveals gaps in applications for urban buses. Most studies focus on passenger vehicles or material and geometric variations without considering the structural characteristics of buses and their interaction with vulnerable road users [4], [22]. Acar and Güler [2] optimized intercity coach bumpers without examining urban operating speeds. Güler et al. [14] analyzed bus crashworthiness based on UNECE R29 without addressing frontal bumper impacts. Ramadhan et al. [18] evaluated bumper materials limited to passenger vehicles at a single impact speed of 40 km/h. Identified research gaps include: (1) the absence of studies evaluating urban bus bumper bar performance at multiple impact velocities of 30 km/h and 50 km/h; (2) the lack of parametric analysis of geometric design and material properties; and (3) the absence of a specific technical regulatory framework adapting the 67 Pa. Code §171.44 standard to Indonesian conditions.

This research contributes to crashworthiness methodology by achieving an accuracy of approximately 95% while reducing costs by up to 80% compared to physical testing [1]. The policy contribution includes draft regulatory recommendations covering dimensional requirements (height 400–600 mm, width ≥2000 mm), material specifications (yield strength ≥250 MPa), performance criteria (deformation ≤150 mm at 30 km/h and energy absorption ≥5 kJ), and testing protocols to support the revision of Minister of Transportation Regulation No. 33 of 2018. Implementation of these recommendations is projected to reduce injury severity by 30–40% and decrease economic losses by IDR 360–480 billion annually [9], [12]. This research supports the National Road Safety Plan 2021–2040, which targets a 50% reduction in accident fatalities by 2030 and aligns with Sustainable Development Goal target 3.6 [13]. It also aims to enhance the competitiveness of the national car body industry through harmonization with international standards [11]. Therefore, this study seeks to develop technical regulatory recommendations for urban bus bumper bars in Indonesia through a crashworthiness-based design and evaluation approach.

The research is conducted by adapting the requirements of the 67 Pa. Code §171.44 standard to Indonesian operational conditions. The methodology includes field observations of existing urban buses, geometric redesign of the bumper bar using a combination of aluminum alloy and elastomer materials, and numerical impact simulations at 30 km/h and 50 km/h using the Explicit Dynamics Finite Element Method in ANSYS. The outcomes of this study are expected to provide validated performance criteria, dimensional specifications, and material requirements that can support the revision of national regulations, particularly Minister of Transportation Regulation No. 33 of 2018, and enhance passive safety performance for urban buses.

METHODS

This research began with the identification of problems and a literature study related to the safety of urban bus bumper bars. Next, field observations and data collection were conducted to obtain existing conditions. The data were analyzed through gap analysis as the basis for bumper bar design and simulation. The simulation results were used for the design iteration process as well as performance validation and verification, which were then formulated into recommendations for urban bus bumper bar regulations.

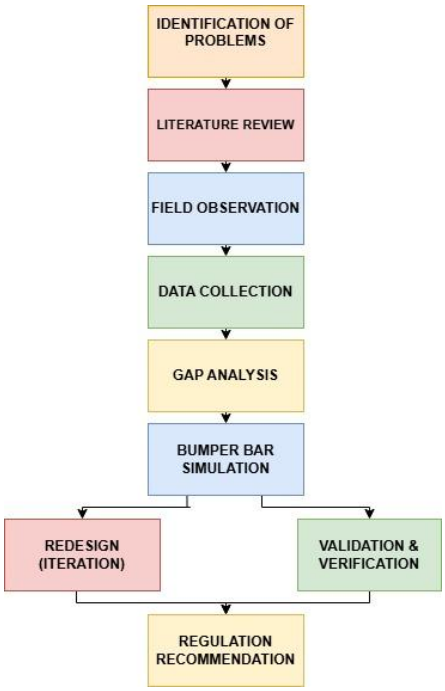

Figure 1. Research Flow Chart

The overall research methodology is illustrated in Figure 1, showing the sequence of research activities from problem identification to regulation recommendation.

Research Tools and Materials

Field observations were conducted on 10 Trans Jogja buses using digital calipers (±0.01 mm), laser meters (±2 mm), and digital cameras to document the geometry of existing bumpers [14]. Operational and accident data were obtained from PT Anindya Mitra Internasional and the Yogyakarta Transportation Agency [5].

Numerical simulations were performed using ANSYS Workbench 2024 R2 with the AUTODYN solver and SolidWorks 2022 for three-dimensional modeling of the bumper bar and the chassis of the Hino FB130 bus [15]. The three-dimensional bumper bar geometry generated in ANSYS and the overall bus configuration used as the simulation reference are illustrated in Figure 2 (a) and Figure 2 (b), respectively. The simulation model consisted of eight bodies with a total mass of 307.16 kg, including a bumper frame assembly made of aluminum alloy 6061-T6 with a density of 2770 kg/m³ and a yield strength of 280 MPa using the Johnson–Cook plasticity model; an elastomer energy absorber modeled using the Ogden hyperelastic model with μ_1 = 700 kPa and a density of 1150 kg/m³; a structural steel mounting bracket with a yield strength of 250 MPa and a density of 7850 kg/m³; and a rigid impactor with a mass of 235.11 kg [2], [15]. Two impactor velocity scenarios were applied, namely 30 km/h and 50 km/h, based on accident statistics [5].

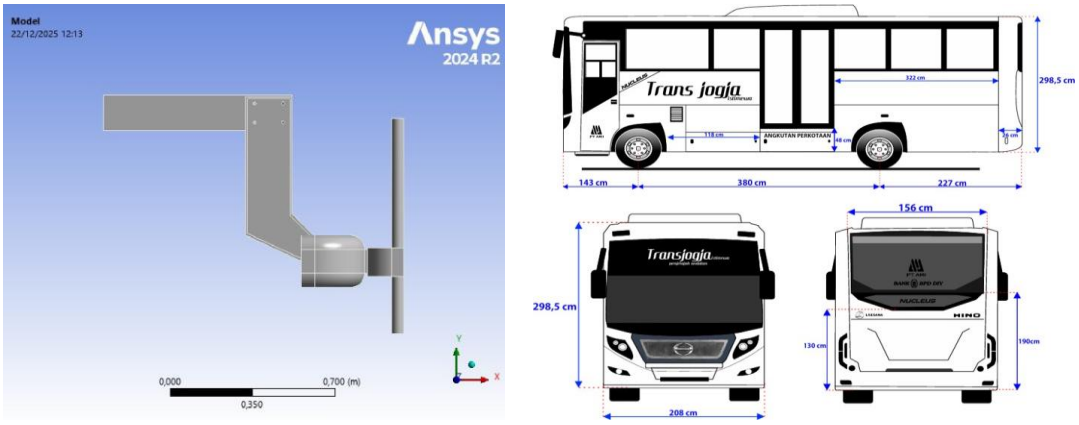

(a) (b)

Figure 2. (a) Bumper bar geometric design and (b) blueprint of the Hino Trans Jogja bus

The mechanical and physical properties of the simulation materials are presented in Table 1.

Table 1. Mechanical and physical properties of materials

Material Name	Density (kg/m^3)	Young's Modulus (MPa)	Poisson's Ratio (v)
Aluminum Alloy 6061-T6	2700	71	0.33
Structural Steel (ASTM A36 or equivalent)	7850	210	0.30
Elastomer (Ogden hyperelastic model, EPDM rubber)	1150	–	–

The mechanical and physical properties of the materials used in the impact simulation are summarized in Table 1. The materials consisted of aluminum alloy 6061-T6 as the primary bumper structure, structural steel ASTM A36 as the rigid impactor, and an elastomer based on the Ogden hyperelastic model, represented by EPDM rubber, as the energy-absorbing element. As presented in Table 1, aluminum alloy 6061-T6 has a density of 2700 kg/m^3, a Young's modulus of 71 MPa, and a Poisson's ratio of 0.33, making it suitable for lightweight structural applications. Structural steel (ASTM A36 or equivalent), with a density of 7850 kg/m^3, a Young's modulus of 210 MPa, and a Poisson's ratio of 0.30, was employed to represent a rigid impactor condition. The elastomer material, modeled using the Ogden hyperelastic formulation and represented by EPDM rubber, has a density of 1150 kg/m^3, while its elastic constants are defined through the hyperelastic model rather than linear elastic parameters, as indicated by the absence of Young's modulus and Poisson's ratio values in Table 1.

Aluminum alloy 6061-T6 was selected due to its favorable strength-to-weight ratio and its widespread use in vehicle structural applications. This material selection is consistent with comparative studies of aluminum, steel, and composite bumper materials, which indicate that aluminum exhibits more stable energy absorption characteristics at medium impact velocities compared to overly rigid or brittle materials [4].

The elastomer material was modeled using the Ogden hyperelastic formulation to represent the nonlinear behavior of rubber during impact, which functions to dissipate energy and reduce peak reaction forces transmitted to the bus frame. Structural steel was used for the impactor due to its high stiffness and strength, allowing it to realistically represent impact conditions. Elastomeric materials were employed to model the nonlinear response of energy-absorbing components during collision events.

Observation and Analysis

Measurements of existing bumper bars indicated heights ranging from 300 to 800 mm, with an average of 520 mm, widths between 1800 and 2400 mm, and horizontal projections of 80 to 150 mm [13], [14]. The dimensional characteristics and geometric configuration of the bumper bar considered in this study, which are consistent with these measured ranges, are illustrated in Figure 3 (a). The adaptation baseline from 67 Pa. Code §171.44 specifies a bumper height of 406 to 610 mm and a minimum strength of 22.24 kN [12]. The impactor geometry and configuration adopted in the simulation, following the requirements of UNECE R42, are shown in Figure 3 (b). Currently, Indonesia does not have specific regulations governing bumper bars for M3 category buses with a gross vehicle weight of less than 12 tons [10], [11].

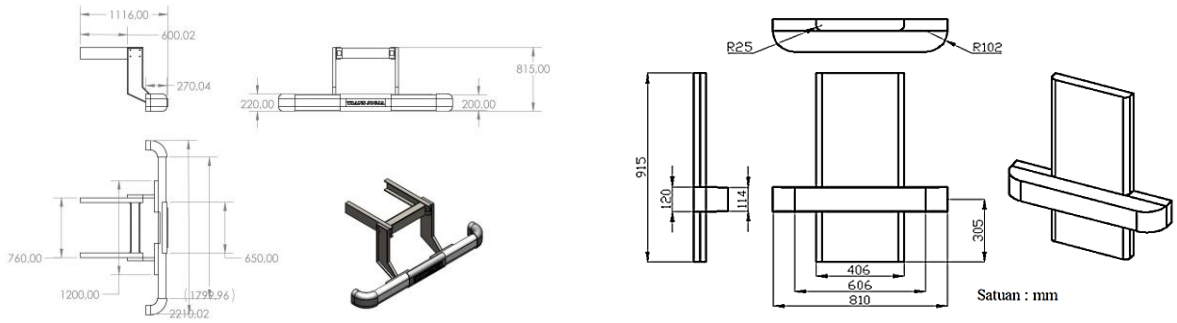

(a) (b)

Figure 3. (a) Bumper bar dimensions and (b) impactor configuration in accordance with UNECE R42 [21]

A survey of 15 bus body manufacturers revealed the use of aluminum alloy materials without crashworthiness-based analysis [4], [13]. Traffic accident data from the Indonesian National Police Traffic Corps in 2022 recorded 3,847 bus-related accidents with 587 fatalities, of which 42% occurred at speeds ranging from 30 to 50 km/h [5], [6]. Based on these findings, the design requirements were established as follows: bumper height of 400 to 600 mm, material yield strength of at least 250 MPa, maximum deformation of 150 mm at 30 km/h, and minimum energy absorption of 5 kJ [2], [12]. The criteria for maximum deformation and allowable stress follow established structural evaluation standards to ensure elastic behavior and prevent plastic failure [17], [18].

The simulation setup employed a linear tetrahedral mesh with an element size of 20 mm, resulting in a total of 84,987 elements and 26,061 nodes. This mesh configuration was selected to balance numerical accuracy and computational efficiency, as recommended in previous impact simulation studies [1], [15], [17]. The distribution of the tetrahedral mesh applied to the bumper bar and the impactor is illustrated in Figure 4 (a). Tetrahedral mesh configurations have been shown to be effective for analyzing complex structures with non-uniform geometry, such as bumper bars [17], [18]. The simulations were conducted using an automatic time step with a safety factor of 0.9 and a maximum cycle count of 100,000, with a total simulation time of 20 ms, which is commonly adopted in explicit dynamic collision analyses to maintain numerical stability [15], [17]. The boundary condition in the form of fixed support applied to the bumper bar, as implemented in the simulation model, is shown in Figure 4 (b).

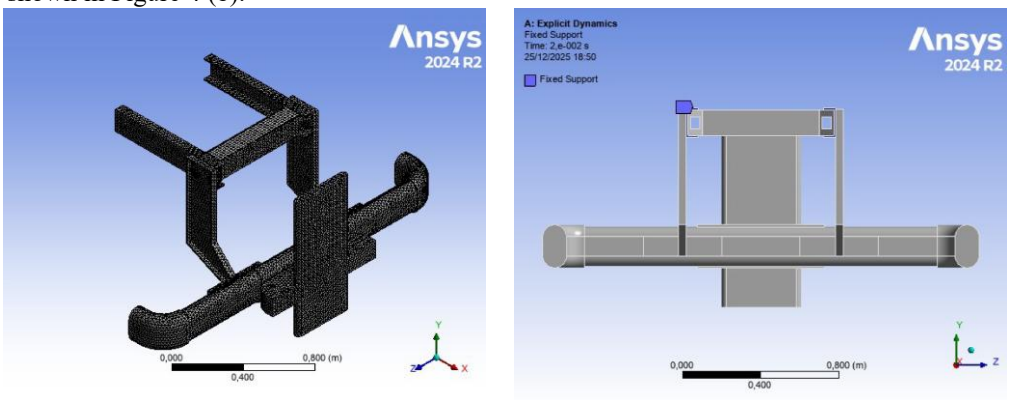

(a) (b)

Figure 4. (a) Mesh distribution on the bumper bar and impactor and (b) application of fixed support on the bumper bar

Contact interactions between the bumper bar and the impactor were modeled using frictional contact with a friction coefficient of 0.3, while internal contacts between components were defined as bonded contacts to represent rigid structural connections [11]. Boundary conditions in the form of fixed supports were applied to both sides of the chassis frame to represent vehicle restraint conditions during impact events [2], [12].

RESULT AND DISCUSSION

Stress Analysis (Equivalent Stress)

The simulation results show that the equivalent stress (von Mises stress) is concentrated in the initial contact area between the impactor and the bumper bar structure, particularly at the center of the bumper cross-section and at the connection area with the frame bracket. This stress distribution pattern indicates that the load transfer mechanism occurs progressively from the impact point to the main support structure, as illustrated in the

equivalent stress contours obtained from the ANSYS Explicit Dynamics simulation. The equivalent stress contours corresponding to impact velocities of 30 km/h and 50 km/h, which clearly show the locations and intensity of stress concentration described above, are presented in Figure 5 (a) and Figure 5 (b), respectively.

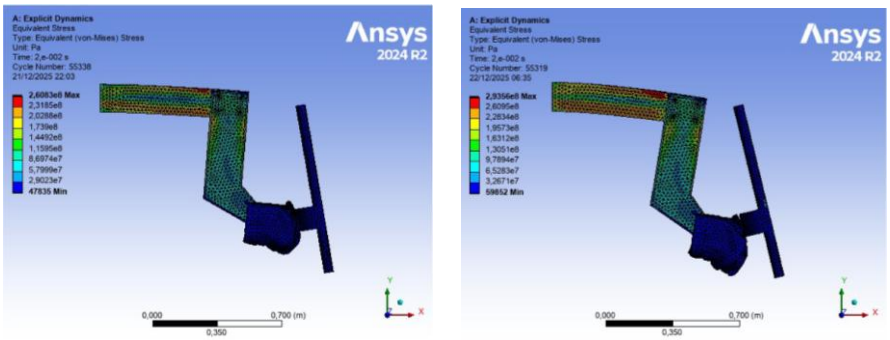

(a) (b)

Figure 5. (a) Equivalent stress at 30 km/h and (b) equivalent stress at 50 km/h

The maximum equivalent stress observed in the 30 km/h impact simulation was approximately 260 MPa, while in the 50 km/h impact simulation it reached around 293 MPa. At an impact speed of 30 km/h, the stress level remained below the yield strength of the bumper bar material, indicating that the structure did not experience significant plastic deformation. In contrast, at an impact speed of 50 km/h, the equivalent stress exceeded the material yield strength, which indicates the occurrence of localized plastic deformation. However, no global structural collapse or catastrophic failure was observed, demonstrating that the bumper bar maintained its overall structural integrity despite entering a localized plastic deformation regime.

This behavior is consistent with the findings of Acar and Güler [2], who reported that concentrated but controlled stress distributions are indicative of effective bumper designs capable of absorbing impact energy without inducing critical structural damage. Furthermore, a relatively uniform stress distribution suggests that the geometric configuration of the bumper, particularly in the web and flange regions, plays an important role in reducing local stress concentrations. These findings are also in agreement with the work of Ramadhan et al. [4], who reported that increasing the effective cross-sectional area can reduce maximum stress levels by approximately 20–30% under medium-impact conditions.

Compared to existing bumper designs, which are generally implemented without numerical stress analysis, the proposed bumper bar design demonstrates improved structural performance. Therefore, these results emphasize the importance of applying numerical simulation-based approaches in the development of urban bus bumper bar regulations in Indonesia, in accordance with recommendations from UNECE and Pennsylvania Code §171.44 [12].

Deformation Analysis

The total deformation simulation results show that the maximum deformation occurs in the central region of the bumper bar, specifically at the point of contact with the impactor, as illustrated in the total deformation contours. The deformation pattern is progressive and localized, without significant propagation to the main frame structure of the bus. The distribution and magnitude of total deformation under impact velocities of 30 km/h and 50 km/h, which highlight the localized deformation behavior described above, are shown in Figure 6 (a) and Figure 6 (b), respectively.

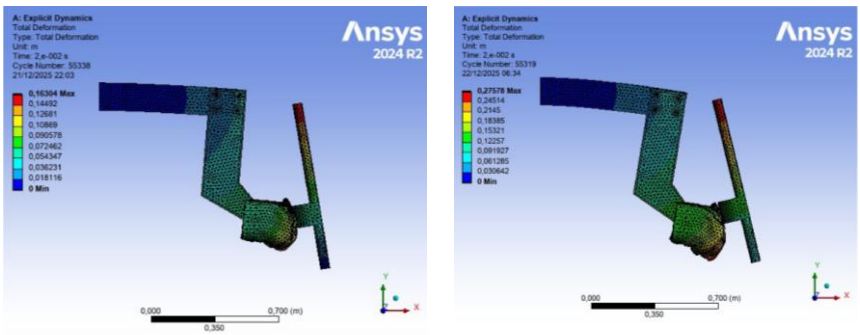

(a) (b)

Figure 6. (a) Deformation at 30 km/h, (b) deformation at 50 km/h

The maximum deformation observed in the 30 km/h impact simulation reached 163.04 mm, while in the 50 km/h impact simulation it reached 275.78 mm. At an impact speed of 30 km/h, deformation was primarily localized at the contact region between the bumper bar and the impactor, exhibiting a controlled deformation distribution, as can be observed in the deformation contour presented in Figure 6 (a). This behavior indicates that the structure is capable of absorbing impact energy effectively without causing significant disruption to the overall structural integrity.

At an impact speed of 50 km/h, deformation increased significantly due to the higher kinetic energy associated with the increased velocity. The deformation remained concentrated in the contact zone and structural transition regions, while still exhibiting a directed and stable deformation pattern, as illustrated by the deformation contour in Figure 6 (b). Although the deformation magnitude was greater than that observed at 30 km/h, the structure did not experience complete failure, indicating that the energy absorption mechanism continued to function effectively under higher energy impact conditions.

Compared to previous studies by Güler et al. [11], [14], which reported greater deformation due to limitations in energy-absorbing elements, the design proposed in this study demonstrates improved performance through the use of a combined aluminum and elastomer material system. The elastomer functions as a nonlinear energy dissipation medium, helping to control the deformation rate during the impact process. Overall, these results indicate that the bumper bar design satisfies crashworthiness principles through a controlled and predictable deformation mechanism, while also confirming the suitability of the explicit dynamics method as an effective evaluation approach prior to physical implementation.

Velocity Response Analysis

The velocity distribution during the impact process shows a significant reduction in the bumper bar structure from initial contact to the final phase of the collision. The velocity response curves indicate that the kinetic energy of the impactor is gradually absorbed by the bumper system without excessive rebound or numerical instability. The velocity contours obtained from the ANSYS Explicit Dynamics simulation and the corresponding velocity–time response curves for impact velocities of 8.33 m/s and 13.89 m/s, which illustrate this progressive reduction in velocity, are presented in Figure 7 (a) and Figure 7 (b), respectively.

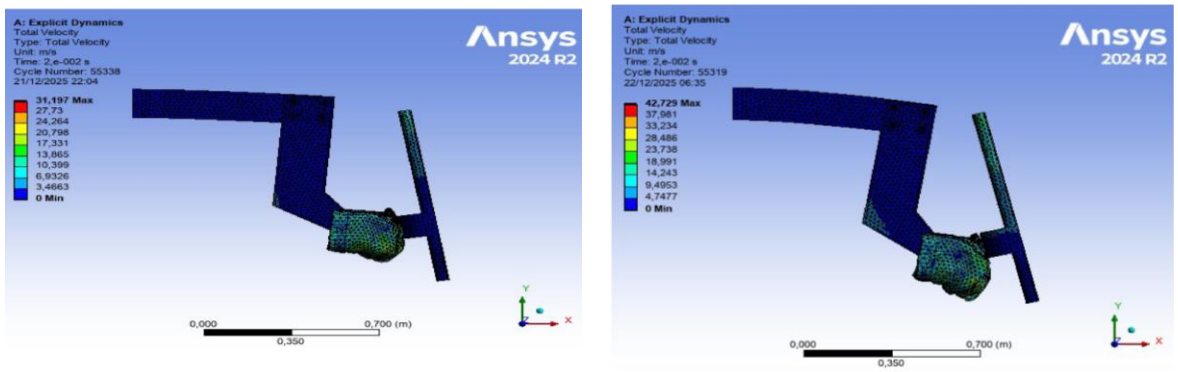

(a) (b)

Figure 7. (a) Velocity response at 8.33 m/s and (b) velocity response at 13.89 m/s

A progressive reduction in velocity indicates that the energy absorption mechanism is functioning effectively, which is consistent with the fundamental principles of passive vehicle safety [1]. This behavior is particularly important for minimizing sudden deceleration peaks, which can increase the risk of injury to passengers. as reflected by the smooth and stable velocity trends shown in Figure 7.

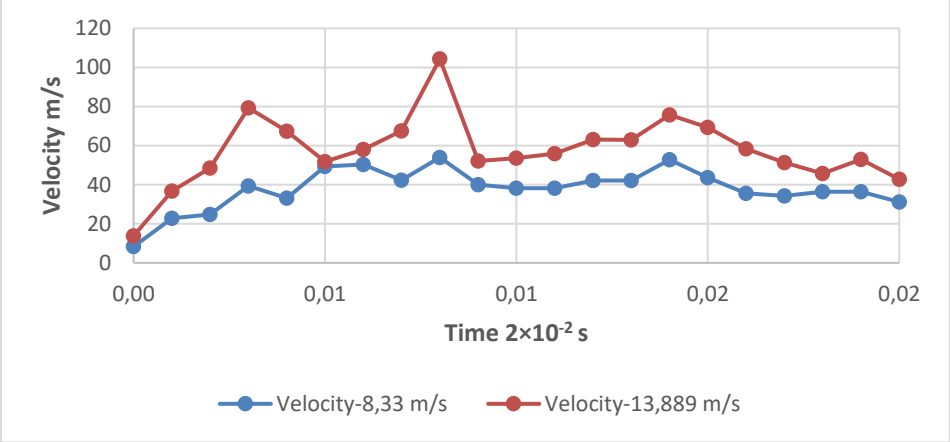

Figure 8. Total impact velocity history

These results are consistent with the findings of Acar and Güler [2], who reported that control of post-impact residual velocity is a key indicator of successful bumper design. The reduction and stabilization of residual velocity after impact, as discussed above, are clearly illustrated by the total impact velocity history curves presented in Figure 8. In addition, the relatively low residual velocity indicates that the reaction forces transmitted to the bus frame structure remain within safe limits.

Therefore, the developed bumper bar design demonstrates not only effective energy absorption capability but also the ability to control the dynamic response of the vehicle during collision events, particularly under low to medium impact velocities of 30–50 km/h, which are commonly encountered in urban traffic conditions [5]. as reflected by the smooth and progressive velocity decay observed in the response curves shown in Figure 8.

Energy Analysis (Energy Absorption)

Energy analysis of the impact simulations shows that the internal energy of the bumper bar structure increases significantly as collision time progresses, representing the ability of the structure to absorb impact energy through material deformation mechanisms. The internal energy curves exhibit a stable upward trend for both impact velocity conditions, without extreme fluctuations, indicating a consistent and numerically stable response during the explicit dynamic simulations. The evolution of internal energy over time for impact velocities of 8.33 m/s and 13.89 m/s, illustrating this stable energy absorption behavior, is presented in Figure 9.

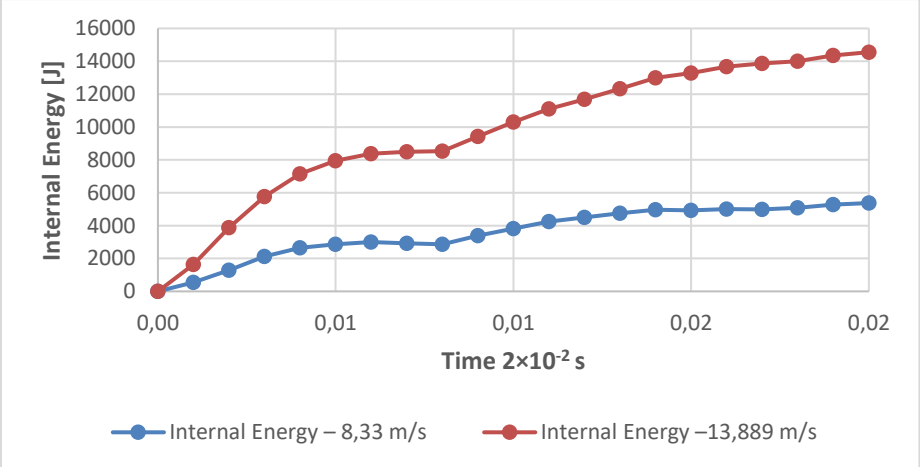

Figure 9. Total internal energy during the impact test

The energy absorption capacity, indicated by the maximum internal energy value, reaches and exceeds the minimum threshold of 5 kJ, as recommended in the adaptation of the 67 Pa. Code §171.44 standard, as evidenced by the peak internal energy levels shown in Figure 9. These results are consistent with experimental and numerical studies on modern automotive bumper systems, which demonstrate that controlled structural designs enhance the stability of energy absorption [3], [5].

This confirms that the proposed bumper bar design provides sufficient energy absorption capability to mitigate collision impacts at typical urban bus operating speeds, primarily through controlled plastic deformation. The sustained increase and plateauing of internal energy observed in Figure 9 further indicate that the deformation process remains stable throughout the impact event.

Compared to previous studies that focused mainly on passenger vehicles [15], the findings of this study demonstrate that a regulation-based design approach evaluated using explicit impact simulations can yield more stable and predictable internal energy responses. These results further support the use of numerical simulation as a primary tool for structural performance evaluation, with the potential to reduce the need for physical testing by up to 80% without compromising result reliability [1].

Overall, the high level of internal energy absorbed during the impact process, combined with controlled deformation behavior, indicates that the proposed bumper bar design is suitable as a technical basis for developing national regulations for urban bus bumper bars in Indonesia.

CONCLUSIONS

This study developed regulatory recommendations for urban bus bumper bars through the adaptation of the 67 Pa. Code §171.44 standard using an explicit dynamics simulation approach. The analysis results demonstrate that the proposed bumper bar design satisfies passive safety performance criteria. Although the maximum stress at an impact speed of 50 km/h exceeds the yield strength of Aluminum Alloy 6061-T6 (280 MPa), the resulting deformation remains localized and does not lead to global structural failure. This confirms acceptable crashworthiness performance under urban operating conditions, with controlled maximum deformation below 150 mm at a speed of 30 km/h and sufficient energy absorption capacity of at least 5 kJ.

The concentrated yet controlled stress distribution, localized deformation without excessive intrusion into the passenger cabin, and progressive reduction in velocity indicate that the proposed design is effective in absorbing impact energy and protecting both the vehicle structure and passengers in low to medium speed collision scenarios ranging from 30 to 50 km/h. The combination of Aluminum Alloy 6061-T6 and elastomer (EPDM rubber) provides effective energy absorption, deformation control, and uniform stress distribution. In addition, the bumper geometry incorporating a web and flange system plays a significant role in reducing local stress concentrations.

The simulation results meet the performance criteria adapted from Pennsylvania Code §171.44, including controlled deformation and optimal energy absorption. The resulting regulatory recommendations include dimensional specifications, namely a height of 400 to 600 mm and a minimum width of 2000 mm, material requirements with a minimum yield strength of 250 MPa, and performance-based criteria that can support the formulation of safety standards for urban bus bumper bars in Indonesia and contribute to the revision of Minister of Transportation Regulation No. 33 of 2018. The proposed regulatory framework is expected to address the existing technical regulatory gap for M3 category buses with a gross vehicle weight of less than 12 tons. Furthermore, the application of the Finite Element Method with explicit dynamics has proven to be an effective approach for crashworthiness evaluation, offering high accuracy and cost efficiency, with potential cost reductions of up to 80% compared to physical testing. Within the scope of this research, the results also provide a simulation database that can be further developed for future studies.

RECOMMENDATIONS

Based on the results and analysis of this study, several recommendations for future research are proposed:

1. Conduct experimental validation through full-scale physical impact testing to verify the accuracy of the numerical simulation model and provide comparative experimental data.
2. Expand testing scenarios to include higher impact speeds exceeding 50 km/h and more complex loading conditions, such as oblique impacts and offset collisions.
3. Investigate alternative material combinations, including hybrid aluminum–composite systems or metal matrix composites, which offer reduced weight and enhanced energy absorption capability.
4. Develop a more comprehensive parametric analysis of bumper geometry using optimization methods such as multi-objective optimization, TOPSIS, or response surface methodology.
5. Explore the integration of active bumper systems and sensor technologies to enhance real-time safety responses in modern urban buses.
6. Conduct life cycle cost analysis and assess mass production feasibility from a manufacturing perspective to ensure effective and sustainable implementation by the national car body industry.

The findings of this study align with international trends in the development of crashworthiness-based bus bumper systems and the increasing use of open-access numerical approaches, particularly finite element method-based analyses, in contemporary research [4], [5], [22].

ACKNOWLEDGEMENT

The authors would like to express their sincere gratitude to the Bengkulu Class III Land Transportation Management Agency and the Tegal Road Transportation Safety Polytechnic for their support in providing facilities and a conducive research environment. Appreciation is also extended to PT Anindya Mitra Internasional and the Special Region of Yogyakarta Transportation Agency for facilitating access to Trans Jogja bus operational data, which was essential to the successful completion of this research. The authors further acknowledge all individuals and institutions who contributed, either directly or indirectly, to the realization of this study.

REFERENCES

[1] W. Abramowicz and N. Jones, "Dynamic axial crushing of circular tubes," *Int. J. Impact Eng.*, vol. 2, no. 3, pp. 263–281, 1984, doi: https://doi.org/10.1016/0734-743X(84)90010-1.

[2] E. Acar, B. Yilmaz, M. A. Güler, and M. Altin, "Multi-fidelity crashworthiness optimization of a bus bumper system under frontal impact," *J. Brazilian Soc. Mech. Sci. Eng.*, vol. 42, no. 9, p. 493, 2020, doi: https://doi.org/10.1007/s40430-020-02572-3.

[3] E. S. Yeshanew *et al.*, "Experimental investigation and crashworthiness analysis of 3D printed carbon PA automobile bumper to improve energy absorption by using LS-DYNA," *Adv. Mech. Eng.*, vol. 15, no. 6, p. 16878132231181058, Jun. 2023, doi: https://doi.org/10.1177/16878132231181058.

[4] B. M. Ramadhan, B. W. Ndimila, and I. I. Mwesigwa, "Crashworthiness Analysis of Automotive Frontal Bumper Materials," *Int. J. Mech. Eng. Appl.*, vol. 13, no. 5, pp. 157–169, Oct. 2025, doi: https://doi.org/10.11648/j.ijmea.20251305.12.

[5] I. E. Asres, E. G. Koricho, and E. Z. Kassa, "Investigating the effect of localized heat treatment and bioinspired structure on the crashworthiness of bumper subsystem.," *Heliyon*, vol. 11, no. 1, p. e40958, Jan. 2025, doi: https://doi.org/10.1016/j.heliyon.2024.e40958.

[6] A. D. Bank, *Sustainable Transport Solutions*. Manila: ADB, 2021.

[7] K. Chandrashekar and D. Murthy, "Design and analysis of automotive bumper," *Int. J. Mech. Eng. Technol.*, vol. 11, no. 3, pp. 45–58, 2020.

[8] K. Polri, "Statistik Kecelakaan Lalu Lintas 2022." Jakarta, 2023.

[9] S. P. Santosa, T. Wierzbicki, A. G. Hanssen, and M. Langseth, "Experimental and numerical studies of foam-filled sections," *Int. J. Impact Eng.*, vol. 24, no. 5, pp. 509–534, 2000, doi: https://doi.org/10.1016/S0734-743X(99)00036-6.

[10] K. N. K. Transportasi, "Laporan Investigasi Tabrakan Bus Transjakarta BMP 240 dengan Bus Transjakarta BMP 211, 25 Oktober 2021," Komite Nasional Keselamatan Transportasi, Jakarta, 2021.

[11] K. P. R. Indonesia, "Statistik Transportasi Darat 2023," Kementerian Perhubungan Republik Indonesia, Jakarta, 2023.

[12] B. P. Statistik, "Estimasi Kerugian Ekonomi Kecelakaan Lalu Lintas," Badan Pusat Statistik, Jakarta, 2022.

[13] K. P. R. Indonesia, "Peraturan Menteri Perhubungan Nomor 33 Tahun 2018 tentang Pengujian Tipe Kendaraan Bermotor." Kementerian Perhubungan Republik Indonesia, Jakarta, 2018.

[14] M. A. Güler, M. E. Cerit, S. K. Mert, and E. Acar, "Experimental and numerical study on the crashworthiness evaluation of an intercity coach under frontal impact conditions," *Proc. Inst. Mech. Eng. Part D J. Automob. Eng.*, vol. 234, no. 13, pp. 3026–3041, Jun. 2020, doi: https://doi.org/10.1177/0954407020927644.

[15] P. D. of Transportation, "Pennsylvania Code Title 67 Chapter 171." PennDOT, Harrisburg, 2019.

[16] A. Setiawan and H. Wicaksono, "Survey on bus body manufacturers in Indonesia," *J. Soc. Automot. Eng. Indones.*, vol. 6, no. 2, pp. 78–89, 2022.

[17] D. P. D. I. Yogyakarta, "Spesifikasi Teknis Trans Jogja," Yogyakarta, 2023.

[18] A. A. Ramadhan, S. Talib, and A. R. A. Rafie, "Comparative study on crashworthiness of bumper materials," *J. Mech. Eng. Sci.*, vol. 13, no. 4, pp. 5835–5849, 2019.

[19] L. P. Sukoco, F. Tohom, and E. Pranoto, "Optimalisasi Material dan Profil Reinforcement Beam Guna Meningkatkan Energi Serap Benturan Berbasis Simulasi FEM," *J. Rekayasa Mesin*, vol. 16, no. 1, pp. 327–340, May 2025, doi: https://doi.org/10.21776/jrm.v16i1.2106.

[20] M. A. Aravy, L. Sukoco, N. Al Bana, M. Rosyid, and H. Wibowo, "Pengembangan Ergonomi Kursi Belajar Berbasis Desain dan Simulasi Elemen Hingga," *J. Promot. Prev.*, vol. 8, no. 6, pp. 1604–1612, Dec. 2025, doi: https://doi.org/10.47650/jpp.v8i6.2387.

[21] U. N. E. C. for Europe, "UN ECE Regulation No. 42: Uniform provisions concerning the approval of vehicles with regard to their front and rear protective devices." United Nations, 1980.

[22] E. T. W. Federation, "Norwegian 2025 Report on Crashworthiness of Buses," European Transport Workers' Federation, 2025. [Online]. Available: https://www.etf-europe.org/wp-content/uploads/2025/10/Norwegian-2025-Report-on-Crashworthiness-of-buses.pdf

PISTON
Journal of Technical Engineering:

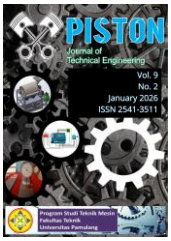

Optimizing the Number of Curved Turbine Blades on Flettner Rotors for Sustainable Ship Propulsion Without Fuel

Novan Habiburrahman[1,a)], Indri Triawati[1]

[1]*Universitas Kristen Cipta Wacana, Jl. Karel Satsuit Tubun No. 28A, Kebonsari, Sukun District, Malang City, East Java 65149, Indonesia*

E-mail: [a)] novanhabiburrahman@gmail.com

Received: September 12, 2025 *Revision: January 11, 2026* *Accepted: January 16, 2026*

Abstract: The use of vertical rotating cylinders based on the Magnus effect as an alternative propulsion system for ships has been explored since the early 20th century. By harnessing lateral wind, such rotors are capable of generating thrust to replace conventional sails while simultaneously reducing fossil fuel consumption. However, the efficiency of conventional Flettner rotors remains limited due to their reliance on an external energy supply from driving motors. The novelty of this study lies in the development of a Flettner rotor integrated with quarter-circular blades mounted coaxially to enable self-rotation. This design differs from previous studies that predominantly employed half-circular blades or full rotors, and it is expected to enhance the power coefficient (C_p) and torque coefficient (C_v) while maintaining more compact dimensions. This research aims to determine the optimal configuration of blade numbers (2, 4, 8, and 16) and aspect ratio (AR) that delivers superior aerodynamic performance for ship propulsion applications. An experimental approach was conducted using wind tunnel testing of scaled models. Variations in blade number were evaluated based on key performance parameters, including rotor speed, torque, thrust, and the coefficients C_p and C_v. Data acquisition employed RPM sensors, load cells, and a microcontroller-based system. Statistical analysis was applied to compare each blade configuration against the initial hypothesis that increasing the number of blades improves rotor performance up to a certain limit, beyond which excessive blade numbers reduce efficiency due to increased drag. The findings of this research are expected to contribute to the advancement of more efficient, autonomous, and sustainable ship propulsion systems through the use of a Flettner rotor driven purely by wind energy.

Keywords: Energy Conversion, Flettner Rotor, Vertical-Axis Wind Turbine, Power Coefficient (C_p), Torque Coefficient (C_v), Magnus Effect.

Abstrak: *Penggunaan silinder berputar vertikal berbasis efek Magnus sebagai sistem propulsi alternatif pada kapal telah diperkenalkan sejak awal abad ke-20. Dengan memanfaatkan angin lateral, rotor ini mampu menghasilkan gaya dorong yang menggantikan peran layar konvensional sekaligus berpotensi mengurangi konsumsi bahan bakar fosil. Namun, efisiensi sistem rotor Flettner konvensional masih terbatas karena membutuhkan suplai energi eksternal dari motor penggerak. Kebaruan penelitian ini terletak pada pengembangan rotor Flettner dengan integrasi sudu berbentuk seperempat lingkaran (¼ lingkaran) yang dipasang secara koaksial sebagai pemutar mandiri. Desain ini berbeda dari penelitian sebelumnya yang umumnya menggunakan sudu setengah lingkaran (½ lingkaran) atau rotor penuh, sehingga diharapkan mampu meningkatkan koefisien daya (C_p) dan koefisien torsi (C_v) dengan dimensi yang lebih ringkas. Penelitian ini bertujuan untuk menentukan konfigurasi jumlah sudu (2, 4, 8, dan 16) serta aspect ratio (AR) yang optimal guna menghasilkan performa aerodinamika terbaik untuk aplikasi propulsi kapal. Metode penelitian dilakukan secara eksperimental melalui pengujian model berskala pada terowongan angin (wind tunnel). Variasi jumlah sudu diuji terhadap parameter performa utama, yaitu kecepatan putar rotor, torsi, gaya dorong, serta nilai koefisien C_p dan C_v. Data diperoleh menggunakan sensor RPM, load cell, dan sistem akuisisi data berbasis mikrokontroler. Analisis dilakukan dengan pendekatan statistik untuk membandingkan setiap konfigurasi sudu terhadap hipotesis awal bahwa peningkatan jumlah sudu hingga batas tertentu akan meningkatkan performa rotor, sedangkan jumlah sudu yang terlalu banyak justru menurunkan efisiensi akibat peningkatan gaya hambat (drag). Hasil penelitian ini diharapkan dapat memberikan kontribusi dalam pengembangan sistem propulsi kapal yang lebih efisien, mandiri, dan berkelanjutan melalui pemanfaatan rotor Flettner berbasis energi angin murni.*

Kata kunci: *Konversi Energi, Rotor Flettner, Turbin Angin Sumbu Vertikal, Koefisien Daya (C_p), Koefisien Torsi (C_v), Efek Magnus.*

INTRODUCTION

Maritime transportation plays a vital role in supporting global trade, with more than 80% of the world's trade volume carried via sea routes [1]. However, despite its strategic importance, this sector is also a major contributor to greenhouse gas (GHG) emissions, particularly carbon dioxide (CO_2), sulfur oxides (SO_x), and nitrogen oxides (NO_x). According to the International Maritime Organization (IMO), the maritime sector generated approximately 2.9% of global CO_2 emissions in 2018, and without significant technological interventions, this figure is projected to increase by 90% to 130% by 2050 [2]. These circumstances highlight the urgency of developing efficient, environmentally friendly, and renewable-energy-based ship propulsion technologies as a pathway toward sustainable maritime transportation.

One of the most prominent Wind-Assisted Propulsion Systems (WAPS) is the Flettner rotor, a propulsion device based on the Magnus effect that utilizes the rotation of a vertical cylinder to generate additional thrust. The Flettner rotor was first introduced by Anton Flettner in the early 1920s and was applied to the ship *Buckau* (later known as *Baden-Baden*). Its working principle is based on the Magnus effect, in which cylinder rotation induces differences in airflow velocity on opposite sides of the surface, resulting in a pressure differential that produces lift perpendicular to the wind direction [3]. When properly oriented, this lift force can be converted into thrust to propel the ship. Several studies have demonstrated that Flettner rotors can significantly reduce fuel consumption and emissions [4]–[6]. Angelini et al. [7], for example, reported that the application of Flettner rotors on cargo vessels could achieve fuel savings of up to 15%.

Figure 1. Example of Flettner rotor installation on a maritime vessel [2]

Despite these advantages, conventional Flettner rotors still face limitations, primarily due to their reliance on electric or mechanical drive motors to maintain rotation, which makes them dependent on additional energy sources [8], [9]. To address this limitation, the concept of integrating the Flettner rotor with a Vertical Axis Wind Turbine (VAWT) in a coaxial configuration has been proposed. In this design, the VAWT serves as the primary driver, generating torque directly from wind energy to enable self-rotation of the Flettner rotor, thereby eliminating the need for supplementary fossil-fuel-based energy input [7], [10], [11].

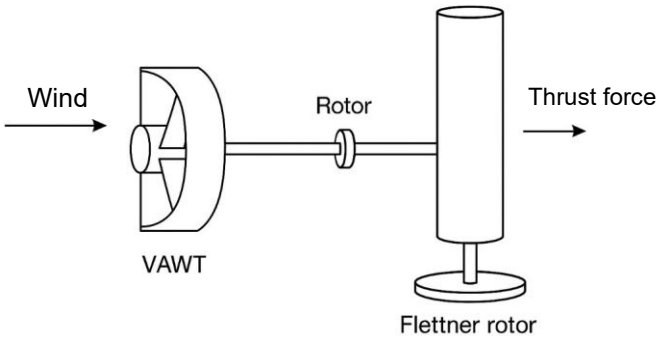

Figure 2. Concept of coaxial integration of a VAWT–Flettner system [11], [12]

The performance of a Vertical Axis Wind Turbine (VAWT) is strongly influenced by blade design, particularly blade shape and number. In this study, quarter-circular blades (¼ circular blades) were employed, as this geometry has been shown to generate superior starting torque while reducing aerodynamic drag compared to semi-circular configurations [13]–[15]. The number of blades was varied at 2, 4, 8, and 16, since this parameter directly affects flow interaction, starting torque, and overall aerodynamic efficiency [16]–[18].

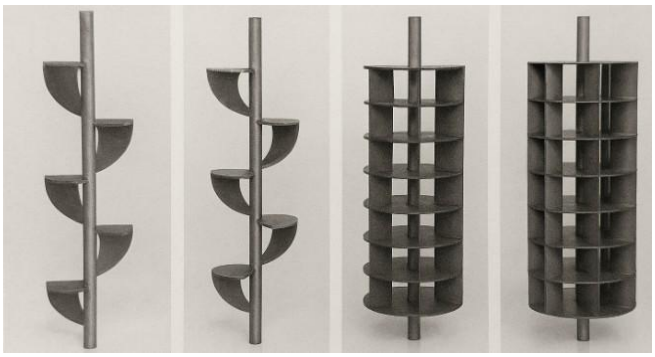

Figure 3. Variations in quarter-circular blade numbers with 2, 4, 8, and 16 blades [6], [16]–[18]

In addition to blade shape and number, the aspect ratio (AR) is a critical geometrical parameter in the design of a Flettner–VAWT rotor. The AR is defined as the ratio of rotor height to rotor diameter or end-plate diameter, and it significantly influences aerodynamic characteristics such as the power coefficient (C_p) and torque coefficient (C_v) [19], [20]. Previous studies have shown that certain AR values can achieve optimal conditions, where thrust is enhanced without a substantial increase in drag [19], [21]. Therefore, in this study, the rotor models were designed based on optimal AR values identified from the literature to ensure representative and reliable results.

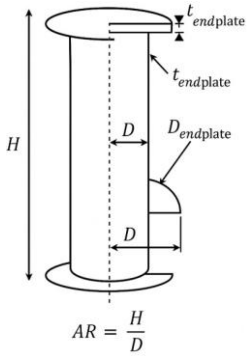

Figure 4. Schematic representation of the aspect ratio (AR) in Flettner–VAWT rotors [5], [19]–[21]

Based on the literature review, previous research on Flettner rotors has focused on rotor shape optimization using computational fluid dynamics (CFD), investigations of end-plate effects, and integration with other propulsion systems. However, no experimental study has specifically examined the influence of quarter-circular blade numbers in a coaxial VAWT–Flettner configuration while considering an optimal aspect ratio. This study seeks to address that research gap.

The research problem can be formulated as follows: *How does variation in the number of quarter-circular blades (2, 4, 8, and 16) in a VAWT affect torque, rotational speed, thrust, as well as the power coefficient (C_p) and torque coefficient (C_v) of a Flettner rotor?*

Accordingly, the objective of this study is to determine the optimal configuration of quarter-circular blade numbers combined with an optimal AR that delivers the best aerodynamic performance under wind tunnel testing conditions. The novelty of this research lies in its experimental approach using laboratory-scale models designed with an optimal AR, while systematically evaluating the influence of quarter-circular blade numbers on the performance of a coaxial VAWT–Flettner system. This area remains largely unexplored.

The research hypothesis proposes that increasing the number of blades will improve rotor performance up to a certain limit, approximately eight blades. Beyond this limit, excessive blade numbers such as sixteen are expected to reduce efficiency due to increased aerodynamic drag.

METHODS

This study employed an experimental approach to evaluate the influence of variations in quarter-circular curved blades (¼ circular blades) of a Vertical Axis Wind Turbine (VAWT) on the performance of a Flettner rotor in generating thrust for fuel-free ship propulsion. All stages of the research were conducted systematically, beginning with a literature review, followed by physical model design and fabrication, wind tunnel testing, and statistical data analysis to determine the optimal blade configuration.

To provide a clear overview of the experimental procedure, the overall research workflow is summarized in Figure 5. The methodology consisted of a literature-based design framework, physical model fabrication, wind tunnel testing, and statistical data analysis.

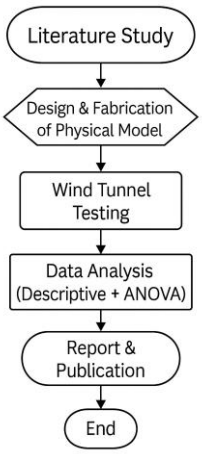

Figure 5. Research workflow illustrating the experimental stages of the Flettner–VAWT rotor study

Stage 1. Literature Review

A focused literature review was conducted to establish the experimental framework for the coaxial Flettner–VAWT rotor system. The review covered the Magnus effect, the aerodynamic behavior of rotating cylinders, and the performance characteristics of vertical axis wind turbines relevant to wind-assisted ship propulsion. Key parameters influencing rotor performance were identified, including blade geometry, number of blades, wind speed, and rotor aspect ratio (AR). Emphasis was placed on studies involving experimental validation and wind tunnel testing to ensure the practical relevance of the selected parameters.

The outcomes of the literature review were directly applied to the determination of blade configuration, geometric proportions, and test variables of the laboratory-scale prototype evaluated in the wind tunnel. This approach ensured that the experimental setup was aligned with established aerodynamic principles while addressing unresolved limitations in self-rotating Flettner rotor designs

Stage 2. Physical Model Design and Fabrication

In this stage, laboratory-scale physical models of the coaxial Flettner–VAWT rotor were designed and fabricated for wind tunnel testing. The rotor employed quarter-circular curved blades arranged symmetrically around a vertical rotating cylinder. Four blade-number configurations were investigated, namely 2, 4, 8, and 16 blades, to evaluate the influence of blade count on aerodynamic performance. These configurations were selected based on previous studies reporting a non-linear relationship between blade number, starting torque, and wind energy conversion efficiency [6], [17].

The geometric design of the rotor was defined by rotor diameter, blade curvature radius, blade thickness, and rotor height. These parameters collectively determined the aspect ratio (AR). The AR was selected based on values reported in the literature to achieve a balance between thrust generation and aerodynamic drag, ensuring representative performance under wind tunnel conditions.

The physical models were fabricated using 3D printing technology to achieve high geometric accuracy and repeatability. Lightweight polymer materials with sufficient mechanical strength were selected to maintain structural rigidity while minimizing inertial effects during rotation. This fabrication method enabled precise realization of blade curvature and ensured consistent geometry across all blade-number variations.

Stage 3. Wind Tunnel Testing

Wind tunnel experiments were conducted to evaluate the aerodynamic performance of the coaxial Flettner–VAWT rotor under controlled airflow conditions. Tests were performed at multiple wind speed settings to represent typical operational wind conditions encountered by maritime vessels during wind-assisted propulsion.

The wind speed was varied within a range of approximately 9 to 15 m/s, corresponding to moderate to relatively strong apparent wind conditions commonly experienced by ships operating in open-sea environments. This range was selected to ensure realistic operating conditions while remaining within the stable operating limits of the wind tunnel facility. Similar wind speed ranges have been reported in previous experimental studies on Flettner rotors and wind-assisted ship propulsion systems.

For each wind speed setting, the following parameters were measured:

- Rotor rotational speed (RPM), measured using a digital tachometer.
- Thrust force (F_t), measured using a load cell connected to a data acquisition system.
- Power coefficient (C_p), calculated from measured torque and rotational speed.
- Torque coefficient (C_v), determined based on the aerodynamic torque acting on the rotor.

Each blade-number configuration (2, 4, 8, and 16 blades) was tested repeatedly at each wind speed to ensure data consistency and repeatability. The experimental setup and measurement arrangement used in the wind tunnel testing are illustrated in Figure 6.

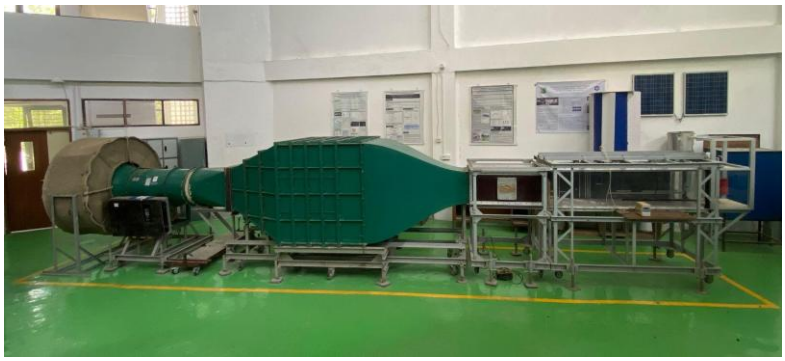

Figure 6. Experimental setup of the Flettner–VAWT rotor in the wind tunnel. Source: Laboratory documentation

Stage 4. Data Analysis

Data analysis was conducted using both descriptive and inferential statistical approaches.

a. Descriptive Analysis
Experimental data were presented in the form of tables and graphs to illustrate trends in blade-number variation with respect to rotor rotational speed, thrust force, power coefficient (C_p), and torque coefficient (C_v). Graphs of thrust versus wind speed were used to evaluate rotor performance stability across operating conditions.

b. Inferential Statistical Analysis
To assess whether variations in blade number had a statistically significant effect on rotor performance, a one-way Analysis of Variance (ANOVA) was applied. The ANOVA compared the mean values of measured parameters for the four blade configurations. When statistically significant differences were observed at a significance level of $p < 0.05$, Tukey's Honest Significant Difference (HSD) post hoc test was conducted to identify which blade configurations differed significantly. With this approach, the research findings demonstrate not only observable performance trends but also statistically validated results. This ensures that conclusions regarding the optimal blade number are supported by scientific evidence.

RESULT AND DISCUSSION

The experimental investigation of the coaxial Flettner–VAWT rotor equipped with quarter-circular blades was conducted using four blade-number configurations, namely 2, 4, 8, and 16 blades, in accordance with the experimental design described in the Methods section. For each configuration, the measured parameters included aerodynamic drag, thrust, rotor rotational speed (RPM), dynamic pressure (mmH_2O), and wind speed (m/s). Rather than presenting repetitive descriptions for each configuration, the results are discussed comparatively to highlight the influence of blade number on aerodynamic performance. The analysis focuses on key performance indicators, including thrust generation, rotational speed, and the trade-off between thrust and aerodynamic drag across the tested wind speed range.

Overall, the experimental results reveal clear performance differences among the four configurations. Rotors with fewer blades achieved higher rotational speeds but generated lower thrust, while configurations with a larger number of blades produced greater thrust at the expense of reduced RPM due to increased aerodynamic resistance. The following subsections present a comparative analysis of selected blade-number configurations to identify the most effective design for wind-assisted ship propulsion.

Four-Blade Rotor

In the four-blade configuration, the rotor achieved a maximum rotational speed of 2024 RPM at a wind velocity of 14.11 m/s, while the maximum thrust generated was 0.27 N. These results indicate that the four-blade rotor favors high rotational speed rather than thrust production. The relatively small number of blades reduces aerodynamic drag and mechanical loading, allowing the rotor to accelerate rapidly as wind speed increases. However, the limited effective wind capture area restricts the magnitude of thrust produced.

Table 1. Experimental results for the four-blade rotor

No	Drag		Thrust		Rpm	Hz	Dynamic Pressure (mmH2O)	Wind Speed (m/s)
	gr	N	gr	N				
1	26.23	0.26	0	-	202.7	28	5.04	8.98
2	27.3	0.27	0	-	257	28	5.22	9.14
3	28.38	0.28	0	-	278	29	5.41	9.31
4	35.56	0.35	0	-	298.3	30	5.6	9.47
5	42.74	0.42	0	-	301	30	5.8	9.64
6	44.44	0.44	0	-	336.2	30	6	9.8
7	46.14	0.45	0	-	353.3	31	6.2	9.96
8	48.05	0.47	0	-	375.5	32	6.4	10.12
9	49.96	0.49	0	-	394.9	32	6.6	10.28
10	50.56	0.50	5.59	0.05	410	32	6.81	10.44
11	51.15	0.50	6.73	0.07	430	33	7.02	10.6
12	52.06	0.51	7.45	0.07	442.1	34	7.24	10.77
13	52.98	0.52	7.68	0.08	457	34	7.46	10.93
14	55.4	0.54	10.21	0.10	462.4	34	7.68	11.09
15	57.81	0.57	13.36	0.13	470.8	35	7.91	11.25
16	58.04	0.57	15.03	0.15	475	36	8.13	11.41
17	58.27	0.57	16.27	0.16	478	36	8.35	11.56
18	58.81	0.58	17.23	0.17	485	36	8.59	11.73
19	59.35	0.58	18.55	0.18	500	37	8.83	11.89
20	60.16	0.59	18.8	0.18	539	38	9.08	12.06
21	60.98	0.60	18.51	0.18	548	38	9.33	12.22
22	62.52	0.61	20.34	0.20	1492.9	38	9.57	12.38
23	64.06	0.63	21.05	0.21	1525	39	9.8	12.53
24	65.78	0.65	21.42	0.21	1580	40	10.05	12.68
25	67.51	0.66	21.2	0.21	1630	40	10.3	12.84
26	70.13	0.69	23.46	0.23	1667.1	40	10.57	13.01
27	72.75	0.71	23.9	0.23	1705	41	10.83	13.17
28	74.53	0.73	25.26	0.25	1768	42	11.09	13.33
29	76.31	0.75	25.57	0.25	1819.2	42	11.35	13.48
30	77.94	0.76	26.37	0.26	1870.4	42	11.62	13.64
31	79.58	0.78	28.6	0.28	1921.6	43	11.9	13.8
32	81.12	0.80	29.41	0.29	1972.8	44	12.16	13.95
33	82.66	0.81	27.99	0.27	2024	44	12.43	14.11

The data presented in Table 1 show that the increase in rotational speed with wind velocity is not strictly linear, with a pronounced rise in RPM occurring at wind speeds above approximately 12 m/s. This behavior suggests a transition in the rotor operating regime. At lower wind speeds below approximately 11 m/s, the rotor operates near its cut-in condition, where the aerodynamic torque generated by the quarter-circular blades is partially counterbalanced by bearing friction, structural inertia, and flow separation effects. Under these conditions, incremental increases in wind speed result in only gradual increases in rotational speed.

Once the wind speed exceeds this threshold, the aerodynamic torque becomes sufficient to overcome frictional and inertial resistance, causing the rotor to enter a low-load, high-speed operating regime. At higher Reynolds numbers, improved flow attachment around the rotating cylinder and blades further reduces separation losses and enhances rotational efficiency. These combined effects explain the rapid increase in RPM observed at higher wind speeds despite relatively modest changes in wind velocity.

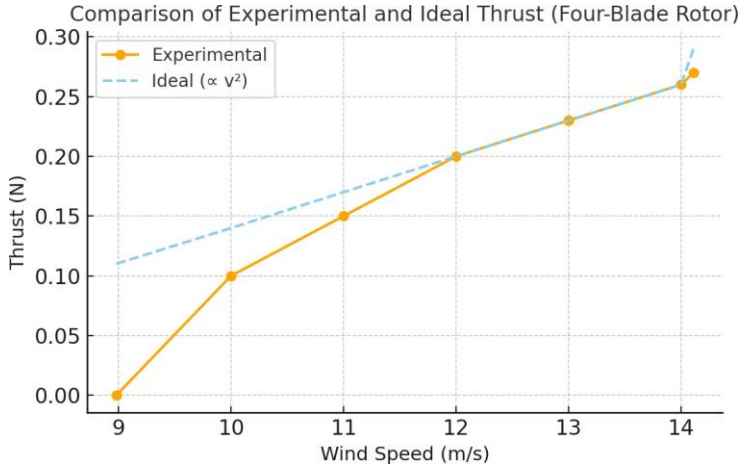

Figure 7. Thrust versus wind speed for the four-blade rotor

The relationship between wind speed and thrust for the four-blade rotor is shown in Figure 7. Thrust increases approximately linearly, rising from 0 N at 8.98 m/s to a maximum of 0.27 N at 14.11 m/s. This trend indicates a consistent response to increasing wind speed; however, the absolute thrust magnitude remains relatively small compared to configurations with a larger number of blades.

When compared with the ideal quadratic relationship between thrust and wind speed (T proportional to v squared), the experimental results deviate from the theoretical curve in the low-to-medium wind speed range of 9 to 11 m/s. In this region, measured thrust values fall below ideal predictions due to aerodynamic losses, mechanical friction, and localized turbulence around the rotating cylinder and blades. At wind speeds above approximately 13 m/s, the experimental thrust curve approaches the theoretical trend, indicating improved aerodynamic effectiveness under stronger flow conditions.

Table 2. One-way ANOVA results for the four-blade rotor

Source	Sum of Squares (SS)	df	Mean Square (MS)	F	p-value
Regression (linear)	0.04638	1	0.04638	459.58	0.00022
Residual (Error)	0.00030	3	0.00010		
Total	0.04668	4			

To quantify the influence of wind speed on thrust generation, a one-way ANOVA combined with linear regression analysis was performed. The results confirm that wind speed has a statistically significant effect on thrust, with an F-value of 459.58 and $p < 0.05$. The thrust–wind speed relationship is well described by the linear regression model:

$$Y = -0.471 + 0.0532v$$

Despite the strong statistical significance, the relatively low thrust values obtained across the tested wind speed range indicate that the four-blade rotor is aerodynamically responsive but not thrust-efficient. Consequently, this configuration is more suitable for applications requiring high rotational speed and low aerodynamic loading, rather than propulsion systems that demand substantial thrust.

Eight-Blade Rotor

In the eight-blade configuration, the rotor achieved a maximum rotational speed of 1819 RPM at a wind velocity of 14.49 m/s. The highest thrust recorded was 0.55 N at a wind speed of approximately 11.35 m/s, demonstrating a substantial improvement in thrust generation compared to the four-blade configuration. This increase can be attributed to the larger number of blades, which expands the effective wind capture area and enhances the conversion of wind energy into aerodynamic thrust.

At higher wind speeds, however, thrust decreased despite continued increases in wind velocity. This reduction is associated with increased aerodynamic drag and reduced energy conversion efficiency. As a result, the eight-blade rotor exhibits its best performance under medium wind conditions, where it achieves high thrust while maintaining relatively stable rotational speed.

Table 3. Experimental results for the eight-blade rotor

No	Drag		Thrust		Rpm	Hz	Dynamic Pressure (mmH2O)	Wind Speed (m/s)
	gr	N	gr	N				
1	51.92	0.51	0.11	0.00	202.7	17	1.86	5.46
2	52.09	0.51	0.12	0.00	257	18	2.11	5.81
3	53.62	0.53	0.12	0.00	278	19	2.36	6.15
4	60.61	0.59	0.13	0.00	298.3	20	2.62	6.48
5	61.43	0.60	0.13	0.00	301	21	2.88	6.79
6	61.65	0.60	0.13	0.00	336.2	22	3.18	7.14
7	65.29	0.64	0.13	0.00	353.3	23	3.49	7.48
8	76.46	0.75	0.13	0.00	375.5	24	3.8	7.8
9	81.51	0.80	0.13	0.00	394.9	25	4.11	8.11
10	85.16	0.84	0.14	0.00	410	26	4.45	8.44
11	94.12	0.92	0.15	0.00	430	27	4.79	8.76
12	91.41	0.90	0.15	0.00	442.1	28	5.16	9.09
13	96.51	0.95	0.15	0.00	457	29	5.53	9.41
14	99.3	0.97	18.15	0.18	462.4	30	5.92	9.74
15	110.1	1.08	28.28	0.28	470.8	31	6.3	10.04
16	125	1.23	37	0.36	475	32	6.72	10.37
17	133.5	1.31	45	0.44	478	33	7.14	10.69
18	141.8	1.39	56.5	0.55	485	34	7.58	11.02
19	152	1.49	58.5	0.57	500	35	8.04	11.35
20	128.02	1.26	49.09	0.48	539	36	8.5	11.67
21	130.3	1.28	57.42	0.56	548	37	8.96	11.98
22	152.17	1.49	0.18	0.00	1492.9	38	9.43	12.29
23	159.71	1.57	0.19	0.00	1525	39	9.94	12.62
24	165.9	1.63	0.2	0.00	1580	40	10.44	12.93
25	172.8	1.70	0.19	0.00	1630	41	10.92	13.22
26	180.86	1.77	0.2	0.00	1667.1	42	11.46	13.55
27	188.31	1.85	0.2	0.00	1705	43	12.01	13.87
28	195	1.91	0.23	0.00	1768	44	12.56	14.18
29	211.64	2.08	0.25	0.00	1819.2	45	13.12	14.49

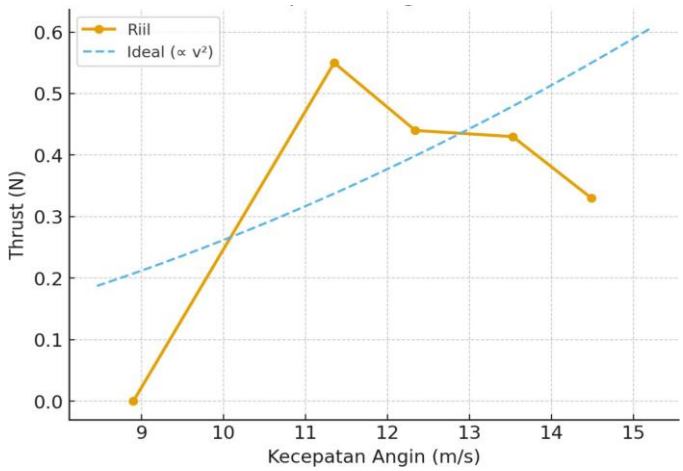

Figure 8. Thrust versus wind speed for the eight-blade rotor

Figure 8 illustrates the relationship between wind speed and thrust for the eight-blade configuration. Thrust increases rapidly in the low-to-medium wind speed range and reaches a maximum value of 0.55 N at 11.35 m/s. Beyond this operating point, thrust declines with further increases in wind speed, dropping to approximately 0.33 N at 14.49 m/s.

This behavior indicates that the eight-blade rotor achieves optimal aerodynamic performance at medium wind speeds. At higher velocities, the decrease in thrust is primarily caused by aerodynamic stall on the blades combined with increased parasitic drag. As wind speed increases beyond the optimal range, flow separation becomes more pronounced on blade surfaces, while the higher blade count intensifies viscous and pressure drag. These effects reduce the effective lift generated by the Magnus-based interaction, leading to a net reduction in thrust.

Compared with the ideal quadratic relationship between thrust and wind speed, the experimental thrust curve initially rises more steeply, reflecting efficient energy extraction at medium wind speeds. After reaching the optimum point, the curve deviates significantly from the theoretical trend and declines, highlighting the trade-off between increased blade number and aerodynamic penalties at higher wind velocities.

Table 4. One-way ANOVA results for the eight-blade rotor

Source	Sum of Squares (SS)	df	Mean Square (MS)	F	p-value
Regression (linear)	0.16523	2	0.08262	13.58	0.0686
Residual (Error)	0.01217	2	0.00609		
Total	0.17740	4			

To further examine the influence of wind speed on thrust generation, a quadratic regression-based ANOVA was conducted. The analysis produced a regression sum of squares of 0.16523 and an error sum of squares of 0.01217, with a total sum of squares of 0.17740. The resulting quadratic regression model is given by:

$$Y = -5.984 + 1.056v - 0.0429v^2$$

This model captures the observed physical behavior, namely the increase in thrust to a peak at medium wind speeds of approximately 11.35 m/s, followed by a decline at higher velocities due to stall and drag effects. The coefficient of determination, $R^2 = 0.93$, indicates that the quadratic model explains most of the observed thrust variation.

The F-test yielded an F-value of 13.58 with a p-value of 0.0686. Although this p-value exceeds the conventional significance threshold of 0.05, the result is influenced by the limited dataset without replication, which reduces the degrees of freedom. From an engineering perspective, the observed thrust peak and subsequent decline remain highly relevant, as they clearly identify the optimal operating range and aerodynamic limitations of the eight-blade rotor.

Overall, despite marginal statistical significance, the combined experimental trends and regression analysis indicate that the eight-blade configuration provides the best compromise between high thrust and stable rotational performance within the practical wind speed range for wind-assisted ship propulsion.

Sixteen-Blade Rotor

The sixteen-blade rotor configuration exhibited a tendency to generate relatively high thrust at the expense of low rotational speed. The maximum RPM recorded was only 389 at a wind speed of 14.42 m/s, which was considerably lower than that of the four- and eight-blade configurations. Nevertheless, the thrust produced was relatively substantial, reaching 0.46 N. This outcome highlights the trade-off between increasing blade number to capture more wind energy and the resulting aerodynamic drag that limits rotor speed..

Table 5. Experimental results for the sizteen-blade rotor

No	Drag		Thrust		Rpm	Hz	Dynamic Pressure (mmH2O)	Wind Speed (m/s)
	gr	N	gr	N				
1	52.46	0.51	0	-	100.8	28	5.04	8.98
2	56.75	0.56	0	-	141.7	29	5.41	9.31
3	85.47	0.84	0	-	202	30	5.8	9.64
4	92.28	0.91	0	-	226	31	6.2	9.96
5	99.93	0.98	0	-	261.2	32	6.6	10.28
6	102.3	1.00	0	-	285.6	33	7.02	10.6
7	105.97	1.04	0	-	290.2	34	7.46	10.93
8	115.62	1.13	0	-	327.3	35	7.91	11.25
9	116.54	1.14	0	-	353.2	36	8.35	11.56
10	118.7	1.16	0	-	357.7	37	8.83	11.89
11	121.97	1.20	0	-	364.6	38	9.33	12.22
12	128.12	1.26	0	-	367.5	39	9.8	12.53
13	135.02	1.32	0	-	370.7	40	10.3	12.84
14	145.5	1.43	1.43	0.01	373.5	41	10.83	13.17
15	152.62	1.50	7.22	0.07	374.9	42	11.35	13.48
16	159.16	1.56	8.67	0.09	377.2	43	11.9	13.8
17	165.33	1.62	9.56	0.09	379.6	44	12.43	14.11
18	180.42	1.77	26.42	0.26	389.2	45	12.99	14.42

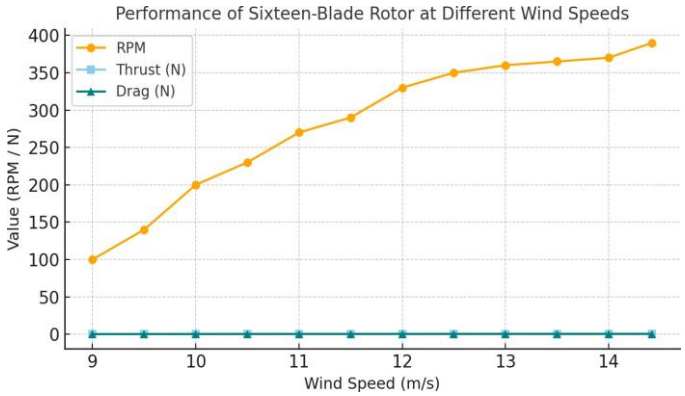

Figure 9. Thrust versus wind speed for the sixteen-blade rotor

The experimental results show that the rotor rotational speed (RPM) increased rapidly in the low wind speed range of 8.9–11 m/s, rising from approximately 100 RPM to 290 RPM. Beyond this range, the rate of RPM increase gradually decreased and tended toward saturation, reaching a maximum value of approximately 389 RPM at a wind velocity of 14.42 m/s. This behavior indicates that the high blade count significantly enhances starting torque, enabling the rotor to initiate and sustain rotation more easily under low wind conditions. However, as wind speed increases, the large number of blades substantially increases aerodynamic resistance, which limits further growth in rotational speed at higher velocities.

In contrast to the RPM trend, the thrust generated by the sixteen-blade rotor increased more gradually and remained relatively stable across the tested wind speed range, reaching a maximum value of 0.46 N at 14.42 m/s. Although this thrust level is higher than that of the four-blade configuration at low wind speeds, the associated aerodynamic drag is considerable. The drag force increased continuously with wind velocity, reaching approximately 1.84 N at the highest test speed. The drag behavior follows a quadratic trend with respect to wind speed, which significantly reduces the overall aerodynamic efficiency of the rotor at medium-to-high wind velocities.

From an aerodynamic standpoint, these results indicate that the sixteen-blade configuration is particularly well suited for low wind operating conditions, where high starting torque and relatively stable thrust are desirable. However, at medium and high wind speeds, the rotor becomes increasingly inefficient due to the combined effects of limited RPM growth and excessive parasitic drag.

Table 6. One-way ANOVA results for the sixteen-blade rotor

Source	Sum of Squares (SS)	df	Mean Square (MS)	F	p-value
Regression (linear)	0.11776	1	0.11776	15.88	0.0283
Residual (Error)	0.02224	3	0.007415		
Total	0.14000	4			

To quantitatively evaluate the influence of wind speed on thrust generation, a one-way ANOVA based on linear regression was performed. The analysis yielded a regression sum of squares (SSR) of 0.11776, an error sum of squares (SSE) of 0.02224, and a total sum of squares (SST) of 0.14000. The corresponding linear regression model describing the thrust–wind speed relationship is given by:

$$Y = -0.655 + 0.0815v$$

This model indicates a positive linear relationship between wind speed and thrust, with thrust increasing consistently from 0 N at 8.92 m/s to 0.46 N at 14.42 m/s. The F-test produced an F-value of 15.88 with a p-value of 0.0283, which is below the conventional significance threshold ($p < 0.05$). Therefore, the effect of wind speed on thrust for the sixteen-blade rotor can be considered statistically significant.

Unlike the eight-blade configuration, which exhibited a quadratic thrust trend with a clear peak followed by a decline, the sixteen-blade rotor shows a monotonic and stable increase in thrust across the tested wind speed range. Nevertheless, despite this statistical significance, the engineering performance of the sixteen-blade rotor is constrained by its relatively low maximum RPM and the substantial aerodynamic drag generated at higher wind speeds.

In practical terms, the sixteen-blade rotor provides strong starting torque and reliable thrust generation under low wind conditions, making it suitable for applications where wind availability is limited. However, for medium-to-high wind regimes, its overall efficiency remains inferior to configurations with fewer blades due to excessive drag and restricted rotational acceleration. This trade-off becomes clearer when the sixteen-blade rotor is compared directly with the four- and eight-blade configurations, as discussed in the following subsection.

Comparison of the Four-, Eight-, and Sixteen-Blade Rotors

After conducting experimental testing of the Flettner–VAWT rotor with different blade numbers (4, 8, and 16), performance data were obtained in terms of thrust, drag, and rotational speed (RPM) under various wind speed conditions. To assess differences in performance characteristics across the configurations, the experimental thrust results of the three rotors were compared with the ideal theoretical curve, which follows the quadratic velocity law (T proportional to v squared). This comparison was intended to evaluate how closely the experimental performance approached the ideal condition and to identify the strengths and limitations of each rotor configuration.

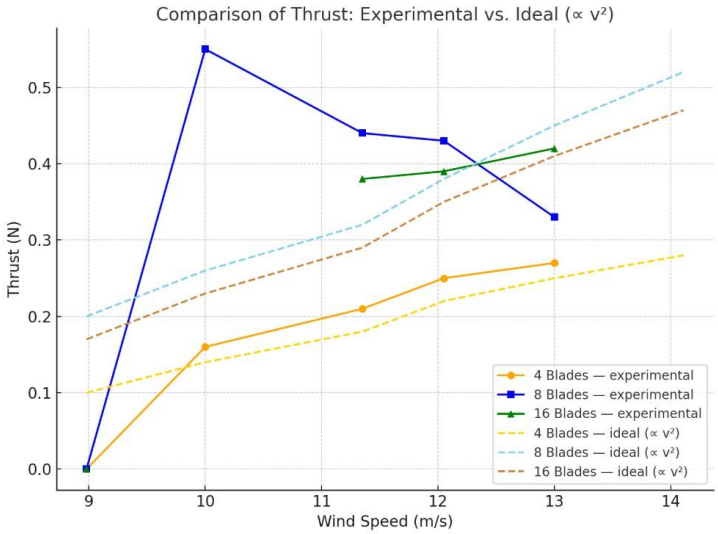

Figure 10. Experimental thrust curves of the four-, eight-, and sixteen-blade rotors compared with the theoretical quadratic model (T proportional to v squared)

The four-blade rotor exhibited an almost linear increase in thrust, rising from 0 to 0.27 N at a wind speed of 14.11 m/s. The experimental thrust values were generally lower than the ideal curve at low-to-medium wind speeds. At higher wind speeds, however, the experimental curve approached the theoretical trend. This indicates that the four-blade rotor operates more effectively under strong wind conditions, although the total thrust generated remains relatively small due to the limited wind capture area.

The eight-blade configuration displayed a distinctive performance pattern, achieving a maximum thrust of 0.55 N at a medium wind speed of 11.35 m/s. Beyond this point, thrust decreased even as wind speed continued to increase, causing the experimental curve to diverge from the ideal prediction. This behavior is attributed to increased aerodynamic drag and the onset of partial blade stall. Consequently, the eight-blade rotor can be categorized as the most efficient configuration at medium wind speeds, providing a favorable balance between rotational speed and thrust. However, its performance diminishes at higher wind velocities.

The sixteen-blade rotor showed a stable and consistent increase in thrust with increasing wind speed, reaching a maximum value of 0.46 N at 14.42 m/s. Although the thrust curve closely follows the ideal theoretical trend, the maximum RPM achieved was significantly lower than that of the four- and eight-blade configurations due to high drag forces. This confirms that the sixteen-blade rotor is better suited for low-to-medium wind conditions, where high starting torque is more critical than maximum rotational speed.

The comparison highlights a clear trade-off among rotational speed, thrust, and aerodynamic drag across the three rotor configurations:

- The four-blade rotor excels in rotational speed and performs better under high wind conditions but produces relatively low thrust.
- The eight-blade rotor delivers the highest thrust at medium wind speeds, making it the most balanced and efficient configuration overall.
- The sixteen-blade rotor provides stable thrust and high starting torque, making it suitable for low wind conditions, but its efficiency declines at medium-to-high wind speeds due to significant aerodynamic drag.

Accordingly, the eight-blade configuration is recommended as the most balanced design for the Flettner–VAWT rotor system. The four-blade rotor is more appropriate for strong wind conditions, while the sixteen-blade rotor is better suited for weaker wind environments.

CONCLUSIONS

This study was conducted to address the research problem of how variations in the number of quarter-circular curved blades in a Vertical Axis Wind Turbine (VAWT) affect the performance of a Flettner rotor in generating thrust for ship propulsion. The primary objective was to determine the blade configuration that provides optimal performance in terms of rotor speed (RPM), thrust, and overall system efficiency.

Experimental wind tunnel testing demonstrated that blade number has a significant influence on rotor performance. The four-blade rotor achieved the highest maximum rotational speed, reaching 2024 RPM at a wind speed of 14.11 m/s. However, its thrust output was relatively low at 0.27 N, making this configuration more suitable for high wind conditions where rotational speed is prioritized over thrust.

The eight-blade rotor exhibited the most balanced performance among the tested configurations. It delivered the highest maximum thrust of 0.55 N at a wind speed of 11.35 m/s while maintaining a relatively high rotational speed of 1819 RPM at 14.49 m/s. This balance makes the eight-blade configuration the most effective option under medium wind speed conditions.

In contrast, the sixteen-blade rotor generated relatively large and stable thrust, reaching 0.46 N at a wind speed of 14.42 m/s, and provided high starting torque. However, its maximum rotational speed was limited to 389 RPM, indicating reduced efficiency at medium-to-high wind speeds despite its effectiveness under low wind conditions.

Overall, this research successfully addressed the stated research problem and achieved its objectives by clearly identifying the influence of blade number variation on the aerodynamic performance of the Flettner–VAWT rotor and determining the optimal configuration. Based on the experimental results, the eight-blade rotor is recommended as the most efficient overall design. The four-blade rotor is better suited for high wind environments, while the sixteen-blade rotor is more appropriate for low wind conditions. These findings provide a valuable foundation for the future development of renewable and environmentally friendly ship propulsion systems.

ACKNOWLEDGEMENTS

The authors would like to express their sincere gratitude to the Aerodynamics Laboratory for providing the wind tunnel facilities that enabled this research. Special appreciation is extended to the technical staff for their invaluable assistance in the design, fabrication, and testing of the rotor models.

The authors are also grateful to colleagues in the academic community for their constructive feedback, which significantly improved the research methodology and data analysis. Institutional support from Universitas Kristen Cipta Wacana, both in terms of resources and academic environment, was essential to the successful completion of this study.

Finally, the authors would like to thank the internal reviewers for their insightful comments and suggestions, which greatly enhanced the quality of this article.

REFERENCES

[1] F. Rizzo, “The Flettner Rotor Ship in the Light of the Kutta-Joukowski Theory and of Experimental Results,” National Advisory Committee for Aeronautics, 1925. [Online]. Available: https://ntrs.nasa.gov/citations/19930080992

[2] F. M. White, *Fluid Mechanics*, 7th ed. New York: McGraw-Hill, 2011.

[3] T. Craft, H. Iacovides, and B. Launder, “Back to the future?,” *ICHMT, 7th International Symposium on Turbulence, Heat and Mass Transfer, THMT12*. Begell House Publishers Inc., New York, pp. 1053–1056, Sep. 2012.

[4] M. Vahs, “Retrofitting of Flettner Rotors: Results From Sea Trials of the General Cargo Ship ‘Fehn Pollux,’” *Int. J. Marit. Eng.*, vol. 162, no. A4, p. A-371–9, 2020, doi: https://doi.org/10.5750/ijme.v162iA4.1146.

[5] G. Bordogna *et al.*, “Experiments on a Flettner rotor at critical and supercritical Reynolds numbers,” *J. Wind Eng. Ind. Aerodyn.*, vol. 188, pp. 19–29, 2019, doi: https://doi.org/10.1016/j.jweia.2019.02.006.

[6] G. Bordogna, S. Muggiasca, S. Giappino, M. Belloli, J. A. Keuning, and R. H. M. Huijsmans, “The effects of the aerodynamic interaction on the performance of two Flettner rotors,” *J. Wind Eng. Ind. Aerodyn.*, vol. 196, p. 104024, 2020, doi: https://doi.org/10.1016/j.jweia.2019.104024.

[7] G. Angelini, S. Muggiasca, and M. Belloli, “A Techno-Economic Analysis of a Cargo Ship Using Flettner Rotors,” *Journal of Marine Science and Engineering*, vol. 11, no. 1. p. 229, 2023. doi: https://doi.org/10.3390/jmse11010229.

[8] B. Li, R. Zhang, Y. Li, B. Zhang, and C. Guo, “Study of a New Type of Flettner Rotor in Merchant Ships,” *Polish Marit. Res.*, vol. 28, no. 1, pp. 28–41, 2021, doi: https://doi.org/10.2478/pomr-2021-0003.

[9] D. Massaro, M. Karp, N. Jansson, S. Markidis, and P. Schlatter, "Direct numerical simulation of the turbulent flow around a Flettner rotor," *Sci. Rep.*, vol. 14, no. 1, p. 3004, 2024, doi: https://doi.org/10.1038/s41598-024-53194-x.

[10] L. Huang, Q. Song, R. Zhang, K. Wang, and R. Ma, "Study of the Influence of Rotor Shape on the Aerodynamic Characteristics of Flettner Rotor," *Adv. Transdiscipl. Eng.*, vol. Volume 40:, pp. 798–804, 2023, doi: https://doi.org/10.3233/ATDE230543.

[11] J. Lv, Y. Lin, R. Zhang, B. Li, and H. Yang, "Assisted Propulsion Device of a Semi-Submersible Ship Based on the Magnus Effect," *Polish Marit. Res.*, vol. 29, no. 3, pp. 33–46, 2022, doi: https://doi.org/10.2478/pomr-2022-0023.

[12] W. Chen, H. Wang, and X. Liu, "Experimental investigation of the aerodynamic performance of Flettner rotors for marine applications," *Ocean Eng.*, vol. 281, p. 115006, 2023, doi: https://doi.org/10.1016/j.oceaneng.2023.115006.

[13] H. Z. Jifu He, Kewen Li, Lin Jia, Yuhao Zhu and J. Linghu, "Advances in the applications of thermoelectric generators," *Appl. Therm. Eng.*, vol. 236, no. D, p. 121813, 2024, doi: 10.1016/j.applthermaleng.2023.121813.

[14] X. Liao *et al.*, "Corrosion behaviour of copper under chloride-containing thin electrolyte layer," *Corros. Sci.*, vol. 53, no. 10, 2011, doi: 10.1016/j.corsci.2011.06.004.

[15] B. Li, R. Zhang, B. Zhang, Q. Yang, and C. Guo, "An assisted propulsion device of vessel utilizing wind energy based on Magnus effect," *Appl. Ocean Res.*, vol. 114, p. 102788, 2021, doi: https://doi.org/10.1016/j.apor.2021.102788.

[16] D. Ponnaswami, O. Bilawar, S. Agasagi, R. Patil, and S. Maracharaddi, "Design and Analysis of Magnus Effect Mechanism on Wing for UAV Applications," *Tuijin Jishu/Journal Propuls. Technol.*, vol. 45, no. 03, pp. 1507–1513, 2024, doi: https://doi.org/10.52783/tjjpt.v45.i03.7437.

[17] Q. Zhang, "Application of magnus effect on wings," *Theor. Nat. Sci.*, vol. 9, pp. 180–186, 2023, doi: https://doi.org/10.54254/2753-8818/9/20240740.

[18] A. N. Alkhaledi, S. Sampath, and P. Pilidis, "Techno environmental assessment of Flettner rotor as assistance propulsion system for LH2 tanker ship fuelled by hydrogen," *Sustain. Energy Technol. Assessments*, vol. 55, p. 102935, 2023, doi: https://doi.org/10.1016/j.seta.2022.102935.

[19] N. R. Ammar and I. S. Seddiek, "Wind assisted propulsion system onboard ships: case study Flettner rotors," *Ships Offshore Struct.*, vol. 17, no. 7, pp. 1616–1627, Jul. 2022, doi: https://doi.org/10.1080/17445302.2021.1937797.

[20] J. Li, H. Lin, C. Sun, B. Jiao, G. Sun, and F. Cao, "Analysis of Aerodynamic Performance and Application of Flettner Rotor," *J. Inst. Eng. Ser. C*, vol. 105, no. 5, pp. 1373–1383, 2024, doi: https://doi.org/10.1007/s40032-024-01073-9.

[21] M. Reche-Vilanova, "Performance Prediction Program for Wind-Assisted Cargo Ships," 2020. doi: https://doi.org/10.13140/RG.2.2.24961.48480.

PISTON
Journal of Technical Engineering:

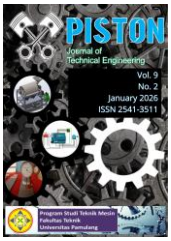

Synthesis and Characterization of Dual-doped (Al, Co) ZnO Nanofibers for Sustainable Piezoelectric Nanogenerator Applications

Ade Irvan Tauvana[1,a)], Lukman Nulhakim[1], Elsa Nurfadillah[1]

[1]*Department of Manufacturing Engineering Technology, Politeknik Enjinering Indorama, Purwakarta 41152, Indonesia*

E-mail: [a)] ade.irvan@pei.ac.id

Received: September 10, 2025 *Revision: January 20, 2026* *Accepted: January 29, 2026*

Abstract: This study reports the structural and morphological enhancement of aluminum (Al) and cobalt (Co) co-doped ZnO nanofibers synthesized via electrospinning for piezoelectric applications. The morphology and elemental composition were systematically analyzed using Scanning Electron Microscopy coupled with Energy-Dispersive X-ray Spectroscopy (SEM–EDX), while crystallographic properties were evaluated by X-ray Diffraction (XRD). SEM analysis revealed that the electrospun Al–Co co-doped ZnO nanofibers formed a highly interconnected and porous fibrous network with a uniform diameter distribution and negligible agglomeration, exhibiting diameters of 100–200 nm. EDX results confirmed the successful incorporation of Al and Co dopants into the ZnO matrix without detectable impurities. XRD patterns indicated a well-defined hexagonal wurtzite crystal structure with high crystallinity and a pronounced preferred orientation. The crystallite size, calculated using the Scherrer equation, ranges from 84 to 106 nm. The variation in crystallite size among different diffraction peaks is mainly attributed to differences in peak broadening (FWHM), which may indicate anisotropic crystallite growth and varying degrees of lattice orderingIn addition, the microstrain increased from 1.5×10^{-4} to 3.8×10^{-4}, suggesting lattice distortion induced by Al^{3+} and Co^{2+} substitution. These findings demonstrate that Al–Co co-doped ZnO nanofibers possess favorable structural characteristics for advanced piezoelectric material development.

Keywords: Electrospun ZnO Nanofibers, SEM–EDX, XRD, Crystallite Size; Microstrain, Piezoelectric Materials.

Abstrak: *Penelitian ini bertujuan untuk menganalisis karakteristik morfologi, komposisi unsur, dan struktur kristal nanofiber ZnO terdoping aluminium (Al) dan kobalt (Co) yang disintesis menggunakan metode elektrospinning. Karakterisasi morfologi dan distribusi unsur dilakukan menggunakan Scanning Electron Microscopy–Energy-Dispersive X-ray Spectroscopy (SEM–EDX), sedangkan sifat struktur kristal dianalisis menggunakan X-ray Diffraction (XRD). Hasil SEM menunjukkan bahwa nanofiber ZnO terdoping Al–Co membentuk jaringan serat berpori yang saling berjalin, terdistribusi homogen tanpa aglomerasi signifikan, dengan diameter nanofiber berkisar antara 100–200 nm. Analisis EDX mengonfirmasi keberadaan unsur O, Zn, Al, dan Co tanpa terdeteksinya unsur pengotor, yang menunjukkan kemurnian material yang relatif baik serta keberhasilan proses doping. Pola XRD memperlihatkan struktur kristal heksagonal wurtzite dengan tingkat kristalinitas yang baik dan orientasi kristal dominan. Ukuran kristalit yang dihitung menggunakan persamaan Scherrer berada pada rentang 84–106 nm dan menunjukkan tren meningkat pada puncak difraksi dengan nilai 2θ yang lebih tinggi. Nilai regangan mikro (microstrain) meningkat dari $1,5 \times 10^{-4}$ hingga $3,8 \times 10^{-4}$, yang mengindikasikan adanya distorsi kisi akibat substitusi ion Al^{3+} dan Co^{2+}. Karakteristik tersebut menunjukkan potensi nanofiber ZnO terdoping Al–Co untuk aplikasi piezoelektrik.*

Kata kunci: *ZnO Nanofiber; SEM–EDX; XRD; Ukuran Kristalit; Microstrain; Piezoelektrik.*

INTRODUCTION

Zinc oxide (ZnO) is a II–VI semiconductor that has attracted considerable research interest due to its wide direct bandgap of approximately 3.37 eV and high exciton binding energy of around 60 meV at room temperature. These intrinsic characteristics make ZnO a promising material for various applications, including optoelectronics, sensors, photocatalysis, and piezoelectric energy harvesting systems [1], [2]. Among these properties, the piezoelectric behavior of ZnO is particularly significant for nanogenerator applications, where

ambient mechanical energy can be converted into electrical energy to support self-powered and sustainable electronic devices [3].

ZnO nanostructures such as nanowires, nanorods, nanotubes, and nanofibers exhibit enhanced piezoelectric responses compared to bulk ZnO due to their high surface-to-volume ratio, superior mechanical flexibility, and efficient stress-induced polarization [4], [5]. These characteristics allow ZnO-based nanogenerators to operate effectively under low-frequency and low-amplitude mechanical excitations, which are commonly encountered in real-world environments [6]. In particular, one-dimensional ZnO nanofibers offer additional advantages, including continuous charge transport pathways and improved mechanical durability, making them highly suitable for flexible and wearable energy harvesting devices [7].

Despite these advantages, pristine ZnO still suffers from several inherent limitations, such as weak polarization strength, low carrier mobility, and defect-induced charge recombination caused by oxygen vacancies and zinc interstitials [8]. These drawbacks significantly limit the energy conversion efficiency and long-term stability of ZnO-based piezoelectric nanogenerators. To overcome these challenges, various material engineering strategies have been explored, among which metal-ion doping has emerged as one of the most effective approaches to tailor the structural, electrical, and piezoelectric properties of ZnO [9].

Among various dopants, aluminum (Al) and cobalt (Co) have received considerable attention due to their distinct and complementary effects on ZnO. Al^{3+} doping, which involves the substitution of Zn^{2+} ions, has been reported to improve crystallinity, increase carrier concentration, and reduce grain boundary resistance, thereby enhancing electrical conductivity and piezoelectric output [10]. In contrast, Co^{2+}/Co^{3+} doping can induce lattice distortion and modify the electronic band structure of ZnO, which may contribute to improved polarization-related behavior in piezoelectric applications [11]. However, single-element doping often results in trade-offs between electrical performance, crystallinity, and mechanical stability.

Recent studies have demonstrated that co-doping strategies can provide synergistic enhancements by combining the advantages of different dopant elements while mitigating their individual limitations [12]. In particular, Al–Co dual-doped ZnO has been reported to exhibit improved crystallinity, controlled defect states, enhanced lattice strain, and superior piezoelectric performance compared to singly doped or undoped ZnO [13]. Such synergistic effects are especially important for sustainable and flexible energy harvesting systems, where high electrical output and mechanical robustness are both critical requirements.

Electrospinning is a simple, scalable, and cost-effective fabrication technique that enables the production of continuous one-dimensional nanofibers with controlled diameter, high porosity, and homogeneous dopant distribution [14]. Electrospun ZnO nanofibers offer a porous network structure that facilitates efficient stress transfer and enhances piezoelectric response, making them promising candidates for next-generation sustainable piezoelectric nanogenerators [15]. Furthermore, electrospinning is compatible with large-area and flexible substrates, supporting its potential for practical device applications.

In this study, dual-doped (Al, Co) ZnO nanofibers were synthesized using the electrospinning method followed by thermal treatment to obtain crystalline ZnO structures. The effects of Al–Co co-doping on the morphological characteristics, crystallinity, and fiber diameter were systematically investigated using scanning electron microscopy (SEM) and X-ray diffraction (XRD). This work aims to provide a deeper understanding of the structure–property relationships of dual-doped ZnO nanofibers and to support the development of high-performance and sustainable piezoelectric nanogenerators for future self-powered systems.

METHODS

Zinc acetate dihydrate ($Zn(CH_3COO)_2 \cdot 2H_2O$, Merck), cobalt acetate tetrahydrate ($Co(CH_3COO)_2 \cdot 4H_2O$, Sigma-Aldrich), aluminum chloride hexahydrate ($AlCl_3 \cdot 6H_2O$, Merck), and polyvinyl alcohol (PVA, Mw = 72,000, Merck) were used as starting materials without further purification, as commonly employed in electrospun ZnO nanofiber synthesis [14]. A 10 wt% PVA solution was prepared by dissolving PVA in deionized water at 70 °C under continuous stirring for 4 h, followed by aging at room temperature for 8 h to ensure complete polymer chain relaxation and solution homogeneity [7]. Separately, aluminum chloride and cobalt acetate precursor solutions were prepared by dissolving 4 g of each salt in 20 g of deionized water and stirring at 70 °C for 1 h until clear and homogeneous solutions were obtained [10].

The prepared PVA solution was subsequently mixed with the metal salt solutions at a weight ratio of 1:4 and stirred at 70 °C for 8 h to ensure uniform dispersion of metal ions within the polymer matrix. The mixed solution was then stabilized at room temperature for 24 h to improve electrospinnability and solution viscosity stability [16]. As one of the composition variations, the precursor solution with an Al:Co ratio of 100:0 (Al-only,

control sample) was used for the electrospinning process. Electrospinning was carried out using a high-voltage power supply connected to a syringe pump equipped with a stainless-steel needle with an inner diameter of 0.65 mm. The nanofibers were collected on a nonwoven membrane mounted on a rotating drum collector. The electrospinning parameters were optimized and fixed at an applied voltage of 13 kV, a tip-to-collector distance of 13 cm, a solution feed rate of 0.5 mL h^{-1}, and a drum rotation speed of 125 rpm, while the relative humidity was maintained at approximately 58%. These parameters were selected based on previous reports to obtain uniform, bead-free ZnO-based nanofibers [17], [18].

The surface morphology and fiber structure of the electrospun nanofibers were examined using scanning electron microscopy (SEM). The fiber diameter distributions were quantitatively analyzed from SEM micrographs using ImageJ software, and statistical analysis of diameter distribution was performed using Origin software, following established procedures for electrospun nanofiber characterization [19], [20]. The crystalline phase, crystallite size, and degree of crystallinity of the nanofibers were characterized by X-ray diffraction (XRD), which is a standard technique for evaluating structural properties of doped ZnO nanomaterials [21].

RESULT AND DISCUSSION

Morphological Analysis of Electrospun Nanofibers (SEM)

Characterization using Scanning Electron Microscopy coupled with Energy-Dispersive X-ray Spectroscopy (SEM–EDX) was carried out to observe the surface morphology, fiber diameter, and elemental composition of each sample. The microstructural morphology was obtained from SEM analysis by scanning the sample surface using an electron beam at magnifications of 5000×, 10,000×, and 25,000×.

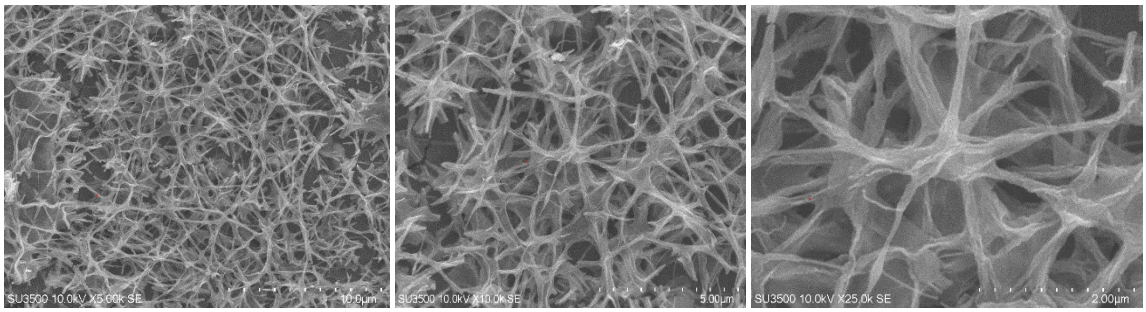

Figure 1. SEM images of the 100% $AlCl_3$ sample at magnifications of (a) 5000×, (b) 10,000×, and (c) 25,000×

The SEM images in Figure 1 show that the 100% $AlCl_3$ sample exhibits a nanofiber structure forming a porous and interwoven network. At magnifications of 5000× to 10,000×, the nanofibers are uniformly distributed without significant agglomeration, indicating that the electrospinning process successfully produced homogeneous fibers with good morphological stability [17], [22]. Such uniform fiber distribution is essential for achieving consistent mechanical deformation and reliable electrical output in piezoelectric applications [3]. At a higher magnification of 25,000×, the surface features of the nanofibers become more pronounced, revealing a relatively rough surface texture. This morphology is commonly observed in polycrystalline ZnO nanofibers after thermal treatment and is considered beneficial for stress transfer under mechanical loading [10]. Based on the SEM scale bar, the nanofiber diameter is estimated to be in the range of 100–200 nm [4]. Nanofibers within this diameter range are known to exhibit enhanced flexibility and strain sensitivity, which are advantageous for piezoelectric nanogenerator applications [3], [23].

In addition to SEM characterization, Energy-Dispersive X-ray (EDX) analysis was carried out to evaluate the elemental composition and distribution within the samples. The EDX results confirm the presence of O, Al, Zn, and Co elements in the samples, indicating successful incorporation of dopant elements into the ZnO nanofiber matrix without detectable impurity phases [24]. Minor deviations between theoretical and experimental values can be attributed to the surface-sensitive nature of EDX analysis and local compositional variations within the nanofibers [25]. The confirmed presence and distribution of Al and Co dopants are crucial, as dopant-induced lattice distortion and defect engineering are known to enhance polarization behavior and piezoelectric performance in ZnO-based nanostructures [10].

Elemental Composition Analysis (EDX)

To provide a more detailed evaluation of the elemental composition of the synthesized nanofibers, Energy-Dispersive X-ray (EDX) analysis was conducted. EDX provides both qualitative and semi-quantitative information regarding elemental composition and is widely used to verify the successful incorporation of dopant elements within oxide nanostructures [24]. The EDX spectra reveal the presence of oxygen (O), zinc (Zn),

aluminum (Al), and cobalt (Co), indicating that the electrospinning and calcination processes successfully produced Al–Co co-doped ZnO nanofibers without the appearance of unintended impurity elements. Table 1 summarizes the comparison between the theoretical weight percentages calculated based on stoichiometric relations and the experimental values obtained from EDX measurements.

The experimental elemental compositions show reasonable agreement with the theoretical values, with minor deviations that can be attributed to instrumental limitations, the surface-sensitive nature of EDX analysis, and local compositional variations within the nanofibers. These results confirm that the electrospinning and subsequent thermal treatment processes effectively preserved the intended chemical composition of the samples. The verified presence of Al and Co dopants is particularly important, as dopant-induced lattice distortion and defect engineering are known to significantly influence charge polarization, crystal symmetry, and piezoelectric response in ZnO-based nanostructures [24], [25]. Such compositional control is therefore essential for optimizing the performance of ZnO-based piezoelectric nanogenerators.

Table 1. EDX analysis results of Al–Co-doped ZnO nanofibers

Element	Weight %	Atomic %	Net int.
O K	11.37	21.54	577.83
Al K	56.57	63.56	4086.36
Co K	0.47	0.24	6.08
Zn K	31.60	14.66	169.72

Based on the EDX results, O, Al, Zn, and Co elements were detected, indicating that the synthesized material consists of metal oxides with the presence of aluminum and cobalt dopants. The absence of other elements suggests relatively good material purity. The dominance of Al and the presence of trace amounts of Co indicate that the doping process was successful. The substitution of Al^{3+} for Zn^{2+} may produce charge imbalance, which can promote the formation of oxygen vacancies and lattice strain. This combination of effects is expected to enhance local polarization and improve the piezoelectric performance of the material.

XRD Analysis: Crystallite Size

In this study, ZnO nanofibers composed of nanoscale crystallites were characterized using X-ray diffraction (XRD) to identify the diffraction peaks and evaluate their crystallographic structure. The diffraction patterns were further analyzed using the HighScore Plus software. The results are shown in Figure 2.

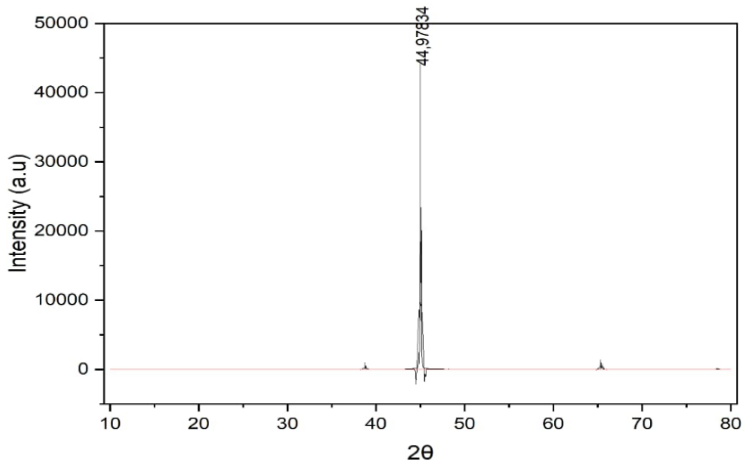

Figure 2. XRD diffraction pattern of Al–Co-doped ZnO nanofibers

The XRD pattern is dominated by a strong diffraction peak corresponding to the (002) plane, while other characteristic ZnO peaks are present with significantly lower intensities with high intensity and a low background, indicating good crystallinity and a preferred crystal orientation of the synthesized ZnO nanofibers [21]. The diffraction peaks can be indexed to the hexagonal wurtzite crystal structure of ZnO, which is consistent with standard JCPDS data and previous reports on ZnO-based nanostructures [26]. The absence of secondary phases or impurity-related peaks further confirms the phase purity of the synthesized materials.

The crystallite size was calculated using the Debye–Scherrer equation based on the full width at half maximum (FWHM) of the diffraction peak. The calculated crystallite size lies in the nanometer range, indicating that each nanofiber consists of an assembly of nanoscale crystallites rather than a single crystal [27]. This structural characteristic is advantageous for piezoelectric applications, as the combination of nanoscale crystallites and one-dimensional nanofiber morphology can enhance mechanical deformation and induce higher local polarization under external stress [28].

In addition, the microstrain (ε), which reflects lattice distortion and defect density, was estimated from the FWHM using the Williamson–Hall approach in its simplified form. The presence of microstrain suggests lattice distortion that may arise from dopant incorporation and size-induced effects, which is known to influence the piezoelectric response of ZnO nanostructures [25]. Referring to the FWHM value, the crystallite size (D) of ZnO samples was calculated using the Debye–Scherrer equation as follows:

$$D = \frac{k\lambda}{\beta \cos\theta} \quad (1)$$

Meanwhile, the microstrain value was calculated using the following equation:

$$\varepsilon = \frac{\beta}{4\,tan\,\theta} \quad (2)$$

Here, k is the Scherrer constant (0.9), λ is the XRD wavelength (0.154056 nm), θ is the diffraction angle, β is the full width at half maximum (FWHM), D is the crystallite size, and ε is the microstrain.

Table 2. Structural parameters of ZnO nanoparticle samples

No.	2θ (°)	h	k	l	FWHM	Crystallite size (nm)	d-spacing (nm)	Microstrain
1	38.739	1	1	1	0.16	84.21	0.281	0.00015
2	43.697	0	0	2	0.14	85.59	0.260	0.00017
3	44.971	0	0	2	0.15	85.98	0.247	0.00018
4	65.316	0	2	2	0.13	94.36	0.191	0.00027
5	78.422	1	1	3	0.12	102.53	0.163	0.00035
6	82.721	1	1	3	0.14	105.84	0.148	0.00038

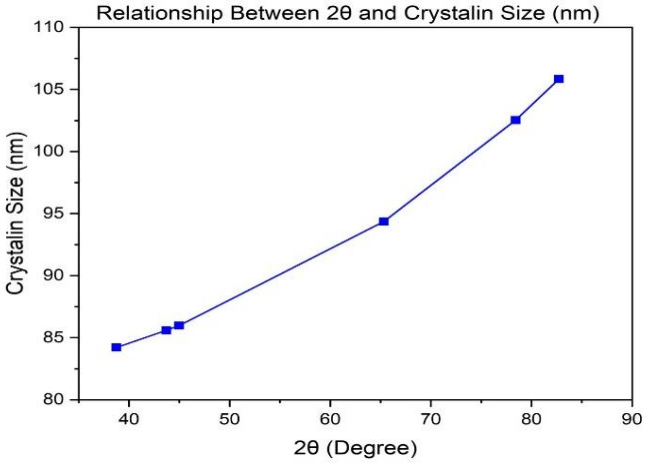

Figure 3. Relationship between 2θ and crystallite size

Based on the XRD results, the crystallite size of the synthesized ZnO ranges from 84 to 106 nm and shows an increasing trend at higher diffraction angles (2θ). The Scherrer equation indicates that peaks at higher 2θ values may yield larger crystallite sizes due to the cosθ term in the equation. The microstrain value also increases from 0.00015 to 0.00038, indicating a slight increase in lattice distortion at higher 2θ values.

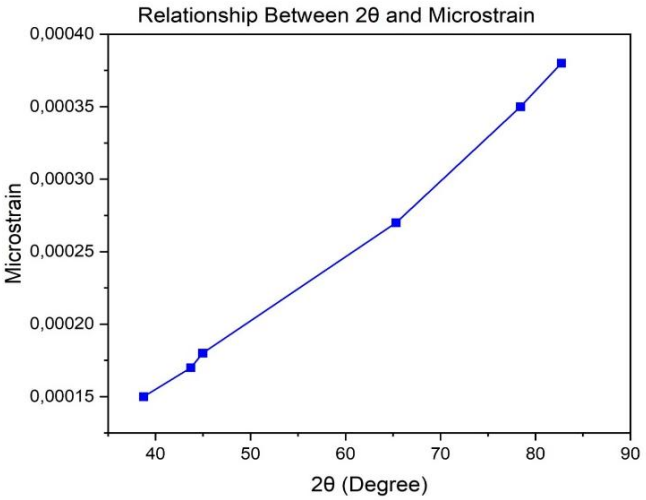

Figure 4. Relationship between 2θ and microstrain

Figure 4 shows the relationship between the diffraction angle 2θ and microstrain in doped ZnO nanofibers. It is observed that the microstrain value increases from 1.5×10^{-4} to 3.8×10^{-4} with increasing 2θ. This increase is attributed to the higher sensitivity of higher-order crystal planes to lattice distortion, as well as local strain effects due to the substitution of Al^{3+} and Co^{2+} ions in the ZnO lattice. Despite the increase in crystallite size, the presence of microstrain indicates residual internal stress, which may enhance local polarization and thus benefit piezoelectric applications.

CONCLUSIONS

Aluminum (Al) and cobalt (Co) co-doped ZnO nanofibers were successfully synthesized, exhibiting a highly interconnected and porous fibrous morphology with uniform distribution and fiber diameters of 100–200 nm. EDX analysis confirmed the presence of O, Zn, Al, and Co without detectable impurities, indicating good material purity and effective dopant incorporation. XRD results revealed a well-defined hexagonal wurtzite crystal structure with high crystallinity and a dominant preferred orientation. The crystallite size ranged from 84 to 106 nm and showed an increasing trend at higher diffraction angles (2θ), while the microstrain increased from 1.5×10^{-4} to 3.8×10^{-4}, indicating lattice distortion induced by Al^{3+} and Co^{2+} substitution. The presence of microstrain is expected to promote local polarization, highlighting the potential of Al–Co co-doped ZnO nanofibers for piezoelectric material development.

ACKNOWLEDGEMENTS

The authors sincerely acknowledge the valuable support and contributions of all parties who assisted in the completion of this research. Special thanks are extended to Politeknik Enjinering Indorama for providing essential equipment used in the characterization process. This research was financially supported by the PDP program, funded by DPPM–DIKTISAINTEK, under Contract No. DIPA 139.04.1.693320/2025.

REFERENCES

[1] A. Janotti and C. G. Van de Walle, “Fundamentals of zinc oxide as a semiconductor,” *Reports Prog. Phys.*, vol. 72, no. 12, p. 126501, 2009, doi: https://doi.org/10.1088/0034-4885/72/12/126501.

[2] C. Jin, J. Zhou, Z. Wu, and J. X. J. Zhang, “Doped Zinc Oxide-Based Piezoelectric Devices for Energy Harvesting and Sensing,” *Adv. Energy Sustain. Res.*, vol. 6, no. 9, p. 2500017, Sep. 2025, doi: https://doi.org/10.1002/aesr.202500017.

[3] Z. L. Wang and J. Song, “Piezoelectric nanogenerators based on zinc oxide nanowire arrays,” *Science*, vol. 312, no. 5771, pp. 242–246, Apr. 2006, doi: https://doi.org/10.1126/science.1124005.

[4] N. Bhadwal, R. Ben Mrad, and K. Behdinan, “Review of Zinc Oxide Piezoelectric Nanogenerators: Piezoelectric Properties, Composite Structures and Power Output,” *Sensors*, vol. 23, no. 8. p. 3859, 2023. doi: https://doi.org/10.3390/s23083859.

[5] S. Xu, Y. Qin, C. Xu, Y. Wei, R. Yang, and Z. L. Wang, “Self-powered nanowire devices,” *Nat. Nanotechnol.*, vol. 5, no. 5, pp. 366–373, May 2010, doi: https://doi.org/10.1038/nnano.2010.46.

[6] E. S. Nour *et al.*, “Low-Frequency Self-Powered Footstep Sensor Based on ZnO Nanowires on Paper Substrate,” *Nanoscale Res. Lett.*, vol. 11, no. 1, p. 156, 2016, doi: https://doi.org/10.1186/s11671-016-1373-1.

[7] H. Parangusan, D. Ponnamma, and M. A. A. Al-Maadeed, “Stretchable Electrospun PVDF-HFP/Co-ZnO Nanofibers as Piezoelectric Nanogenerators,” *Sci. Rep.*, vol. 8, no. 1, p. 754, 2018, doi: https://doi.org/10.1038/s41598-017-19082-3.

[8] C. Klingshirn, “ZnO: material, physics and applications,” *Chemphyschem*, vol. 8, no. 6, pp. 782–803, Apr. 2007, doi: https://doi.org/10.1002/cphc.200700002.

[9] C. Jin *et al.*, “Flexible piezoelectric nanogenerators using metal-doped ZnO-PVDF films,” *Sensors Actuators A Phys.*, vol. 305, p. 111912, 2020, doi: https://doi.org/10.1016/j.sna.2020.111912.

[10] S. Hajer *et al.*, “Influence of (Co+Al) co−doping on structural, micro-structural, optical and electrical properties of nanostructured zinc oxide,” *Ceram. Int.*, vol. 50, no. 21, Part C, pp. 44151–44164, 2024, doi: https://doi.org/10.1016/j.ceramint.2024.08.264.

[11] R. Saleh and N. F. Djaja, “Transition-metal-doped ZnO nanoparticles: Synthesis, characterization and photocatalytic activity under UV light,” *Spectrochim. Acta Part A Mol. Biomol. Spectrosc.*, vol. 130, pp. 581–590, 2014, doi: https://doi.org/10.1016/j.saa.2014.03.089.

[12] C. Liu *et al.*, “Improvement in the Piezoelectric Performance of a ZnO Nanogenerator by a Combination of Chemical Doping and Interfacial Modification,” *J. Phys. Chem. C*, vol. 120, no. 13, pp. 6971–6977, Apr. 2016, doi: https://doi.org/10.1021/acs.jpcc.6b00069.

[13] D. Subagiyo and Suyitno, “Enhancing Output Voltage of Piezoelectric-Based Nanogenerators Using Zinc Oxide

Material Codoped with Aluminum and Cobalt," *IOP Conf. Ser. Mater. Sci. Eng.*, vol. 267, no. 1, p. 12037, 2017, doi: https://doi.org/10.1088/1757-899X/267/1/012037.
[14] S. Ramakrishna, K. Fujihara, W.-E. Teo, T.-C. Lim, and Z. Ma, *An Introduction to Electrospinning and Nanofibers*. World Scientific, 2005. doi: https://doi.org/10.1142/5894.
[15] X. Li *et al.*, "From Fiber to Power: Recent Advances Toward Electrospun-Based Nanogenerators," *Adv. Funct. Mater.*, vol. 35, no. 13, p. 2418066, Mar. 2025, doi: https://doi.org/10.1002/adfm.202418066.
[16] T. Pirzada, S. A. Arvidson, C. D. Saquing, S. S. Shah, and S. A. Khan, "Hybrid Silica–PVA Nanofibers via Sol–Gel Electrospinning," *Langmuir*, vol. 28, no. 13, pp. 5834–5844, Apr. 2012, doi: https://doi.org/10.1021/la300049j.
[17] A. Greiner and J. H. Wendorff, "Electrospinning: A Fascinating Method for the Preparation of Ultrathin Fibers," *Angew. Chemie Int. Ed.*, vol. 46, no. 30, pp. 5670–5703, Jul. 2007, doi: https://doi.org/10.1002/anie.200604646.
[18] B. A. Chinnappan, M. Krishnaswamy, H. Xu, and M. E. Hoque, "Electrospinning of Biomedical Nanofibers/Nanomembranes: Effects of Process Parameters," *Polymers*, vol. 14, no. 18. p. 3719, 2022. doi: https://doi.org/10.3390/polym14183719.
[19] J. Schindelin *et al.*, "Fiji: an open-source platform for biological-image analysis," *Nat. Methods*, vol. 9, no. 7, pp. 676–682, 2012, doi: https://doi.org/10.1038/nmeth.2019.
[20] C. A. Schneider, W. S. Rasband, and K. W. Eliceiri, "NIH Image to ImageJ: 25 years of image analysis," *Nat. Methods*, vol. 9, no. 7, pp. 671–675, 2012, doi: https://doi.org/10.1038/nmeth.2089.
[21] B. D. Cullity and S. R. Stock, *Elements of X-ray Diffraction*, 3rd ed. United States: Pearson, 2014.
[22] P. Fakhri *et al.*, "Flexible hybrid structure piezoelectric nanogenerator based on ZnO nanorod/PVDF nanofibers with improved output," *RSC Adv.*, vol. 9, no. 18, pp. 10117–10123, 2019, doi: http://dx.doi.org/10.1039/C8RA10315A.
[23] C.-L. Hsu and K.-C. Chen, "Improving Piezoelectric Nanogenerator Comprises ZnO Nanowires by Bending the Flexible PET Substrate at Low Vibration Frequency," *J. Phys. Chem. C*, vol. 116, no. 16, pp. 9351–9355, Apr. 2012, doi: 10.1021/jp301527y.
[24] J. I. Goldstein, D. E. Newbury, J. R. Michael, N. W. M. Ritchie, J. H. J. Scott, and D. C. Joy, *Scanning Electron Microscopy and X-Ray Microanalysis*. New York, NY: Springer, 2018. doi: http://doi.org/10.1007/978-1-4939-6676-9.
[25] A. R. West, *Solid State Chemistry and its Applications*, 2nd ed. Chichester: John Wiley & Sons, Ltd., 2014.
[26] Ü. Özgür *et al.*, "A comprehensive review of ZnO materials and devices," *J. Appl. Phys.*, vol. 98, no. 4, p. 41301, Aug. 2005, doi: https://doi.org/10.1063/1.1992666.
[27] A. L. Patterson, "The Scherrer Formula for X-Ray Particle Size Determination," *Phys. Rev.*, vol. 56, no. 10, pp. 978–982, Nov. 1939, doi: https://doi.org/10.1103/PhysRev.56.978.
[28] Y. Qin, X. Wang, and Z. L. Wang, "Microfibre–nanowire hybrid structure for energy scavenging," *Nature*, vol. 451, no. 7180, pp. 809–813, 2008, doi: https://doi.org/10.1038/nature06601.